UNIVERSITÀ DEGLI STUDI DI MILANO

Scuola di Dottorato in Fisica, Astrofisica e Fisica Applicata
Dipartimento di Fisica

Corso di Dottorato in Fisica, Astrofisica e Fisica Applicata
Ciclo XXX

Generation and Detection of Nonclassical States in the Continuous Variable Regime

Settore Scientifico Disciplinare FIS/03

Supervisore: Dr Simone CIALDI

Co-Supervisore: Prof. Matteo G. A. PARIS

Coordinatore: Prof. Francesco RAGUSA

Tesi di Dottorato di:
Carmen Porto

Anno Accademico 2016-2017

Commission of the final examination:

External Referee:
Dr. Alessia Allevi
Dr. Alberto Porzio

External Member:
Prof. Lorenzo Maccone
Prof. Giuseppe Vallone

Internal Member:
Prof. Matteo G. A. Paris

Final examination:

Date 23/01/2018

Università degli Studi di Milano, Dipartimento di Fisica, Milano, Italy

A Te Nonna

Contents

List of Figures vii

List of Tables xiii

Introduction xiii

Part I : Non classical states of light 3

1 Theoretical concepts 3
- 1.1 The electromagnetic field quantization 3
- 1.2 Quantum states of light 5
  - 1.2.1 Fock states 5
  - 1.2.2 Coherent States 6
  - 1.2.3 Thermal states 6
- 1.3 Quadrature operators 7
- 1.4 Squeezed states 10
- 1.5 Gaussian states 10
  - 1.5.1 Basic notation and definition of Gaussian state 11
  - 1.5.2 Linear and bilinear Hamiltonians 11
- 1.6 Detecting quantum states of light 13
- 1.7 Quantum state tomography 17

2 Generation of nonclassical states 19
- 2.1 Second-order optical nonlinearity 19
  - 2.1.1 Conservation laws 21
- 2.2 Optical parametric oscillation 22
- 2.3 The quantum behaviour of the Optical Parametric Oscillator (OPO) 23
  - 2.3.1 Classical description of a linear cavity 23
  - 2.3.2 Non-linear interaction 25
  - 2.3.3 The quantum equations of motion for the OPO 26
- 2.4 Calculation of squeezing from an OPO cavity 26
- 2.5 Classical properties of parametric amplification. 28
- 2.6 Losses effect on squeezing 29

3 The experimental setup **31**
3.1 Introduction 32
3.2 The laser 32
3.3 States generation stage 35
3.3.1 State preparation stage 36
3.3.2 Squeezed state generation: OPO. 43
3.3.3 Pump optical layout 49
3.4 PDH 51
3.5 Homodyne detection 54
3.6 Propagation of squeezing 58
3.7 The glass-integrated homodyne detector 61
3.7.1 The integrated homodyne analyzer (IHA) 61
3.7.2 Optical layout 61

Part II : Non classical states measurements **67**

4 Full quantum state reconstruction of symmetric two-mode squeezed thermal states via spectral homodyne detection and a state-balancing detector **67**
4.1 Introduction 67
4.2 Experimental results 72
4.3 Concluding remarks 74

5 Quantum-to-classical transition for squeezed thermal states (STS) of a single-mode optical system **77**
5.1 Introduction 77
5.2 Single-mode Gaussian states 78
5.3 Homodyne tomography 79
5.4 Conclusions 81

6 Squeezing detection by using an glass-integrated homodyne analyzer **83**
6.1 Introduction 83
6.2 Squeezed vacuum states 83
6.3 Squeezed coherent states 86
6.4 Conclusion 88

Conclusions and Perspectives **89**

Bibliography **91**

List of Publications **97**

Acknowledgments **100**

List of Figures

1 Wu et al. used degenerate parametric down-conversion ($MgO:LiNbO_3$) in a magnesium-doped lithium niobate crystal placed in a standing-wave cavity (M;M') **(a)**. The results are displayed on the right **(b)**, where the root mean square noise voltage measured by the spectrum analyzer is shown versus the phase of the local oscillator. The squeezing was about 3.5 dB below the vacuum noise (dashed line) [1]. xvi

2 (**a**): Schematic of the experimental setup used in Ref. [4]. (**b**): Squeezing and antisqueezing spectra normalized to the vacuum noise level, experiment (continuous lines) and theory (dashed lines) for different OPA pump power (P). With P = 16 mW, a nonclassical noise reduction of 15.3 dB was obtained [4] xvi

1.1 (a) Phasor representation of the classical wave. In (b) it is highlighted that the fluctuations of the quadratures correspond to amplitude and phase fluctuations 8

1.2 Representations in the phasor diagram of the vacuum and generic coherent states. 9

1.3 Representations in the phasor diagram of the amplitude (on the right) and phase squeezed (on the left) vacuum states. 10

1.4 The Gaussian Wigner function for the vacuum state. The level' curve at the level of the quadrature variances is the uncertainty area in the two-dimensional phasor diagram. 13

1.5 Wigner functions for a coherent state, a displaced phase squeezed state and a displaced amplitude squeezed state from left to right. 13

1.6 Schematic diagram of the Homodyne Detector. 14

1.7 Schematic diagram of the Homodyne detection. 16

1.8 Sidebands. 16

2.1 Overview of the basic $\chi^{(2)}$ nonlinear interactions. There are two groups of nonlinear effects which can be divided into upconversion and downconversion processes. The upconversion processes are second harmonic generation (SHG) and sum frequency generation, which is the non-degenerate case of SHG. The upconversion processes are degenerate optical parametric oscillation (DOPO) and amplification (DOPA) and the corresponding non degenerate processes NDOPO and NDOPA. The difference between OPO and OPA is that the OPA is seeded with fundamental field, whereas this seed is replaced with a vacuum field for the OPO. * denotes the seed photons. 20
2.2 A model of passive optical resonator, including input fields from the input and output couplers, input field fluctuations due to loss in the resonator, and output fields exiting the input and output couplers. 23
2.3 OPO cavity layout. 25
2.4 Squeezing from an optical parametric oscillator as a function of pump power normalized to the threshold power when Ω=0. The plots show the predicted amplitude (phase) quadrature variance of the output field for two values of the escape efficiency of OPO cavity. Pump depletion is neglected, and all the input fields are assumed to be in coherent or vacuum states. The calculation was performed with the experimental parameters derived in Chap. 3 27
2.5 The predicted frequency spectra of the squeezing at half threshold for an OPO operating in the deamplification regime, with $\eta_{esc} = 0.914$. 28
2.6 The beam splitter model of losses. 29

3.1 Experimental setup for generation and detection of squeezed state. It consists of four stages, laser, state generation, PDH and homodyne detection stages. The principal radiation source is provided by a homemade single-mode Nd:YAGlaser internally frequency doubled by a periodically poled MgO:$LiNbO_3$. The laser output at 532 nm is used as the pump for an optical parametric oscillator (OPO), whereas the other output at 1064 nm is sent to a polarising beam splitter (PBS) to generate the input for the state generation stage and the local oscillator (LO) for the homodyne detector. The sidebands used as OPO coherent seeds are generated by exploiting the combined effect of the two optical systems, MOD1 and MOD2. A phase modulator (PM) generates the sidebands used as active stabilization of the OPO cavity via the Pound-Drever-Hall (PDH) technique. The homodyne detector consists of a balanced beam splitter, two low noise detectors (D1 and D2), and a differential amplifier. The powers of the LO and of the pump are set by amplitude modulators (AM) that consist of an half-wave plate and a Brewster plate. 31
3.2 Schematic diagram of the laser compared with its photo. The active medium is a cylindrical Nd:YAG crystal and a periodically poled MgO:LiNbO3 (PPLN) is used for the second harmonic generation. The single mode operation is ensured by a light diode which consists of a half-wave plate ($\lambda/2$), a Faraday rotator (FR) and a Brewster plate (BP). 33
3.3 Profile of w(z) inside the laser cavity during a round trip starting from the Nd:YAG crystal. The crystal for the second-harmonic generation (PPLN) is in the center. 34
3.4 Laser output power vs pump current: @1064 nm (red) @532 nm (green). 35

3.5 Zoom on states generation stage. 35
3.6 Optical layout of the state preparation stage. 36
3.7 The ramp generator (RG) output which drives the LO PZT. generates a triangle-shaped waveform triggered by a rectangular function with the two pulse widths (positive and negative) different in time: on the falling edge of the rectangular wave, the positive rise of the ramp. Its pulse width along with the duty cycle can be changed. 38
3.8 The "Flow charts" of the main operations developed in Labview program in order to control the generation and acquisition processes. 39
3.9 Screenshot of the first step of the generation/acquisition process. It is consist in acquiring the vacuum states and saving its variance. 40
3.10 Screenshot of the second step of the generation/acquisition process. 40
3.11 The screenshot of the front panel when we choose to generate a CS with selectable main photon number and phase. Once these parameters are set, the software reads β_1 and β_2 saved in the previous step and generates the right voltage value to be sent to MOD1 and MOD2, according to the sequence illustrated in the block diagram at the bottom right corner. 41
3.12 Coherent States generated by choosing the main photon number, n_{ph} and phase, φ on demand. On the right the homodyne traces corresponding to three coherent states generated by setting $\varphi = 0$ and $n_{ph} = 1.5$,$n_{ph} = 2.3$ and $n_{ph} = 4.5$ are shown, on the left three coherent states with the same main photon number, $n_{ph} = 4.5$ but with different phase values, $\varphi_1 = 0$,$\varphi_2 = \pi/4$ and $\varphi_3 = \pi/2$ are plotted. The fitted curves (continuous lines) parameters, amplitude and phase, are in agreement with the values which we have chosen to set. 41
3.13 Screenshot of the third step of the generation/acquisition process when we want to generate a termal state by setting the main photon number on demand. 42
3.14 Schematic diagram of the optical parametric oscillator (OPO) with its photo. It is a linear optical resonator consisting of two concave mirrors with radii of curvature r_{ic}=10mm, r_{oc}=25mm and separation L, and a MgO:LiNbO3 crystal length L_c=10mm. 43
3.15 Cavity response. Upper panel: expected link between the transmitted (P_{out}) with the input power (P_{in}) as function of OPO detuning $\delta\nu$, by considering the parameters of our cavity. Lower panel: OPO internal field. 45
3.16 Propagation of the mode waist w(z) inside the cavity 46
3.17 Precise mode matching of a Gaussian beam via telescopic lens arrangement. With the combination of L_1 and L_2 combination we collimate the beam. L_3 is used to achieve the desired beam waist in the crystal center. 46
3.18 Photo of the OPO in which the optical elements used to achieve the mode-matching are highlighted. 47
3.19 The ordinary refractive index, n_0, and extraordinary refractive index, n_e of $MgO:LiNbO_3$ as functions of the temperature. 48
3.20 The effect of phase mismatch on the non-linear interaction strength using $MgO:LiNbO_3$ 48
3.21 Pump optical layout. 49
3.22 Propagation of the mode waist w(z) of the seed field (red) and of the pump beam (green) inside the cavity. 50

3.23 Measurements of the gain of the parametric amplification as functions of pump power P. By fitting the experimental data with expression in 3.13 we retrieve that the OPO threshold is P_{th}=970 mW. 50
3.24 Magnitude and phase of the reflection coefficient for the OPO cavity. 51
3.25 Real and imaginary part of the cavity reflection coefficient $A(\omega,\Omega)$ at Ω=111 MHz. $\Im A(\omega,\Omega)$ is a smooth function with odd symmetry around the cavity resonance and therefore represents a suitable candidate for the generation of an error signal. 52
3.26 Scheme of the system for generating the PDH signal and keeping the cavity length constant. 53
3.27 Zoom on Homodyne Detection scheme 54
3.28 Sketch of the homodyne detector showing in which way the quantum efficiencies η_D of the photodiodes is modeled. 55
3.29 Schematic models of mode mismatch at BS in Homodyne Detector 57
3.30 Photo of our homodyne detector in which the main elements are highlighted. 58
3.31 Comparison between the experimental data and the theoretical expectation in the two OPO configurations implemented in our laboratory: one with $\eta_{esc} = 0.815$ the other with $\eta_{esc} = 0.924$. 59
3.32 Measurements of the OPO regenerative gain G as functions of pump power P. By fitting the experimental data we obtain P_{th1}=1900 mW for the OPO configuration with $\eta_{esc} = 0.815$ and P_{th2}=970 mW for the OPO configuration with $\eta_{esc} = 0.924$ 60
3.33 Homodyne traces of the vacuum squeezed state with OL power ∼10 mW and pump power ∼ 300 mW. On the left the acquisition performed with the OPO configuration characterized by η_{esc} = 0.924 is shown, on the right one with η_{esc} = 0.815. The measured squeezing levels are -5.8 dB and 3.6 dB, respectively, and are in agreement with the theoretical values. 60
3.34 Once the state is generated, the OPO output beam can be directed onto either SHD or IHA by means of mirrors with high reflectivity at 1064 nm mounted on flippers. The homodyne detection system, indeed, is designed in such a way that we are able to pass from the configuration based on SHD to the configuration exploiting the IHA in a quickly and simply way. Therefore, an immediate comparison can be made between the measurements realized with both layouts. When the mirrors are flipped up, the signal is coupled to the IHA. In order to efficiently coupling the out coming signal from the OPO and the LO into and out of the waveguides, a pair of fiber arrays is used for the entry and exit interfaces of the IHA to inject and eject signal and LO beams efficiently. The LO phase is changed thanks to a thermal phase shifter (IPS). See the text for more details. 62
3.35 Pictorial zoom on the coupling system fibers-IHA. The fiber arrays-to-waveguide coupling efficiency is improved by aligning their position and orientation with a high degree of accuracy. For this purpose the two fiber arrays are separately mounted on two six-axis positioning stages with micron resolution. The alignment is a long and delicate iterative procedure but once the relative orientations between the components have been optimised, we have observed that the overall system remains stable. 63

4.1 Schematic diagram of the experimental setup. 68

4.2 (a) PDH error signal as a function of the cavity displacement $\delta x = L - L_0$, where L is the cavity length and L_0 refers to the resonant condition with the pump at ω_0: the value of $E_{\rm PDH}$ allows to retrieve the information about the detuning $\delta\omega$. (b) Cavity transmission coefficient as a function of ω when $E_{\rm PDH} = 0$: one has the maximum $T_0(0) = 1$ and $T_0(+\Omega) = T_0(-\Omega)$. (b) Cavity transmission coefficient as a function of ω in the presence $E_{\rm PDH} \neq 0$ (in the plot we consider $E_{\rm PDH} > 0$): now one finds the transmissivity maximum at $\delta\omega$, namely, $T_{\delta\omega}(\delta\omega) = 1$. Note that $T_{\delta\omega}(\omega) = T_0(\omega - \delta\omega)$ and it is clear that $T_{\delta\omega}(+\Omega) \neq T_{\delta\omega}(-\Omega)$. Starting from the measured $E_{\rm PDH}(\delta x)$, one can retrieve the value $\delta\omega$ and, thereafter, the sideband transmission coefficients $T_{\delta\omega}(+\Omega)$ and $T_{\delta\omega}(-\Omega)$. For the sake of clarity we did not report the real experimental signals, but their pictorial view to better explain our analysis. See the text for details. 71

4.3 Homodyne traces referring to the coherent two-mode sideband state and the reconstructed $\boldsymbol{R}'$ and $\boldsymbol{\sigma}'$. The purities of the modes $\mathscr{S}$ and $\mathscr{A}$ are $\mu_{\rm s} = 0.99^{+0.01}_{-0.02}$ and $\mu_{\rm a} = 0.99^{+0.01}_{-0.01}$, respectively. Only the relevant elements are shown. 72

4.4 Homodyne traces referring to the squeezed two-mode sideband state and the reconstructed $\boldsymbol{R}'$ and $\boldsymbol{\sigma}'$. The noise reduction is 3.1 ± 0.3 dB for both the modes $\mathscr{S}$ and $\mathscr{A}$, wheres their purities are $\mu_{\rm s} = 0.68 \pm 0.07$ and $\mu_{\rm a} = 0.67 \pm 0.02$, respectively. Only the relevant elements are shown. 73

4.5 Homodyne traces referring to the squeezed-coherent two-mode sideband state and the reconstructed $\boldsymbol{R}'$ and $\boldsymbol{\sigma}'$. The noise reduction is 2.7 ± 0.3 dB for the $\mathscr{A}$ mode and 2.4 ± 0.2 dB for the $\mathscr{S}$ mode, whereas the purities are $\mu_{\rm s} = 0.68 \pm 0.07$ and $\mu_{\rm a} = 0.64 \pm 0.02$, respectively. Only the relevant elements are shown. 73

5.1 Tomographic reconstruction of the variances of the squeezed quadrature $\hat{x}$ (red lower dots) and of the anti-squeezed quadrature $\hat{p}$ (green upper dots) as a function of the total energy $N_{\rm tot}$, for $m = 14$ experimental STS. Dashed lines represent linear fits of the experimental data (see Eqs. (5.8)), from which we obtain the number of squeezed photons $n_{\rm s} \simeq 0.2$. The black dotted horizontal line is the shot-noise level at $\langle \Delta\hat{x}^2 \rangle = \langle \Delta\hat{p}^2 \rangle = 1$. 80

6.1 Homodyne traces referring to the vacuum squeezed states detected by using the SHD (top panel) and the IHA (bottom panel). We also report the corresponding reconstructed Wigner functions, the nonclassical depth (NCD) and the purity. 84

6.2 Measured quadrature variance as a function of θ for the SHD (blue) and the IHA (red). We also report the shot-noise level for comparison (black horizontal dashed line). 85

6.3 Homodyne trace referring to a coherent state (CS) by exploiting the IHA and the corresponding reconstructed Wigner function. The non classical depth (NCD) and the purity of the state are also reported. 86

6.4 Homodyne traces and reconstructed Wigner functions of phase squeezed CS (top panel) and amplitude squeezed CS (bottom panel) by using the IHA. Their non classical depths (NCD) and purities are also reported. 87

List of Tables

4.1 Reconstructed first moment vectors $\boldsymbol{R}$ and CMs $\boldsymbol{\sigma}_\Omega$ of the two-mode sideband states ρ_Ω corresponding to the states of Figs. 4.3, 4.4 and 4.5, respectively. 74

5.1 Characterization, via homodyne tomography, of the $m = 14$ experimental STS in terms of the position and momentum variances, total energy, squeezing factor and purity. The STS display squeezing in position and anti-squeezing in momentum coordinates ($r < 0$) . 80

Introduction

The field of quantum optics investigates how the quantum mechanical properties of optical fields can be manipulated, characterised, and utilised. Until recently, experiments in the field were motivated primarily by a desire to test properties of the microscopic world. As laser physics has advanced, however, many new quantum optical techniques have been developed in order to improve the technology utilised in many scientific research fields. In this context, the *continuous variable* (CV) regime has rapidly gained attention and a lot of progress has been made over the last years in the generation and detection of CV nonclassical states. From a theoretical point of view, although CV states lie in an infinite dimensional Hilbert space, many of them can be handled by mathematical techniques from finite-dimensional algebra. In particular, operations on the density matrix of the so-called *Gaussian states* can be achieved by manipulating the finite-dimensional covariance matrix. Within the family of Gaussian states, when we speak of "nonclassical" states, we are referring to *squeezed states* in which the variance of at least one of the canonical variables is reduced below the noise level of zero point fluctuations. These squeezed states have proved to be the most readily accessible optical fields with demonstrably quantum mechanical behaviour in the CV regime and they are considered to be at the heart of quantum mechanics.

This thesis experimentally examines their generation and detection processes by featuring the experimental setup improved during my Ph.D studies. Here, continuous-wave squeezed light is generated by a sub-threshold *optical parametric oscillator* (OPO), whose physical background consists in the *Spontaneous Parametric Down-Conversion* (SPD C).

Historically, the first observation of squeezing using an OPO cavity has been achieved by Wu et al. in 1986 [1]. They used a magnesium-doped lithium niobate ($MgO:LiNbO_3$) crystal embedded in a linear cavity and pumped at the second harmonic of the degenerate signal and idler fields as shown in Fig. 1 (a). The resulting squeezed vacuum state was analysed by means of a homodyne detector (HD), in which the weak signal under investigation is amplified by a bright laser beam called local oscillator (LO). The HD output was recorded and fed into a spectrum analyser that displays the power spectral density corresponding to the variance of the quadratures of the squeezed vacuum. The results are displayed on the right of Fig. 1 (b), where the root mean square noise voltage measured by the spectrum analyser is shown versus the LO phase. The squeezing reached in that experiment was about 3.5 dB below the vacuum noise (dashed line). Since then, significant advancements have been made to further develop this approach [2][3][3]. One of the most recent results reported a squeezing of about 15 dB [4]. Here

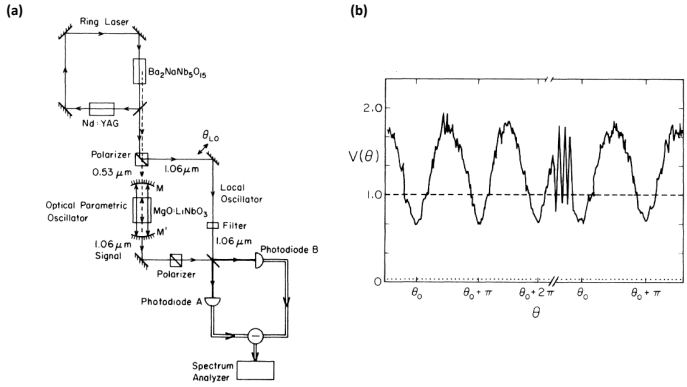

Figure 1: Wu et al. used degenerate parametric down-conversion ($MgO:LiNbO_3$) in a magnesium-doped lithium niobate crystal placed in a standing-wave cavity (M;M') **(a)**. The results are displayed on the right **(b)**, where the root mean square noise voltage measured by the spectrum analyzer is shown versus the phase of the local oscillator. The squeezing was about 3.5 dB below the vacuum noise (dashed line) [1].

the squeezing was generated by PDC in a cavity (OPA in Fig. 2) based on a periodically poled KTP (PPKTP) crystal. The measurements were performed by means of HD and were recorded with a Spectrum Analyzer. Fig. 2 (b) shows the OPA pump power dependence of the experimental squeezing and antisqueezing spectra.

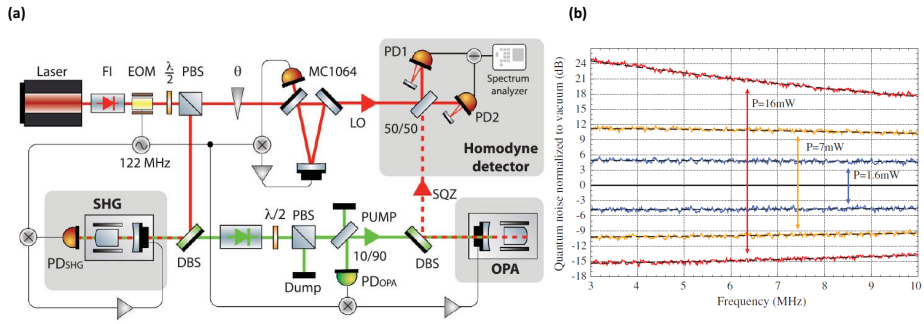

Figure 2: (**a**): Schematic of the experimental setup used in Ref. [4]. (**b**): Squeezing and antisqueezing spectra normalized to the vacuum noise level, experiment (continuous lines) and theory (dashed lines) for different OPA pump power (P). With P = 16 mW, a nonclassical noise reduction of 15.3 dB was obtained [4]

It is interesting to note that the basic experimental scheme used in 1986 is the same as that used today for generating highly efficient squeezing. The improvements in this area have mainly been concentrating on the technical aspects concerning with the primary cause of the squeezing degradation: the noise. The main types of noise mechanisms are related to intra-cavity losses, detection losses and phase noise. The remarkable developments of the low-noise electronics for phase locking, low loss optical components and high efficiency photodiodes and subsequent development of the optical homodyne tomography have enabled a considerable improvement of this system performances.

Initially, from the application point of view, the major advantages was awaited in the

improvement of the optical measurements resolution. In this scenario, the prominent example is the application in the gravitational waves (GWs) detection. The idea was proposed by Caves in 1981 [5] and was implemented first in the GEO600 gravitational wave detector [6] and later in the LIGO detector [7]. Although squeezed light has already been integrated into these GWs detectors, it has not yet been used in actual data acquisition runs. In Advanced LIGO, for example, the squeezing is expected to enhance the sensitivity by up to a factor of ten. Hopefully, such a detector will not only be able to prove the existence of GWs but provide information about their spatial distribution and temporal dynamics. This would result in a fundamentally new method for observing the universe, which has a potential to revolutionize the entire field of astronomy.

In addition to these applications, those relating to quantum information science stand out. This is a new and promising field of research that combines the techniques developed in quantum mechanics with those of information science which could not only provide better methods to interrogate the microscopic world but also real improvements to data storage, information processing and communication. Although originally the investigations of this area mostly focused on the discrete variable world, since the first experimental demonstration of CV quantum teleportation by Furusawa and al. [8] in 1998, a novel approach has been developed, which relies on canonical observables with continuous spectra. This quantum information with CVs offers many practical advantages over its discrete variable counterpart. Manipulating a single photon is a difficult experimental task. Single photons are hard to produce on demand and hard to detect efficiently. These experimental limitations make the implementation of quantum information based on discrete variables both difficult and expensive. In the regime of CVs, instead, nonclassical states of light can be deterministically generated in OPOs, precisely manipulated with linear optics and measured with very high efficiency in balanced HDs. All these features make the optical CV approach a very promising candidate for quantum information processing and communication. In particular, the squeezed states generated from the OPO are the main source of CV quantum states exploited in quantum information processing protocols [9]. One of the main obstacles for quantum information processing is the difficulty of the experimental implementation. Quantum information tasks require unprecedented precise control of complicated systems. For this reason, it is crucial to be able to control each step of the states generation and acquisition processes. Our experimental setup allows to accomplish this task successfully. Moreover, the generation/acquisition process is engineered in such a way that we are able to produce different kinds of nonclassical states on demand. Indeed, the states that SPDC can produce, namely the single- and dual-mode squeezed vacua, can be used as a starting point for the generation of several other quantum states of light and the ability to engineer this process is a central requirement for quantum communication, computing and metrology.

The thesis is divided into two Parts. The first Part introduces the theoretical and experimental techniques used in our laboratory to generate and detect nonclassical states in CV regime. After introducing the mathematical tools that we need for studying them and the theoretical basis of the detection process (Chap. 1), we discuss the physical background on which the experimental generation techniques are based (Chap. 2). Our experimental implementation is then shown in Chap. 3.

The results obtained from the performed work has been published or submitted for publication in international peer-reviewed journals:

- S. Cialdi, C. Porto, D. Cipriani, S. Olivares, and M. G. A. Paris. *Full quantum state reconstruction of symmetric two-mode squeezed thermal states via spectral homodyne de-*

tection and a state-balancing detector. Physical Review A **93**, 043805 (2016)

- A. Mandarino, M. Bina, C. Porto, S. Cialdi, S. Olivares, and M. G. A. Paris.*Assessing the significance of fidelity as a figure of merit in quantum state reconstruction of discrete and continuous-variable systems.* Physical Review A **93**, 062118 (2016)

- C. Porto, D. Rusca, S. Cialdi, A. Crespi, R. Osellame, D. Tamascelli, S. Olivares, and M. G. A. Paris. *Detection of squeezing by on-chip glass-integrated homodyne analyzer* Preprint arXiv:1710.04665 [quant-ph] (2017)

The second part of this thesis deals with these papers: the last three chapters feature each one of them individually and the speech recalls what we wrote in. In Chap. 4 we present a measurement scheme to fully reconstruct the class of symmetric two-mode squeezed thermal states which are those widely exploited in CV quantum technology. Chap. 5 presents the first application of the engineered generation/detection scheme implemented during my Ph.D. which allow us to generate different kinds of squeezed states on demand. The last chapter (Chap. 6) deal with the upgrade developed in order to miniaturise the HD system by exploiting a waveguide beam splitter inscribed in a glass substrate by femtosecond laser writing technology [10] [11]. This device has been embedded in our setup and for the first time, we have characterized nonclassical CV optical states by using it.

Part I

Nonclassical states of light

CHAPTER 1

Theoretical concepts

This Chapter is concerned with the description of quantum states in the continuous variable regime and the theoretical models and methods of analysis required for the experimental work of this thesis. In the first Sections we introduce the quantum mechanical description of electromagnetic field and its possible representation. In particular we introduce the mathematical tool used to describe the Gaussian states which are the field states relevant to our experiments. In the second part of this chapter we describe how to detect quantum states of light by introducing the optical homodyne detection. Finally we show the method to characterise these states.

1.1 The electromagnetic field quantization

In classical physics the properties and behaviour of light propagating in the free space are described by the source free Maxwell equations [12]:

$$\nabla \cdot \mathbf{B} = 0 \tag{1.1a}$$

$$\nabla \times \mathbf{E} = -\frac{\partial \mathbf{B}}{\partial t} \tag{1.1b}$$

$$\nabla \cdot \mathbf{D} = 0 \tag{1.1c}$$

$$\nabla \times \mathbf{H} = \frac{\partial \mathbf{D}}{\partial t} \tag{1.1d}$$

where $\mathbf{B} = \mu_0 \mathbf{H}$, $\mathbf{D} = \varepsilon_0 \mathbf{E}$, μ_0 and ε_0 being the magnetic permeability and electric permittivity of free space. Maxwell's equations are gauge invariant when no sources are present. A convenient choice of gauge for problems in quantum optics is the Coulomb gauge. In this gauge both $\mathbf{B}$ and $\mathbf{E}$ may be determined from a vector potential $\mathbf{A}(\mathbf{r},t)$ such that

$$\mathbf{B} = \nabla \times \mathbf{A} \tag{1.2a}$$

$$\mathbf{E} = -\frac{\partial \mathbf{A}}{\partial t} \tag{1.2b}$$

and

$$\nabla \cdot \mathbf{A} = 0 \tag{1.3}$$

From these conditions we find that $\mathbf{A}$ satisfies the wave equation:

$$\nabla^2 \mathbf{A}(\mathbf{r},t) = \frac{1}{c^2} \frac{\partial^2 \mathbf{A}(\mathbf{r},t)}{\partial t^2} \tag{1.4}$$

It is more convenient to deal with a discrete set of variables rather than with the whole continuum. We shall therefore describe the field restricted to a certain volume

of space and expand the vector potential in terms of a discrete set of orthogonal mode functions:

$$\mathbf{A}^{(+)}(\mathbf{r},t)=\sum_k c_k\mathbf{u}_k(\mathbf{r})\,e^{-\imath\omega_k t} \tag{1.5}$$

where ω_k is the angular frequency of the k-th mode and we have separated the vector potential into two complex terms $\mathbf{A}(\mathbf{r},t)=\mathbf{A}^{(-)}(\mathbf{r},t)+\mathbf{A}^{(+)}(\mathbf{r},t)$, with $\mathbf{A}^{(-)}(\mathbf{r},t)$ which contains all amplitudes varying as $e^{-\imath\omega t}$ for $\omega>0$ and $\mathbf{A}^{(-)}(\mathbf{r},t)$ which contains those varying as $e^{\imath\omega t}$ and $\mathbf{A}^{(-)}=(\mathbf{A}^{(+)})^*$. The Fourier coefficients c_k are constant for a free field and the mode functions depend on the boundary conditions of the physical volume under consideration. For example, the plane wave mode functions appropriate to a cubical volume of side L may be written as

$$\mathbf{u}_k(\mathbf{r})=L^{-3/2}\hat{\mathbf{e}}^{(\lambda)}e^{\imath\mathbf{k}\cdot\mathbf{r}} \tag{1.6}$$

Each component of the wave vector $\mathbf{k}$ takes the values

$$k_x=\frac{2\pi n_x}{L},\quad k_y=\frac{2\pi n_y}{L},\quad k_z=\frac{2\pi n_z}{L},\qquad n_x,n_y,n_z=0,\pm1,\pm2,\ldots \tag{1.7}$$

and the unit polarization vector $\hat{\mathbf{e}}^{(\lambda)}$, with λ=1,2, is required to be perpendicular to $\mathbf{k}$ by the transversality condition. The vector potential may now be written in the form

$$\mathbf{A}(\mathbf{r},t)=\imath\sum_k\left(\frac{\hbar}{2\omega_k\varepsilon_0}\right)^{1/2}\left[a_k\mathbf{u}_k(\mathbf{r})\,e^{-\imath\omega_k t}+a_k^*\mathbf{u}_k^*(\mathbf{r})\,e^{\imath\omega_k t}\right] \tag{1.8}$$

and the corresponding form for the electric field is

$$\mathbf{E}(\mathbf{r},t)=\imath\sum_k\left(\frac{\hbar\omega_k}{2\varepsilon_0}\right)^{1/2}\left[a_k\mathbf{u}_k(\mathbf{r})\,e^{-\imath\omega_k t}-a_k^*\mathbf{u}_k^*(\mathbf{r})\,e^{\imath\omega_k t}\right] \tag{1.9}$$

where $\hbar$ is Planck's constant and the normalization factors have been chosen such that the amplitudes a_k and a_k^* are dimensionless.

The transition from the classical to a quantum mechanical description of light is done via canonical quantization which changes the complex amplitudes a_k and a_k^* to the mutually adjoint operators $\hat{a}_k$ and $\hat{a}_k^\dagger$. [13][12]. Due to the bosonic character of photons, the operators follow the bosonic commutation relations

$$[\hat{a}_k,\hat{a}_{k'}]=\left[\hat{a}_k^\dagger,\hat{a}_{k'}^\dagger\right]=0,\quad\left[\hat{a}_k,\hat{a}_{k'}^\dagger\right]=\delta_{kk'} \tag{1.10}$$

With the quantization the electric field may then be featured as an ensemble of independent harmonic oscillators with frequency ω_k obeying the above commutation relations. Each of these oscillators describes the dynamical behaviour of one individual mode independently of the other modes. The quantum state of each mode can be described by a state vector $|\Psi\rangle_k$ of the Hilbert space corresponding to the mode k and the state of the entire field is then defined in the tensor product space of the Hilbert spaces for all the modes. The Hamiltonian for the electromagnetic field is given by

$$H=\frac{1}{2}\int\left(\varepsilon_0\mathbf{E}^2+\mu_0\mathbf{H}^2\right)d\mathbf{r}. \tag{1.11}$$

Substituting 1.9 for **E** and the equivalent expression for **H**, the Hamiltonian may be reduced to the form [12]

$$H = \sum_k \hbar\omega_k \left(a_k^\dagger a_k + \frac{1}{2} \right) \tag{1.12}$$

that is the Hamiltonian of a set of quantum harmonic oscillators (h. o.) with frequencies ω_k. It represents the number of photons in each mode k multiplied by the photon energy $\hbar\omega_k$, plus $\frac{1}{2}\hbar\omega_k$ representing the energy of the vacuum fluctuations in each mode.

1.2 Quantum states of light

Because of the analogies of the e.m. field with a set of harmonic oscillators, we can apply the knowledge of the h.o. states to describe the states of the e.m. field. Below we will consider two possible representations of the e.m. field.

1.2.1 Fock states

The eigenstates of the number operator $N_k = a_k^\dagger a_k$ are the number or Fock states $|n_k\rangle$ and the corresponding eigenvalues are the integer numbers n_k, namely:

$$a_k^\dagger a_k |n_k\rangle = n_k |n_k\rangle \tag{1.13}$$

where the application of the creation and annihilation operators to the number states yields

$$a_k |n_k\rangle = n_k^{1/2} |n_k - 1\rangle, \quad a_k^\dagger |n_k\rangle = (n_k + 1)^{1/2} |n_k + 1\rangle \tag{1.14}$$

The ground state of the oscillator (or vacuum state of the field mode) is defined by

$$a_k |0\rangle = 0 \tag{1.15}$$

and its energy is given by

$$\langle 0| \hat{H} |0\rangle = \frac{1}{2} \sum_k \hbar\omega_k \tag{1.16}$$

The state vectors for the higher excited states may be obtained from the vacuum by successive application of the creation operator

$$|n_k\rangle = \frac{\left(a_k^\dagger\right)^{n_k}}{(n_k!)^{1/2}} |0\rangle, \quad n_k = 0, 1, 2, \ldots \tag{1.17}$$

The number states are orthogonal

$$\langle n_k | m_k \rangle = \delta_{mn} \tag{1.18}$$

and complete

$$\sum_{n_k=0}^{\infty} |n_k\rangle \langle n_k| = 1 \tag{1.19}$$

Since the norm of these eigenvectors is finite, they form a complete set of basis vectors for a Hilbert space.

1.2.2 Coherent States

While the number states form a useful representation when the number of photons is very small, they are not the most suitable representation for optical fields where the total number of photons is large. Despite the fact that the number states of the electromagnetic field have been used as a basis for several problems in quantum optics including some laser theories, a more appropriate basis for many optical fields is given by the coherent states [12] which are the quantum mechanical states closer to a classical description of the field and the closest approximation of the output state of a laser.

These states are the eigenvectors of the annihilation operator:

$$\hat{a}\,|\alpha\rangle = \alpha\,|\alpha\rangle \quad \alpha \in \mathbb{C} \tag{1.20}$$

The coherent state contains an indefinite number of photons. This may be highlighted by considering its expansion in the number states basis:

$$|\alpha\rangle = e^{-|\alpha|^2/2} \sum \frac{\alpha^n}{(n!)^{1/2}}\,|n\rangle \tag{1.21}$$

We note that the probability distribution of photons in a coherent state is a Poisson distribution

$$P(n) = |\langle n|\alpha\rangle|^2 = \frac{|\alpha|^{2n}\, e^{|\alpha|^2}}{n!} \tag{1.22}$$

where $|\alpha|^2$ is the mean number of photons, $\langle \hat{n} \rangle = |\alpha|^2$.

Two coherent states $\langle\alpha\rangle$ and $\langle\beta\rangle$ are not orthogonal:

$$|\langle \alpha \mid \beta \rangle|^2 \neq 0 \tag{1.23}$$

and they are over-complete. In fact we can see that the identity can be resolved as

$$\frac{1}{\pi} \int_{\mathbb{C}} |\alpha\rangle \langle\alpha| = \hat{I} \tag{1.24}$$

These states are most easily generated using the unitary displacement operator

$$D(\alpha) = exp\left(\alpha a^{\dagger} - \alpha^* a\right) \tag{1.25}$$

where α is an arbitrary complex number. The coherent state $|\alpha\rangle$ is generated by operating with D(α) on the vacuum state

$$|\alpha\rangle = D(\alpha)\,|0\rangle \tag{1.26}$$

1.2.3 Thermal states

The photon number states and the coherent states are two pure states. Another quite common state is the thermal state, which is a mixed state, being a mixture of Fock states. If the state of the radiation is at thermal equilibrium with a heat bath of temperature T, it is described by the density operator written as[12] :

$$\hat{\rho}_{th}\,(N_{th}) = \frac{1}{1+N_{th}} \sum_{n=0}^{\infty} \left(\frac{N_{th}}{1+N_{th}}\right)^n |n\rangle \langle n| \tag{1.27}$$

where the mean number of thermal photons, N_{th} is given by:

$$N_{th} = \left[exp\left(\frac{\hbar\omega}{k_B T}\right) - 1 \right]^{-1} \tag{1.28}$$

with ω the radiation frequency and k_B the Boltzmann constant.

Note that if $N_{th} = 0$, we have $\hat{\rho}_{th}(0) = |0\rangle\langle 0|$ that is the vacuum state.

1.3 Quadrature operators

For the sake of simplicity we consider now a monochromatic electric field. By reorganising the eq. 1.9, we can rewrite the electric field vector **E** (**r**,t) as [13]

$$\mathbf{E}(\mathbf{r},t) = E_0 \left(\alpha(\mathbf{r},t) e^{-\imath\omega t} + \alpha^*(\mathbf{r},t) e^{\imath\omega t} \right) \mathbf{p}(\mathbf{r},t) \tag{1.29}$$

where we have explicitly included the polarization contribution in the polarization vector **p**(**r**,t), and now α(**r**,t) is the complex amplitude function:

$$\alpha(\mathbf{r},t) = \alpha_0(\mathbf{r},t) e^{\imath\phi(\mathbf{r},t)} \tag{1.30}$$

where α_0(**r**, t) is the (dimensional) magnitude of the field and ϕ(**r**, t) is the phase term which determines the shape of the wave front. For example, in the case of a plane wave with wave vector k = ω/c and moving along the positive direction of z-axis we have $\alpha(\mathbf{r},t) = \alpha_0 e^{\imath kz}$. This description of a wave allows us to introduce the *quadrature amplitudes*, which are proportional to the real and imaginary parts of the complex amplitude:

$$X_1(\mathbf{r},t) = \alpha(\mathbf{r},t) + \alpha^*(\mathbf{r},t) \tag{1.31a}$$

$$X_2(\mathbf{r},t) = \imath\left[\alpha(\mathbf{r},t) - \alpha^*(\mathbf{r},t)\right] \tag{1.31b}$$

In this notation we can explicitly write the absolute phase as:

$$\phi_0 = \arctan\left(\frac{X_2(\mathbf{r},t)}{X_1(\mathbf{r},t)}\right) \tag{1.32}$$

and rewrite the eq. 1.29 as

$$\mathbf{E}(\mathbf{r},t) = E_0 \left(X_1(\mathbf{r},t)\cos\omega t + X_2(\mathbf{r},t)\sin\omega t \right) \mathbf{p}(\mathbf{r},t) \tag{1.33}$$

In this way we can introduce a common graphical representation of classical waves called *phasor diagram* which is a two dimensional diagram of the values X_1 and X_2 as shown in Fig. 1.1 (a): the field in a given space point **r** at time t corresponds to a point in the X_1-X_2 plane and each wave corresponds to one particular vector of length *a* from the origin to the point (X_1, X_2). The magnitude of the wave is given by the distance of the point from the origin and the relative phase, ϕ_0 is given by the angle with the X_1 axis, since the absolute phase is arbitrary. The wave can have fluctuations or modulations in both amplitude and phase. Such variations correspond to fluctuations in the quadrature values and we can describe the time dependent wave with the complex amplitude

$$\alpha(t) = \alpha_0 + \delta X_1(t) + \imath\delta X_2(t) \tag{1.34}$$

In the limit $\alpha_0 \gg \delta X_1$(t),δX_2(t), which means that the waves change or fluctuate only very little around a fixed value α_0, we see (Fig. 1.1 (b)) that δX_1(t),δX_2(t) describe the

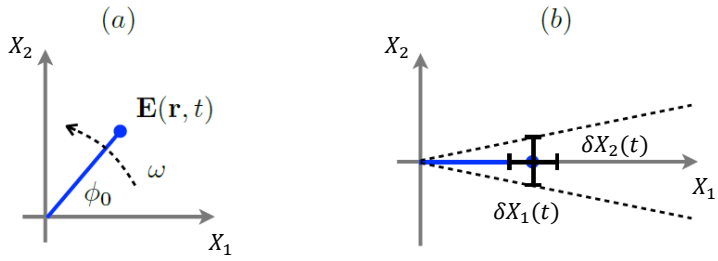

Figure 1.1: (a) Phasor representation of the classical wave. In (b) it is highlighted that the fluctuations of the quadratures correspond to amplitude and phase fluctuations

changes in the amplitude and phase respectively. Therefore, one usually refers to them as the *amplitude* and *phase quadratures*.

If the above considerations are applied to the quantized form of the electromagnetic field, we can define the *quadrature operators*:

$$\hat{X}_1 = \hat{a} + \hat{a}^\dagger \tag{1.35}$$

$$\hat{X}_2 = -\imath\left(\hat{a} - \hat{a}^\dagger\right) \tag{1.36}$$

which are the *amplitude quadrature operator* and *the phase quadrature operator*, respectively. The electric field observable $\hat{E}$ with a certain frequency ω, by reorganising the phase term in the Eq. 1.9, becomes:

$$\hat{E} = \left(\frac{\hbar\omega}{2\varepsilon_0 V}\right)^{1/2} \frac{1}{2}\left(\hat{a}e^{-\imath\theta} + \hat{a}^\dagger e^{+\imath\theta}\right) = \left(\frac{\hbar\omega}{2\varepsilon_0 V}\right)^{1/2} \hat{X}(\theta) \tag{1.37}$$

where $\hat{X}(\theta)$ is the generic *quadrature operator* which define any quadrature between the amplitude and phase quadrature:

$$\hat{X}(\theta) = \left(\hat{a}e^{-\imath\theta} + \hat{a}^\dagger e^{+\imath\theta}\right) = \hat{X}_1 \cos\theta + \hat{X}_2 \sin\theta \tag{1.38}$$

where we have used $\hat{X}_1 = \hat{X}(0)$ and $\hat{X}_2 = \hat{X}\left(\frac{\pi}{2}\right)$.

From the commutation relations 1.10, we see that $\hat{X}_1$ and $\hat{X}_2$ obey the commutator

$$\left[\hat{X}_1, \hat{X}_2\right] = 2i \tag{1.39}$$

The Heisenberg uncertainty principle [12] states that it is impossible to simultaneously obtain precise knowledge of two non-commuting observables. This means that the product of the uncertainties of simultaneous measurements on two arbitrary observables $\hat{A}$ and $\hat{B}$ is bounded by

$$\Delta\hat{A}\Delta\hat{B} \geq \frac{1}{2}\left|\left[\hat{A}, \hat{B}\right]\right| \tag{1.40}$$

where $\Delta\hat{A}$ $\Delta\hat{B}$ are the standard deviation of measurements of A end B which are given by:

$$\Delta\hat{A} = \sqrt{\left\langle\hat{A}^2\right\rangle - \left\langle\hat{A}\right\rangle^2} \tag{1.41}$$

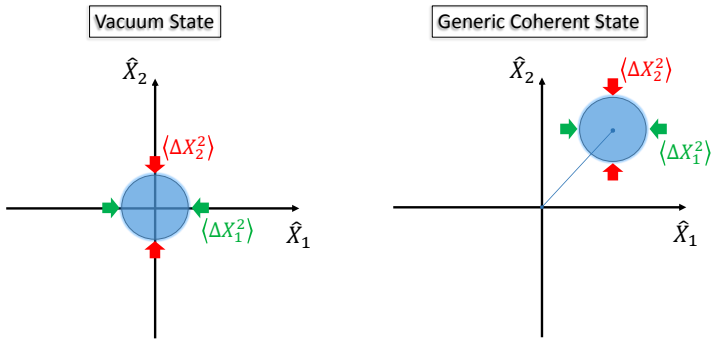

Figure 1.2: Representations in the phasor diagram of the vacuum and generic coherent states.

Therefore, due to eq. 1.39, the uncertainty principle constrains the variances of the operators $\hat{X}_1$ and $\hat{X}_2$ in any state to

$$\langle \Delta \hat{X}_1^2 \rangle \langle \Delta \hat{X}_1^2 \rangle \geq 1 \tag{1.42}$$

Let us consider a coherent state $|\alpha\rangle$. If we calculate the expectation of the quadrature operator we find:

$$\langle \hat{X}(\theta) \rangle = \langle \alpha | \hat{a} | \alpha \rangle e^{-\imath\theta} + \langle \alpha | \hat{a}^\dagger | \alpha \rangle e^{\imath\theta} = 2\Re \left[\alpha e^{-\imath\theta} \right] \tag{1.43}$$

and if we put $\alpha = (X_1 + \imath X_2)$, with $X_1, X_2 \in R$, we obtain:

$$\langle \hat{X}(\theta) \rangle = X_1 \cos\theta + X_2 \sin\theta \tag{1.44}$$

as for a classical wave (see Eq. 1.33). However, whereas in the classical case the uncertainty of the expectation of the quadrature is null, in the present case we have

$$\left\langle \Delta \hat{X}(\theta)^2 \right\rangle = \left\langle \hat{X}(\theta)^2 \right\rangle - \langle \hat{X}(\theta) \rangle^2 = 1 \quad \forall\theta \tag{1.45}$$

and, in particular:

$$\langle \Delta \hat{X}_1^2 \rangle \langle \Delta \hat{X}_2^2 \rangle = 1 \tag{1.46}$$

which means that a coherent state is a *minimun uncertainty states* among the classical states.

As in the classical case, the quadrature operators allow us to represent a state graphically by using a *phasor diagram* that is a plot of $\hat{X}_2$ versus $\hat{X}_1$. In such a diagram any particular coherent state $|\alpha\rangle$ is equivalent to an area whose size is given by the variances $\langle \Delta \hat{X}_1^2 \rangle$ and $\langle \Delta \hat{X}_1^2 \rangle$ and therefore describes the extent of the uncertainty distribution. This area, centered around the point given by the value ($\langle X_1 \rangle$, $\langle X_2 \rangle$) for the state, is usually represented just by a circle as shown in Fig. 1.2.

In agreement with the Eqs. 1.45 and 1.46, we see that a coherent state is represented by a circle whose uncertainty area is symmetric and constant, independent of the state intensity.

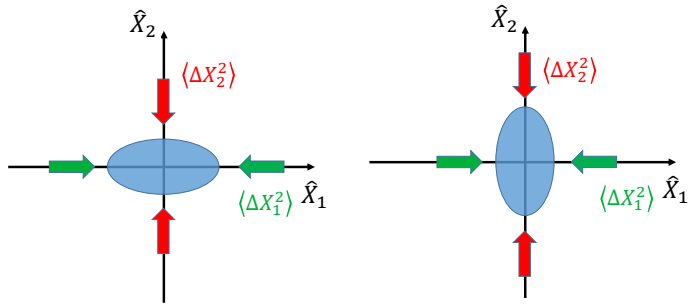

Figure 1.3: Representations in the phasor diagram of the amplitude (on the right) and phase squeezed (on the left) vacuum states.

1.4 Squeezed states

We have seen that the ground state of an electromagnetic oscillation is the vacuum state or in other words the state $|0\rangle$ with zero photons and that the amplitude and phase quadratures for any electromagnetic oscillation must satisfy an Heisenberg uncertainty relation. So even though the vacuum state has no photons, its electromagnetic field still fluctuates. In fact $\langle \Delta \hat{X}_1^2 \rangle = \langle \Delta \hat{X}_2^2 \rangle = 1$, so that the fluctuations of the amplitude and phase quadratures of a vacuum state are equal. The fluctuations of the vacuum state pose a limit to most optical measurement devices and it is sometimes called the quantum noise limit, or from an engineering point of view the shot noise limit. Besides we have seen that a coherent state (whereby we can represent the output of an ideal laser) has the same fluctuations as a vacuum state.

Now, we want to introduce states that have noise properties different from those of the vacuum and coherent states. They are the so-called *squeezed states* in which the noise of the electric field at certain phases falls below that of the vacuum state, that is, states for which either $\langle \Delta \hat{X}_1^2 \rangle < 1$ or $\langle \Delta \hat{X}_1^2 \rangle < 1$. Of course, the Heisenberg uncertainty principle must still be satisfied, so that the noise in the non-squeezed quadrature must be greater than unity. In fact, due to the optical loss and other imperfections present in any real experiment, the product $\langle \Delta \hat{X}_1^2 \rangle \langle \Delta \hat{X}_2^2 \rangle$ is always greater than unity. The representation of this kind of state in the phasor diagram is shown in Fig. 1.3.

1.5 Gaussian states

Generally quantum states are classified according to their Gaussian or non-Gaussian nature. The coherent state is the most prominent example of a Gaussian state, while the number state is an example of a non-Gaussian state. Here we will focus on the Gaussian states because they are the ones considered throughout this thesis. The basic reason is that this class of states is at the heart of quantum information processing with continuous variables [14]. The observation that the vacuum state of quantum electrodynamics is itself a Gaussian state, together with the fact that the quantum evolution achievable with current technology is described by Hamiltonian operators at most bilinear in the quantum fields explains why the states commonly produced in laboratories are Gaussian. In fact, as we will show below, bilinear evolutions preserve the Gaussian character of the vacuum state and this remains also valid when the evolution of a state occurs in a

noisy channel.

1.5.1 Basic notation and definition of Gaussian state

Any quantum state can be fully characterised by its density matrix $\hat{\rho}$, also called density operator. [12] In particular, a n-mode state described by the density matrix $\hat{\rho}$ is a Gaussian state if its characteristic function [14]:

$$\chi[\hat{\rho}](\mathbf{\Lambda}) = Tr\left[\hat{\rho}\exp\left\{-\imath\mathbf{\Lambda}^T\mathbf{\Omega}\hat{\mathbf{R}}\right\}\right] \tag{1.47}$$

is Gaussian, namely, if $\chi[\hat{\rho}](\mathbf{\Lambda})$ can be written in the following form:

$$\chi[\hat{\rho}](\mathbf{\Lambda}) = \exp\left\{-\frac{1}{2}\mathbf{\Lambda}^T\mathbf{\Omega}\boldsymbol{\sigma}\mathbf{\Omega}^T\mathbf{\Lambda} - \imath\mathbf{\Lambda}^T\mathbf{\Omega}\langle\hat{\mathbf{R}}\rangle\right\} \tag{1.48}$$

with $\mathbf{\Lambda} = (a_1, b_1, ..., a_n, b_n)^T \in \mathbf{R}^{2n}$ and Ω is the symplectic matrix defined as $\mathbf{\Omega} = \bigoplus_{k=1}^{n}\boldsymbol{\omega}$, $\boldsymbol{\omega} = \left(\begin{smallmatrix}0 & 1\\ -1 & 0\end{smallmatrix}\right)$. In order to simplify the formalism we have introduced the vector of operators $\hat{\mathbf{R}} = (\hat{q}_1, \hat{p}_1, \cdot\cdot, \hat{q}_{,n}, \hat{p}_n)^T$ and we have defined the covariance matrix $\boldsymbol{\sigma}$ (CM) as:

$$\sigma_{kl} \equiv [\sigma]_{kl} = \frac{1}{2}\langle\hat{R}_k\hat{R}_l + \hat{R}_l\hat{R}_k\rangle - \langle\hat{R}_k\rangle\langle\hat{R}_l\rangle \tag{1.49}$$

By Fourier transform of the characteristic function 1.47 , we obtain the so-called Wigner function of $\hat{\rho}$[12][14]:

$$W[\hat{\rho}](\mathbf{X}) = \frac{1}{(2\pi^2)^n}\int_{\mathbf{R}^{2n}} d^{2n}\mathbf{\Lambda}\exp\left\{\imath\mathbf{\Lambda}^T\mathbf{\Omega}\mathbf{X}\right\}\chi[\hat{\rho}](\mathbf{\Lambda}) \tag{1.50}$$

where $\mathbf{X} = (\mathbf{x_1}, \mathbf{y_1}, ..., \mathbf{x_n}, \mathbf{y_n})^{\mathbf{T}} \in \mathbb{R}^{\mathbf{2n}}$. In the case of the Gaussian state it become:

$$W[\hat{\rho}](\mathbf{X}) = \frac{exp\left\{-\frac{1}{2}\left(\mathbf{X} - \langle\hat{\mathbf{R}}\rangle\right)^T\boldsymbol{\sigma}^{-1}\left(\mathbf{X} - \langle\hat{\mathbf{R}}\rangle\right)\right\}}{\pi^n\sqrt{det[\boldsymbol{\sigma}]}} \tag{1.51}$$

that is still Gaussian. Therefore a Gaussian state is fully characterized by its CM and its first-moments vector.

1.5.2 Linear and bilinear Hamiltonians

In order to preserve Gaussian states, a Hamiltonian should be linear or bilinear in the fields mode [14]. This kind of Hamiltonian can be experimentally realized by means of parametric processes in quantum optical systems which involves parametric interactions in nonlinear media. The most general Hamiltonian of this kind can be written as:

$$H = \underbrace{\sum_{k=1}^{n} g_k^{(1)}\hat{a}_k^\dagger}_{(i)} + \underbrace{\sum_{k\geq l=1}^{n} g_{kl}^{(2)}\hat{a}_k^\dagger\hat{a}_l}_{(ii)} + \underbrace{\sum_{k,l=1}^{n} g_{kl}^{(3)}\hat{a}_k^\dagger\hat{a}_l^\dagger}_{(iii)} + h.c. \tag{1.52}$$

The first block (i) is linear in the field modes. The corresponding unitary transformations are the set of displacement operators we used to define coherent states, $|\alpha\rangle = D(\alpha)|0\rangle$, that is the unitary evolution of the vacuum through the displacement operator.

The second block (ii) appearing in the Hamiltonian 1.52 represents two different physical processes. The first process refers to the terms with l=k in (ii), i.e. proportional

to $g^{(2)}\hat{a}_k^\dagger \hat{a}_k$ and describes the free evolution of the modes: in most cases these terms can be eliminated by choosing a suitable interaction picture. The effect of free evolution is to add an overall phase shift that, for single-mode fields, has no physical meaning, but it is of extreme relevance in the case of interference phenomena involving different beams of light, such as the interferometric scheme used to implement the homodyne detection [14].

If l≠k we deal with a second process which describes a linear mixing of two modes and, in the quantum optics context, the simplest example corresponds to a Hamiltonian of the form $H \propto \hat{a}^\dagger \hat{b} + \hat{b}^\dagger \hat{a}$, where for the sake of simplicity we consider a system of two modes $\hat{a} \equiv \hat{a}_1$ and $\hat{b} \equiv \hat{a}_2$. This Hamiltonian describes the action of a beam splitter.

In the particular case of quantum optics, the last block (iii) describes $\chi^{(2)}$ non-linear interactions in which a photon in the input is converted into two photons, conserving both the energy and the momentum, and which we will illustrate in Chap.2.

- **Single-mode squeezing**

  If in these processes two photons are emitted into the same mode $\hat{a}$, we obtain the single-mode squeezing transformations, which, thus, correspond to Hamiltonians of the form $H \propto \left(\hat{a}^\dagger\right)^2 + h.c.$.

  The single-mode squeezing operator is usually written as:

$$S(\xi) = exp\left\{\frac{1}{2}\left[\xi\left(\hat{a}^\dagger\right)^2 - \xi^* \hat{a}^2\right]\right\} \tag{1.53}$$

  where $\xi = re^{\iota\Psi}$.

- **Two-mode squeezing**

  The two-mode squeezing transformations correspond to Hamiltonians of the form $H \propto \hat{a}^\dagger \hat{b}^\dagger + h.c.$ and describe $\chi^{(2)}$ nonlinear interactions introduced in the previous subsection but with the two photons emitted in different modes.

  The evolution operator is usually written as:

$$S_2(\xi) = exp\left\{\frac{1}{2}\left[\xi \hat{a}^\dagger \hat{b}^\dagger - \xi^* \hat{a}\hat{b}\right]\right\} \tag{1.54}$$

In conclusion a generic Gaussian state can be written as:

$$\hat{\rho} = D(\alpha)\, S(\xi)\, \nu_{th}(N)\, S^\dagger(\xi)\, D^\dagger(\alpha) \tag{1.55}$$

where $\nu_{th}(N)$ is the thermal state introduced in Sec. 1.2.3. In particular, for the vacuum state we have $\alpha = \xi = N = 0$ whose corresponding Wigner function is shown in Fig. 1.4. Recalling the analogy between the quadrature operators and position- and momentum-like operators:

$$\hat{q} = \sqrt{\frac{\hbar}{2\omega}}\left(\hat{a} + \hat{a}^\dagger\right) \qquad \hat{p} = -\iota\sqrt{\frac{\hbar\omega}{2}}\left(\hat{a} - \hat{a}^\dagger\right) \tag{1.56}$$

it is easy to immediately understand that the uncertainty areas which are shown in the phasor diagrams in Sec. 1.3 are simplified representations of the Gaussian Wigner functions [13]. They are the levels curves at the level of the quadrature variances as shown in Fig. 1.4 for the vacuum state. Wigner functions corresponding to a coherent state, and displaced phase and amplitude squeezed states are instead shown in Fig. 1.5.

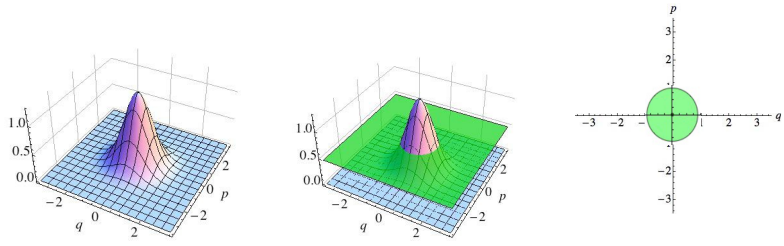

Figure 1.4: The Gaussian Wigner function for the vacuum state. The level' curve at the level of the quadrature variances is the uncertainty area in the two-dimensional phasor diagram.

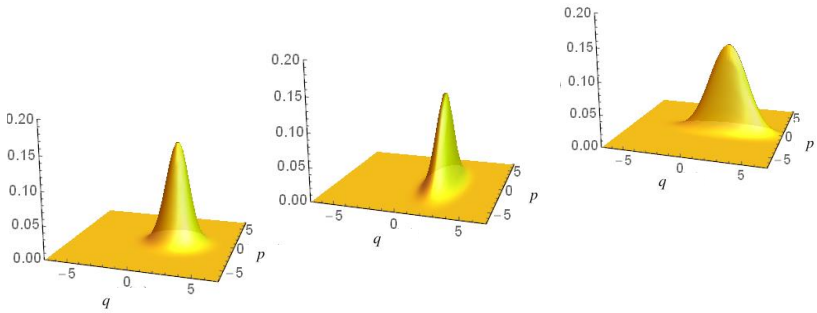

Figure 1.5: Wigner functions for a coherent state, a displaced phase squeezed state and a displaced amplitude squeezed state from left to right.

1.6 Detecting quantum states of light

Our purpose is to perform phase-sensitive measurements of the electric field in an electromagnetic mode, i.e. of $\hat{X}(\theta)$ for all values of θ. In this way, indeed, we can reconstruct the Wigner function of the mode's quantum state. Unfortunately, a single instrument able to perform such a measurement does not exist. Typical oscillation frequencies of the light fields are hundreds of terahertz (10^{14}-10^{15} Hz), and a detector that can follow such fast changes does not exist. Anyway there is an experimental technique that allows to do phase-sensitive measurements of the electric field using regular, "slow" detectors. This method is known as balanced Homodyne Detection (HD). The balanced HD theoretically developed by Yuen and Chan in 1983 [15] and subsequently implemented by Abbas et al. [16], has been widely applied to many quantum optics experiments as an effective tool to characterize the non-classical states of light in either the time [17][18][19][20][21][22][23][24] or the frequency [25, 26, 27, 28, 29, 30, 31, 32, 33, 34, 35, 36, 37, 38] domain. It provides the measurement of single-mode quadratures through the mixing of the field under investigation, called signal, which is usually weak, with a highly excited semiclassical field (e.g. a relatively strong laser beam) at the same frequency, called local oscillator (LO), by using a relatively simple interference setup. The LO has to be phase locked to the input, otherwise it cannot provide a phase reference to distinguish between the quadratures. For this reason, the signal and the LO are usually

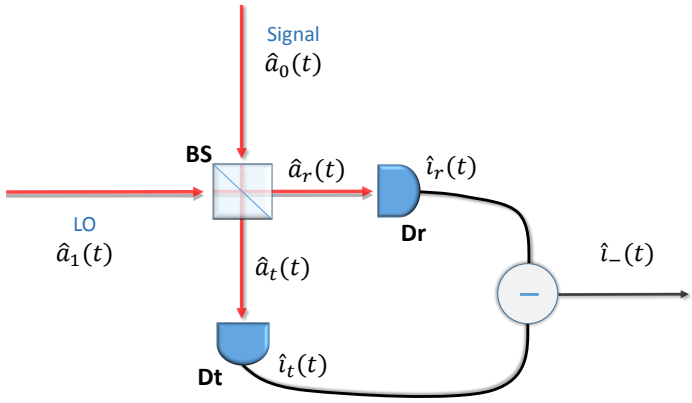

Figure 1.6: Schematic diagram of the Homodyne Detector.

generated by a common source, so that they have a fixed phase relation.

The schematic diagram of a HD is reported in Fig.1.6: Let $\hat{a}_0$(t) be the signal mode which is in the state $\hat{\rho}$ under investigation. It interferes at a beam splitter (BS) with a second mode $\hat{a}_1$(t) excited in a coherent state, $\hat{a}_1$(t)=$|\alpha| e^{\imath\phi} e^{-\imath\omega_0 t}$, with $|\alpha| \gg 1$, as shown in Fig. 1.6. The BS produces the mixing of this two incident optical modes and by using its quantum mechanical description, the reflected and transmitted modes, $\hat{a}_r$ and $\hat{a}_t$, can be expressed as [13]

$$\begin{pmatrix} \hat{a}_r \\ \hat{a}_t \end{pmatrix} = \begin{pmatrix} \imath\sqrt{R} & \sqrt{T} \\ \sqrt{T} & \imath\sqrt{R} \end{pmatrix} \begin{pmatrix} \hat{a}_0 \\ \hat{a}_1 \end{pmatrix} \tag{1.57}$$

where R and T are the BS reflection and transmission coefficients, respectively. After the BS, the two modes are detected by two identical photodetectors, Dr and Dt. Photodetection of a CW laser beam is described by the photoelectric effect, with electrons being liberated from a material when it is subjected to a radiant field. Within the bandwidth of the detectors, the produced photocurrent is directly proportional to the number of photons in the field, i.e. $\hat{\imath}_i = \eta_i \hat{a}_i^\dagger \hat{a}_i$, with $i = r,t$, where η_i is the detection efficiency which contains all processes that reduce the conversion of the light into a current [13]. In what follows, we will assume η_i to be one for the sake of simplicity. The photocurrents are subtracted from each other and the difference photocurrent, $\hat{\imath}_-$, can be written as

$$\begin{aligned} \hat{\imath}_-(t) &\propto (R-T)\,\hat{a}_1^\dagger(t)\,\hat{a}_1(t) + 2\imath\sqrt{RT}\left(\hat{a}_1^\dagger \hat{a}_0 - \hat{a}_1 \hat{a}_0^\dagger\right) + (T-R)\,\hat{a}_0^\dagger(t)\,\hat{a}_0(t) \\ &\approx (R-T)\,\hat{a}_1^\dagger(t)\,\hat{a}_1(t) + 2\imath\sqrt{RT}\left(\hat{a}_1^\dagger \hat{a}_0 - \hat{a}_1 \hat{a}_0^\dagger\right) \end{aligned} \tag{1.58}$$

where we have neglected the term $(T-R)\,\hat{a}_0^\dagger(t)\,\hat{a}_0(t)$ because the LO beam is more powerful than the signal beam.

If R=T, it can be proved that i_(t) is proportional to $\hat{X}(\theta)$. In fact, we can write the time varying field annihilation operator $\hat{a}$(t) as

$$\hat{a}_0(t) = e^{-\imath\omega_0 t} \int d\omega \hat{a}(\omega) e^{-\imath\omega t} \stackrel{def}{=} e^{-\imath\omega_0 t} \widetilde{a}(t) \tag{1.59}$$

i.e. as Fourier transform of $\hat{a}(\omega)$, where ω now denotes the frequency separation from the laser carrier ω_0. With $\widetilde{a}$ we are considering only the slowly varying part of the signal without the carrier. By considering Eq. 1.59, we can rewrite Eq. 1.58 as

$$\begin{aligned}\hat{i}_{-}(t) &\propto 2\sqrt{RT}\,|\alpha|\left(\widetilde{a}(t)\,e^{-\imath\phi+\imath\frac{\pi}{2}}+\widetilde{a}(t)^{\dagger}\,e^{+\imath\phi-\imath\frac{\pi}{2}}\right)\\ &= 2\sqrt{RT}\,|\alpha|\left(\widetilde{a}(t)\,e^{-\imath\theta}+\widetilde{a}(t)^{\dagger}\,e^{+\imath\theta}\right)\end{aligned} \tag{1.60}$$

where we have replaced $\hat{a}_1$(t) with $|\alpha|\,e^{\imath\phi}e^{-\imath\omega_0 t}$.

Finally, by recalling the definition of electric field observable $\hat{X}$(t,θ) in 1.38, we have

$$\hat{i}_{-}(t) \propto 4\sqrt{RT}\,|\alpha|\,\hat{X}(t,\theta)\,. \tag{1.61}$$

It's worth noting that the "fast term" ω_0 is removed by the presence of the LO at the same frequency and what we observe at time t is a photocurrent proportional to the signal field amplified by the LO. Besides the phase θ can be selected by changing the LO phase.

The state which we observe cannot be defined independently of the measurement apparatus because the latter has its response time proportional to spectral bandwidth: $\Delta t \propto 1/(\Delta\omega/2\pi)$. For instance, the main photons number carried by the measured coherent state is the number which on average comes in this response time. Therefore the expression 1.59 becomes

$$\hat{a}_0(t) = e^{-\imath\omega_0 t}\int d\omega F(\omega)\,\hat{a}(\omega)\,e^{-\imath\omega t} \overset{def}{=} e^{-\imath\omega_0 t}\widetilde{a}(t) \tag{1.62}$$

where F(ω) is the apparatus spectral response function.

Theoretically, if the quantum states, such as squezeed states, are generated in a continuous nonlinear process, it could be observed by measuring the variance of the homodyne detector output photocurrent as a function of the LO phase. In a real situation, however, this measurement is obscured by many frequency dependent noises which are present in an experimental system. Fortunately, such technical (classical) noises often occur within specific frequency bands. Among them the most difficult to eliminate are the laser classical noise and the detector electronic noise which are low frequency noises. The idea is to bypass them by shifting the signal towards higher frequencies (few MHz). For this purpose the HD shown in Fig. 1.6 can be modified by adding a amplitude/phase modulator, a phase shifter and a mixer, as shown in fig. 1.7.

Let us now see how this detector works. The signal field is modulated by using a phase or amplitude modulator (PM/AM). In order to understand its action on $\hat{a}_0$, we start from a classical description and then switch to the quantum one. Therefore we consider the classical electric field at a certain position at frequency ω_0

$$\alpha(t) = \alpha_0 e^{\imath\omega_0 t} \tag{1.63}$$

where we omit the complex conjugate term for simplicity, and we focus on the amplitude modulation. A beam of light which is amplitude modulated by a fraction 2δ at the frequency Ω can be described by [13]

$$\begin{aligned}a(t) &= a_0\left(1-\delta\left(1-\cos\Omega t\right)\right)e^{\imath\omega_0 t}\\ &= a_0\left(1-\delta\right)e^{\imath\omega_0 t}+a_0\frac{\delta}{2}\left[e^{\imath(\omega_0+\Omega)t}+e^{\imath(\omega_0-\Omega)t}\right]\end{aligned} \tag{1.64}$$

Here we see that the effect of the modulation is to create two frequency components at $\omega_0-\Omega$ and $\omega_0+\Omega$: these are known as the upper and lower *sidebands*, respectively,

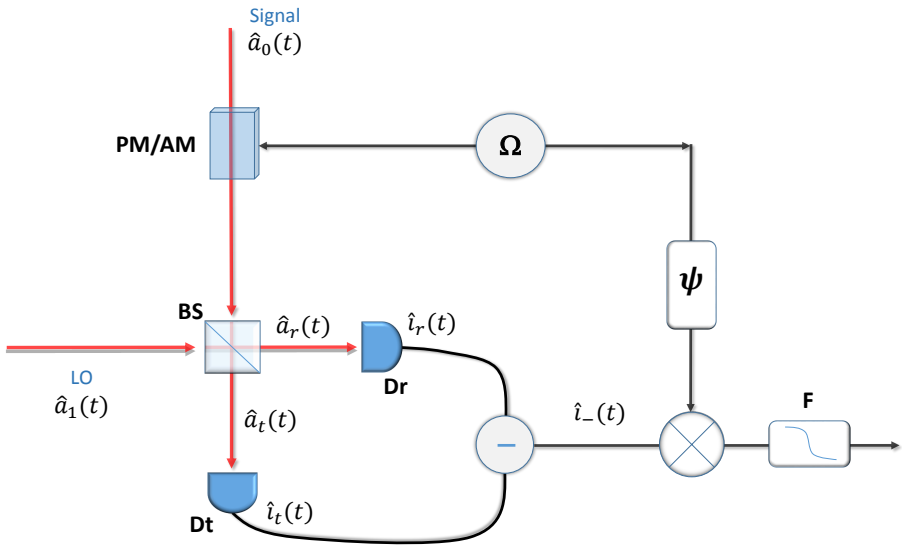

Figure 1.7: Schematic diagram of the Homodyne detection.

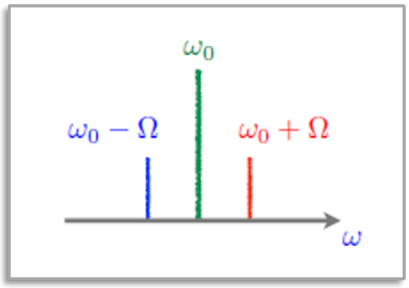

Figure 1.8: Sidebands.

whereas the component at frequency ω_0 as the *carrier* (see Fig. 1.8). By taking in consideration also the complex conjugate terms, Eq. 1.64 becomes:

$$a(t) = a_0(1-\delta)\left(e^{\imath\omega_0 t} + c.c.\right) + a_0\frac{\delta}{2}\left[e^{\imath(\omega_0+\Omega)t} + c.c + e^{\imath(\omega_0-\Omega)t} + c.c.\right] \tag{1.65}$$

Since the contribution at the carrier frequency ω_0 will be eliminated through the mixer ($\otimes$) and the low-pass filter (F) during the detection stage, we can focus only on the terms which depend on Ω. In order to write the quantum mechanical counterpart, it is useful to introduce the operator:

$$\tilde{a'}_0(t) = e^{\imath\omega_0 t}\frac{\tilde{a}_{+\Omega}(t)\,e^{-\imath\Omega t} + \tilde{a}_{-\Omega}(t)\,e^{\imath\Omega t}}{\sqrt{2}} = e^{\imath\omega_0 t}\tilde{a'}(t) \tag{1.66}$$

which formally corresponds to a linear mixing of the field operators of the two sidebands. Upon the substitution of this operator in Eq. 1.60, we now obtain:

$$\hat{\imath}_-(t) \propto 2\sqrt{RT}\,|\alpha|\left(\widetilde{a'}(t)\,e^{-\imath\theta} + \widetilde{a'}(t)^{\dagger}\,e^{+\imath\theta}\right) \tag{1.67}$$

namely, the signal that we want to measure is now around the frequency Ω. In order to bring the information around 0, we mix $\hat{i}_-$(t) with a signal at the frequency Ω and with phase Ψ by means of mixer (⊗). At the mixer output we have:

$$\hat{I}_{mix}(t) = \hat{i}_- \cos(\Omega t + \Psi) \propto \tilde{X}(t,\theta)\cos(\Omega t + \Psi) \tag{1.68}$$

With some algebra we obtain:

$$\hat{I}_{mix}(t) \propto \frac{1}{4}\left(\hat{X}_\Omega(t,\theta-\Psi) + \hat{X}_{-\Omega}(t,\theta+\Psi)\right) \tag{1.69}$$

where $\hat{X}_\Omega(t,\theta)$ and $\hat{X}_{-\Omega}(t,\theta)$ are the quadrature operators associated with the sidebands. We see that the result depends on Ψ. By setting Ψ=0 with a phase shifter we obtain the result that we wanted.

1.7 Quantum state tomography

We have seen that we can perform state reconstruction of the CV systems by quantum homodyne tomography, i.e., by collecting the outcome points x_k at different LO phases θ_k. In this section we show how we can obtain the expectation of an observable $\hat{O}$ given a state $\hat{\rho}$ and its homodyne data sample $\{(\theta_k, x_k)\}$ k = 1, . . . ,M. This technique is called the pattern function tomography [39, 40]. Upon exploiting the Glauber representation of operators in polar coordinates, the average value of a generic observable $\hat{O}$ may be rewritten as

$$\langle\hat{O}\rangle = \int_0^\pi \frac{d\theta}{\pi}\int_{-\infty}^{+\infty} dx\, p(x,\theta)\mathscr{R}[\hat{O}](x,\theta), \tag{1.70}$$

where $p(x,\theta) = \langle x_\theta|\hat{\rho}|x_\theta\rangle$ is the distribution of quadrature outcomes, with $\{|x_\theta\rangle\}$ the set of eigenvectors of $\hat{x}_\theta$, and $\mathscr{R}[\hat{O}](x,\theta) = \int_{-\infty}^{+\infty} dy|y|\mathrm{Tr}[\hat{O}e^{iy(\hat{x}_\theta - x)}]$ is the estimator of the operator ensemble average $\langle\hat{O}\rangle$. In the case of the homodyne data sample $\{(\theta_k, x_k)\}$ k = 1, . . . ,M. where θ_k uniformly spans the interval [0, π] and $M \gg 1$, the integral (1.70) can be rewritten as:

$$\langle\hat{O}\rangle = \lim_{M\to\infty}\frac{1}{M}\sum_{k=1}^{M}\mathscr{R}[\hat{O}](x_k,\theta_k). \tag{1.71}$$

Its discrete form is:

$$\langle\hat{O}\rangle = \frac{1}{M}\sum_{k=1}^{M}\mathscr{R}[\hat{O}](x_k,\theta_k). \tag{1.72}$$

gives an approximation of the actual value of $\langle\hat{O}\rangle$.

The uncertainty of the estimated value $\langle\hat{O}\rangle$ is ruled by the central limit theorem and scales as $\sqrt{M}$, namely

$$\delta\langle\hat{O}\rangle = \frac{1}{\sqrt{M}}\sqrt{\sum_{k=1}^{M}\frac{\left[\mathscr{R}[\hat{O}](x_k,\theta_k)\right]^2 - \langle\hat{O}\rangle^2}{M}}. \tag{1.73}$$

In order to properly characterize a single-mode prepared in a Gaussian state and measured with HD, we need to estimate the first two moments of the quadrature operator $\hat{X}(\phi)$ and reconstruct the first-moment vector and the CM, as well as the total energy

$\hat{a}^\dagger\hat{a}$ of the state. We thus need the following estimators [39]:

$$\mathscr{R}[\hat{X}(\phi)] = 2x\cos(\theta-\phi) \tag{1.74a}$$

$$\mathscr{R}[\hat{X}^2(\phi)] = (x^2-1)\Big\{1+2\cos[2(\theta-\phi)]\Big\}+1 \tag{1.74b}$$

$$\mathscr{R}[\hat{a}^\dagger\hat{a}] = \frac{1}{2}\left(x^2-1\right). \tag{1.74c}$$

In this way it is possible to compute the average value $\langle\hat{O}\rangle$ and the fluctuations $\langle\Delta\hat{O}^2\rangle \equiv \langle\hat{O}^2\rangle - \langle\hat{O}\rangle^2$ for the observables of interest, toghether with the corresponding uncertainties (1.73). This is the technique wich we will use to analyse the majority of experimental results exhibited in this thesis.

CHAPTER 2

Generation of nonclassical states

This chapter provides a brief introduction into the main nonlinear optical phenomena and discusses how it is possible to exploit them to generate nonclassical states.

2.1 Second-order optical nonlinearity

Nonlinear optics is the study of phenomena that are observed when the presence of light changes the optical properties of a material system. These phenomena are "nonlinear" in the sense that they occur when the response of a material system to an applied optical field depends in a nonlinear manner on the strength of the optical field. Although some classes of nonlinear optical effects were known long before the invention of the laser (for example, Pockels and Kerr electro-optic effects and light-induced resonant absorption saturation[41]), it was only with the advent of lasers that systematic studies of optical nonlinearities and the observation of a vast catalogue of nonlinear-optical phenomena became possible. An excellent treatment can be found in the nonlinear optics text by Boyd [42]. Here we will focus on the second-order nonlinearity which can be used to generate non-classical states of light or, more specifically, the squeezed states which constitute the main object of this thesis.

In order to describe more precisely what we mean by an optical nonlinearity, let us consider how the dipole moment per unit volume, or polarization $\widetilde{P}$ (t), which describe the optical response of a material system, depends on the strength $\widetilde{E}$ (t) of an applied optical field

$$\widetilde{P}(t) = \varepsilon_0 \left[\chi^{(1)} \widetilde{E}(t) + \chi^{(2)} \widetilde{E}^2(t) + \chi^{(3)} \widetilde{E}^3(t) + ... \right] \tag{2.1}$$

where ε_0 is the permittivity of free space and the quantities $\chi^{(1)}$ and $\chi^{(i)}$ are known as the linear and i^{th}-order non-linear optical susceptibilities, respectively. For the sake of simplicity, we have taken $\widetilde{P}$ (t) and $\widetilde{E}$ (t) like scalar quantities. In the case in which we also aim to take account of the vector nature of the fields, $\chi^{(1)}$ becomes a second-rank tensor, $\chi^{(2)}$ becomes a third-rank tensor, and so on[42]. For low electromagnetic field intensities, $\widetilde{P}$ (t) is purely linear. As the intensity increases the higher order terms in Eq. 2.1 become more significant and $\widetilde{P}$ (t) becomes increasingly nonlinear.

In particular, the second-order nonlinear optical processes (schematically illustrated in Fig. 2.1) are all those relying on the second-order nonlinear susceptibility $\chi^{(2)}$. They can be widely described as the nonlinear optical processes that involve the interaction of three photons, or in other words, as three-wave mixing processes. These processes can be divided into two complementary categories: the up-conversions, where two photons of lower energy combine to form a more energetic photon and the downconversions where a single photon is converted into two photons of lower energies. Upconversion

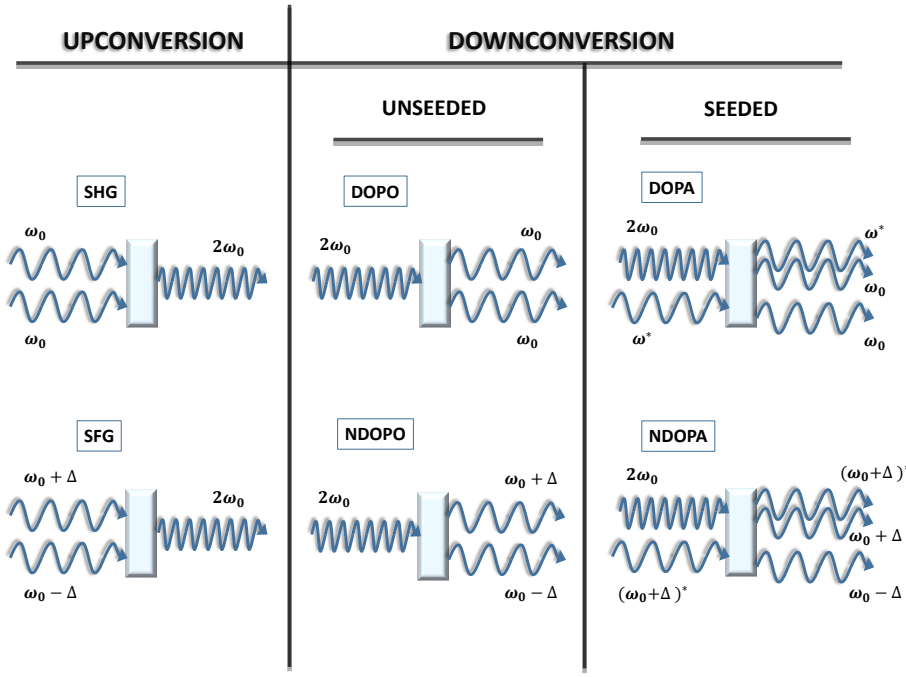

Figure 2.1: Overview of the basic $\chi^{(2)}$ nonlinear interactions. There are two groups of nonlinear effects which can be divided into upconversion and downconversion processes. The upconversion processes are second harmonic generation (SHG) and sum frequency generation, which is the non-degenerate case of SHG. The upconversion processes are degenerate optical parametric oscillation (DOPO) and amplification (DOPA) and the corresponding non degenerate processes NDOPO and NDOPA. The difference between OPO and OPA is that the OPA is seeded with fundamental field, whereas this seed is replaced with a vacuum field for the OPO. * denotes the seed photons.

processes include second harmonic generation (SHG) where two photons of frequency ω_0 are combined to form a photon of frequency $2\omega_0$. When the pair of incoming photons have different frequencies, $\omega_0 + \Delta$ and $\omega_0 - \Delta$, their combination is known as sum frequency generation (SFG). The downconversion processes are summarized on the right of Fig. 2.1. Unlike the upconversion processes, they have normally associated threshold powers below which the dissociation of a photon into the sub-harmonic photons does not occur. These processes are called degenerate and non-degenerate optical parametric oscillation (DOPO and NDOPO). By the introduction of a seed field (labelled with * in Fig. 2.1), the threshold condition can be lifted and we have the degenerate (DOPA) and non-degenerate optical parametric amplifications (NDOPA). We can also think of the DOPO and NDOPO as being vacuum seeded, that is to say it is the fluctuations of the vacuum field which trigger the dissociation of the photons.

2.1.1 Conservation laws

Conservation of energy

Like all physical processes, the conservation of energy must be satisfied during the $\chi^{(2)}$ interaction. For three photons with frequencies ω_1, ω_2 and ω_3, we thus require

$$\omega_1 + \omega_2 = \omega_3 \tag{2.2}$$

[1]

Conservation of momentum: Phase matching condition

The conservation of momentum in a nonlinear optical process is often referred to as the phase matching condition. Request that the momentum of the three photons is conserved means that their optical wavevectors $\mathbf{k}_i$ fulfill the following equation

$$\mathbf{k}_1 + \mathbf{k}_2 = \mathbf{k}_3 \tag{2.3}$$

where $|\mathbf{k}_i| = k_i = n_i\omega_i/c$, with n_i being the refractive index of the nonlinear medium experienced by the photon with frequency ω_i, and c the light speed in the vacuum. When this equation holds exactly, the system is said to be *phase matched*.

The simultaneous fulfilment of the energy conservation and the phase matching condition imposes a relationship on the refractive indices. Here we will restrict our attention to SHG or degenerate OPO where $\omega_1 = \omega_2 = \omega_0$, since the treatment of the non-degenerate processes is only a straight forward extension of the argument. In this case, the phase matching condition for the refractive indices is simply

$$n(\omega_0) = n(\omega_3) \tag{2.4}$$

It's worth noting that the phase-matching condition is seldom fulfilled because the refractive index of most dielectrics shows an effect known as normal dispersion: the refractive index is an increasing function of frequency. For this reason the most common procedure for achieving phase matching is to make use of the birefringence displayed by many crystals, i.e. the dependence of the refractive index on the direction of polarization of the optical radiation. In order to achieve phase matching through the use of birefringent crystals, the highest-frequency wave $\omega_3 = \omega_1 + \omega_2$ is polarized in the direction that gives it the lower of the two possible refractive indices or in other words it is polarised along the fast axis of the birefringent medium. Depending on the choice for the polarizations of the lower-frequency waves, it is referred to as:

- *type I phase matching* when the two lower-frequency waves have the same polarization orthogonal to that of the highest-frequency wave, e.g. they are both polarized along the slow axis of the birefringent medium, $\uparrow \omega_1 + \uparrow \omega_2 = \rightarrow \omega_3$. When the polarisation of one field is parallel to the optical axis (z), and the other field is free to propagate along any direction of the xy-plane the phase matching is said to be *non-critical*.

- *type II phase matching* when the two lower-frequency waves are orthogonally polarized to each other and the highest-frequency wave has the same polarization as one of the lower-frequency waves, e.g. $\uparrow \omega_1 + \rightarrow \omega_2 = \uparrow \omega_3$.

[1] This condition must be satisfied precisely for all nonlinear interactions.

In order to cancel the dispersion and to achieve the phase-matching condition $\Delta\mathbf{k} = \mathbf{k}_1 + \mathbf{k}_2 - \mathbf{k}_3 = 0$, two methods are used: angle tuning, which involves precise angular orientation of the crystal with respect to the propagation direction of the incident light[42] and temperature tuning changing the crystal temperature. For some crystals, indeed, the amount of birefringence is strongly temperature-dependent. As a result, it is possible to phase-match the mixing process by holding the crystal orientation with respect to the propagation direction of the incident light and varying the crystal temperature. The nonlinear medium used throughout the experiments presented in this thesis in order to generate the non classical states is Magnesium Oxide doped Lithium Niobate (MgO:LiNbO3) which deals with this latter case: its refractive index is strongly depend on temperature and temperature tuning is used to achieve noncritical phase matching as we will show in Chap. 3.

- *Quasi-phase matching* In a quasi-phase matched material, the phase matching is obtained via a periodic manipulation of the cumulated relative optical phase. By the short periodic inversion of the crystal domain, the phase mismatch is governed by

$$\Delta\mathbf{k} = (\mathbf{k}_1 + \mathbf{k}_2) - \mathbf{k}_3 - \frac{2\pi}{\Lambda} \tag{2.5}$$

  where Λ is the crystal inversion period. Hence, the condition imposed on the refractive indices is no longer required due to an additional periodic poling term. The advantage of periodic poling is that it can provide a means to access dielectric polarization with high nonlinearity which are otherwise unreachable with angle and temperature tuning. An example of quasi-phase matching is the use of periodically poled lithium niobate (PPLN) at Nd:YAG wavelength for the purpose of frequency doubling. In this situation, the polarization of all three modes are the same, e.g. $\uparrow \omega_1 + \uparrow \omega_2 = \uparrow \omega_3$

2.2 Optical parametric oscillation

Among $\chi^{(2)}$ processes, we want to focus on the *parametric down conversion*, which is our basis for squeezed states generation. A strong beam E_p at frequency ω_p and a weak beam E_s at frequency ω_s (*seed*) are injected into the non linear crystal. Due to non-linear effect, the two fields "mix" inside the crystal and a macroscopic wave at frequency $\omega_i = \omega_p - \omega_s$ is generated by the induced $\widetilde{P}^{(2)}$ polarization:

$$\widetilde{P}^{(2)}(\omega_p - \omega_s) = 2\chi^{(2)} E_p E_s^*. \tag{2.6}$$

The applied field E_p is called pump beam, the generated beams respectively signal (E_s) and idler (E_i). From the quantum point of view, the entire process can be depicted according to the photon energy-level description. Due to absorption of a photon at frequency ω_p an atomic virtual level is excited. This level decays by a two photon emission process that is stimulated by the presence of ω_s field. Two photon spontaneous emission occurs even if the ω_s-field is not applied. In this case the pump energy is spread over more signal/idler pairs so that the generated fields are very much weaker. In fact, we can see that the amount of squeezing obtained by a single pass of a continuous-wave pump laser through a nonlinear crystal of a reasonable size is very small. Two methods are commonly used to address this complication. First, one could use an ultrashort pulsed laser, thereby greatly increasing the pump amplitude [43][44][45]. The second approach is to place the crystal inside an optical resonator (see Fig. 2.3). This enables

the enhancing of the down conversion process in order to obtain macroscopical signal and idler beams even without any initial seed. In fact when a nonlinear medium inside an optical cavity is irradiated with a pump beam, the signal generated on the first pass trough the medium can act as an input on consecutive passes, if it is coupled into the cavity. The signal builds up within the cavity if its wavelength corresponds to high reflectivity of the cavity mirrors and it fulfils the resonance condition of the cavity. The cavity can be resonant to the pump light, thereby enhancing the effective pump power, or to the signal, effectively allowing multiple passing of the signal through the crystal, or both. In our case the cavity is resonant to the signal. This configuration is referred to as the optical parametric oscillator (OPO).

2.3 The quantum behaviour of the Optical Parametric Oscillator (OPO)

Here we want to study the Optical Parametric Oscillator (OPO) in order to retrieve its quantum equations of motion.

2.3.1 Classical description of a linear cavity

We start from a classical description for the linear cavity modelled in fig. 2.2 in order to retrieve the equations of motion of a single cavity mode. It has two partially transmitting

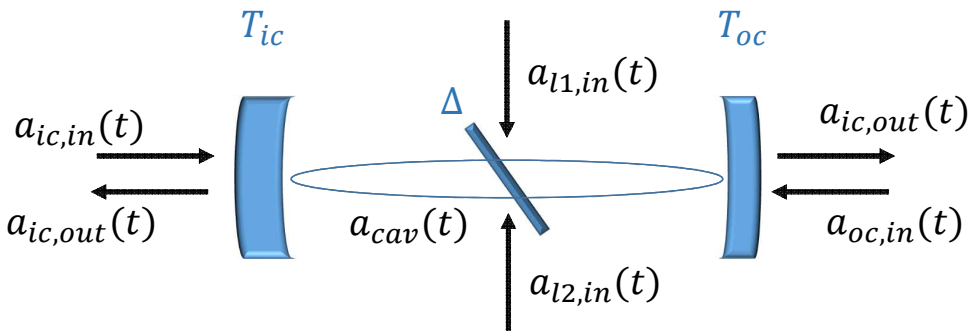

Figure 2.2: A model of passive optical resonator, including input fields from the input and output couplers, input field fluctuations due to loss in the resonator, and output fields exiting the input and output couplers.

mirrors, input (ic) and output (oc) coupler, with transmissivity T_{ic} and T_{oc}, respectively. The internal loss can be schematized as a beam splitter with reflectivity Δ and the input field fluctuations due to this loss are referred to with $a_{l1,in}$(t) and $a_{l2,in}$(t). External fields, $a_{ic,in}$(t) and $a_{oc,in}$(t) enter at the ic and oc coupler respectively. We can calculate the change in the complex field amplitude $a_{cav}(t)$ after one round-trip when the laser carrier frequency is perfectly resonant, under the assumption that this change is small [13]. The classical equation of motion, that will be retrieved in this way, will be the starting point for our quantum description.

If we follow the field a_{cav}(t) in a round trip we have:

$$\begin{aligned} a_{cav}(t+\tau) =& a_{cav}(t)\sqrt{1-T_{ic}}\sqrt{1-T_{oc}}\sqrt{1-\Delta}+a_{ic,in}\sqrt{T_{ic}}+a_{oc,in}\sqrt{T_{oc}}\sqrt{1-T_{ic}}\sqrt{1-\Delta}+ \\ & a_{l1}\sqrt{\Delta}\sqrt{1-T_{oc}}\sqrt{1-T_{ic}}\sqrt{1-\Delta}+a_{l2}\sqrt{\Delta}\sqrt{1-T_{ic}} \end{aligned} \tag{2.7}$$

where τ is the cavity round-trip time. If the change in the field in one round trip is small, we can write

$$a_{cav}(t+\tau) \approx a_{cav}(t)+\dot{a}_{cav}(t)\,\tau \tag{2.8}$$

If the cavity is at resonance and $T_{oc}, T_{ic}, \Delta \ll 1$, the 2.7 can be approximated by

$$\sqrt{\tau}\dot{a}_{cav}(t) \approx \sqrt{\tau}a_{cav}(t)\left(\frac{T_{ic}}{2\tau}+\frac{T_{oc}}{2\tau}+\frac{2\Delta}{2\tau}\right)+a_{ic,in}\frac{\sqrt{T_{ic}}}{\tau}+a_{oc,in}\frac{\sqrt{T_{oc}}}{\tau}+a_{l1}\frac{\sqrt{\Delta}}{\tau}+a_{l2}\frac{\sqrt{\Delta}}{\tau} \tag{2.9}$$

Now, we can define the decay rate of the cavity as

$$\gamma_{ic}=\frac{T_{ic}}{2\tau};\quad \gamma_{oc}=\frac{T_{oc}}{2\tau};\quad \gamma_{l}=\frac{2\Delta}{2\tau}; \tag{2.10a}$$

$$\gamma=\gamma_{ic}+\gamma_{oc}+2\gamma_{l} \tag{2.10b}$$

and the complex amplitude $a(t)$ of the standing mode of the cavity as

$$a(t)=\sqrt{\tau}a_{cav}(t) \tag{2.11}$$

. Thus, Eq. 2.9 becomes

$$\dot{a}(t) \approx -\gamma a(t)+\sqrt{2\gamma_{ic}}a_{ic,in}+\sqrt{2\gamma_{oc}}a_{oc,in}+\sqrt{2\gamma_{l1}}a_{l1}+\sqrt{2\gamma_{l2}}a_{l2} \tag{2.12}$$

If the fields acquire a phase shift ϕ in a round trip, or, in other words the mode isn't on cavity resonance we have:

$$a(t+\tau)=a(t)+\dot{a}\tau=a(t)\,e^{\imath\phi} \approx a(t)\,(1+\imath\phi) \tag{2.13}$$

i.e.

$$\dot{a}(t) \approx \imath\frac{\phi}{\tau}a(t)=\imath\Omega a(t) \tag{2.14}$$

where Ω is the frequency shift respect to the resonance. Therefore we can write:

$$\dot{a}(t) \approx -(\gamma-\imath\Omega)\,a(t)+\sqrt{2\gamma_{ic}}a_{ic,in}+\sqrt{2\gamma_{oc}}a_{oc,in}+\sqrt{2\gamma_{l1}}a_{l1}+\sqrt{2\gamma_{l2}}a_{l2} \tag{2.15}$$

Besides if we want to link the output fields to the input fields, we have to consider the boundary conditions which can be written as [13]:

$$\begin{aligned} a_{ic,in} &= -a_{ic,in}+\sqrt{2\gamma_{ic}}a \\ a_{oc,out} &= -a_{oc,in}+\sqrt{2\gamma_{oc}}a \end{aligned} \tag{2.16}$$

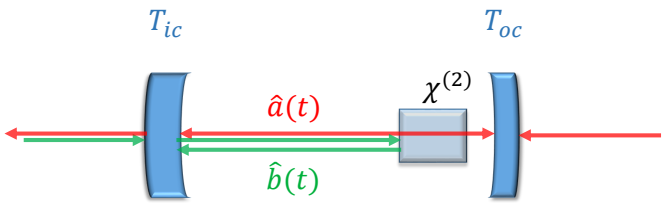

Figure 2.3: OPO cavity layout.

2.3.2 Non-linear interaction

We now include in our system the crystal characterized by $\chi^{(2)}$ (see Fig. 2.3). In this case, in order to obtain the equations of motion for the internal cavity modes we have to consider the interaction between the field inside the cavity and the crystal. If we work in the interaction picture, the Hamiltonian describing such interaction is

$$\hat{H} = \frac{\imath\hbar\chi^{(2)}}{2}\left(\hat{b}^{\dagger}\hat{a}^{2} - \hat{a}^{\dagger 2}\hat{b}\right) \tag{2.17}$$

where $\hat{a}$ and $\hat{b}$ are the modes of the fundamental and the harmonic field (the pump), respectively.

In the Heisenberg picture, the equation of motion for an arbitrary operator $\hat{O}$, reads as

$$\frac{d\hat{O}}{dt} = \frac{\imath}{\hbar}\left[\hat{H},\hat{O}\right] \tag{2.18}$$

Therefore we have

$$\frac{d\hat{a}}{dt} = -\chi^{(2)}\hat{b}\hat{a}^{\dagger} \tag{2.19a}$$

$$\frac{d\hat{b}}{dt} = \frac{\chi^{(2)}}{2}\hat{a}^{2} \tag{2.19b}$$

We now assume that the harmonic field is an intense field which is virtually undepleted by its interaction with the non-linear crystal. Under these conditions we can replace the operator $\hat{b}$ with the c-number b. Let us redefine the quadrature operator 1.35 so that the vacuum variance is equal to one:

$$\hat{X}_1 = \frac{1}{\sqrt{2}}\left(\hat{a}+\hat{a}^{\dagger}\right) \tag{2.20a}$$

$$\hat{X}_2 = \frac{1}{\sqrt{2}\imath}\left(\hat{a}-\hat{a}^{\dagger}\right) \tag{2.20b}$$

In terms of them we obtain

$$\frac{d\hat{X}_{1,2}}{dt} = \mp\tilde{\chi}\hat{X}_{1,2} \tag{2.21}$$

where we have put $\tilde{\chi} = \frac{\chi^{(2)}}{\sqrt{\tau}} b$. Therefore by considering only the non linear interaction the solutions are:

$$\hat{X}_1^{out} = e^{-\tilde{\chi} t} \hat{X}_1^{in} \tag{2.22a}$$

$$\hat{X}_2^{out} = e^{+\tilde{\chi} t} \hat{X}_2^{in} \tag{2.22b}$$

and since the vacuum variance is one the quadrature variances are

$$\left\langle \Delta X_1^{out2} \right\rangle = e^{-2\tilde{\chi} t} \tag{2.23a}$$

$$\left\langle \Delta X_2^{out2} \right\rangle = e^{+2\tilde{\chi} t} \tag{2.23b}$$

We see that the crystal effect is to transfer noise from $\hat{X}_1$ to $\hat{X}_2$.

2.3.3 The quantum equations of motion for the OPO

In general, in order to describe the quantum behaviour of the OPO, we need to write the Hamiltonian describing the interactions within the cavity as well as those between the cavity mode and the continuum of field modes outside the cavity [13]. However, to switch to the quantum description, here we use the simpler approach of canonical quantization of the classical equation 2.15. With the substitution a(t)$\rightarrow \hat{a}$(t) and by considering the Eq. 2.19 we obtain

$$\dot{\hat{a}}(t) = -(\gamma - \imath\Omega)\hat{a}(t) - \chi \hat{b}\hat{a}^{\dagger} + \sqrt{2\gamma_{ic}}\hat{a}_{ic,in} + \sqrt{2\gamma_{oc}}\hat{a}_{oc,in} + \sqrt{2\gamma_l}\hat{a}_{l1} + \sqrt{2\gamma_l}\hat{a}_{l2} \tag{2.24a}$$

$$\dot{\hat{b}}(t) = -(\gamma_2 - \imath\Omega_2)\hat{b}(t) - \frac{\chi}{2}\hat{a}^2 + \sqrt{2\gamma_{2ic}}\hat{b}_{ic,in} + \sqrt{2\gamma_{2oc}}\hat{b}_{oc,in} + \sqrt{2\gamma_{2l}}\hat{b}_{l1} + \sqrt{2\gamma_{2l}}\hat{b}_{l2} \tag{2.24b}$$

where we term the decay rate relating to the second harmonic field $\hat{b}$ with subscript ″2″. Also the boundary condition can be obtained directly from the classical boundary conditions in the same way.

2.4 Calculation of squeezing from an OPO cavity

We start from our cavity equation for the parametric amplifier with Ω=0

$$\dot{\hat{a}}(t) = -\gamma\hat{a}(t) - \chi b\hat{a}^{\dagger} + \sqrt{2\gamma_{ic}}\hat{a}_{ic,in} + \sqrt{2\gamma_{oc}}\hat{a}_{oc,in} + \sqrt{2\gamma_l}\hat{a}_{l1} + \sqrt{2\gamma_l}\hat{a}_{l2} \tag{2.25}$$

By observing only the output field we can use the boundary condition

$$\hat{a}_{oc,out} = -\hat{a}_{oc,in} + \sqrt{2\gamma_{oc}}\hat{a} \tag{2.26}$$

and the steady-state solution is obtained by setting the time derivative to zero. Therefore we have:

$$\begin{aligned} a_{oc,out} = &-\frac{\tilde{\chi}}{\gamma}\left(a_{oc,out}^{\dagger} + a_{oc,in}^{\dagger}\right) + \\ &\frac{1}{\gamma}\left[(\gamma_{oc} - \gamma_{ic} - 2\gamma_l)\,a_{oc,in} + \sqrt{4\gamma_{oc}\gamma_{ic}}a_{ic,out} + \sqrt{4\gamma_{oc}\gamma_l}a_{l1} + \sqrt{4\gamma_{oc}\gamma_l}a_{l2}\right] \end{aligned} \tag{2.27}$$

From this equation we can obtain the expressions for the quadrature operators $\hat{X}_{1(oc,out)}$ and $\hat{X}_{2(oc,out)}$:

$$\hat{X}_{1(oc,out)} = \frac{\gamma_{oc} - \gamma_{ic} - 2\gamma_l - \tilde{\chi}\hat{X}_{1(oc,in)} + \sqrt{4\gamma_{oc}\gamma_{ic}}\hat{X}_{1(oc,in)} + \sqrt{4\gamma_{oc}\gamma_l}\hat{X}_{1(l1)} + \sqrt{4\gamma_{oc}\gamma_l}\hat{X}_{1(l2)}}{\gamma + \tilde{\chi}}$$
$$\hat{X}_{2(oc,out)} = \frac{\gamma_{oc} - \gamma_{ic} - 2\gamma_l + \tilde{\chi}\hat{X}_{1(oc,in)} + \sqrt{4\gamma_{oc}\gamma_{ic}}\hat{X}_{1(oc,in)} + \sqrt{4\gamma_{oc}\gamma_l}\hat{X}_{1(l1)} + \sqrt{4\gamma_{oc}\gamma_l}\hat{X}_{1(l2)}}{\gamma - \tilde{\chi}} \tag{2.28}$$

The condition $\gamma_{oc} = \tilde{\chi}$ defines the threshold of the OPO and $\tilde{\chi} \propto \sqrt{P}$ where P is the pump power. We put

$$d = \frac{\tilde{\chi}}{\gamma_{oc}} = \sqrt{\frac{P}{P_{th}}} \tag{2.29}$$

where P_{th} is the pump power and the OPO threshold power.

In order to understand the process of squeezing via optical parametric amplification let us assume that all of the input fields are in coherent or vacuum states. The quadrature variances of the output field are then given by the simplified expression

$$\langle \Delta X^2_{1,2} \rangle = 1 \mp \eta_{esc} \frac{4d}{(1 \pm d)^2} \tag{2.30}$$

where $\eta_{esc} = \gamma_{oc}/\gamma$ is the escape efficiency of the cavity.

If we have $\Omega \neq 0$, the quadrature variances of the output field become:

$$\langle \Delta X^2_{1,2} \rangle = 1 \mp \eta_{esc} \frac{4d}{(\Omega/\gamma)^2 + (1 \pm d)^2} \tag{2.31}$$

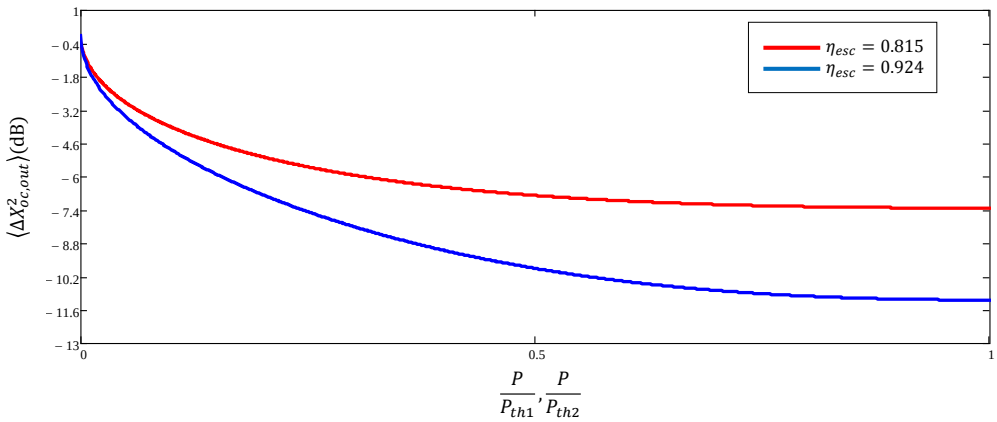

Figure 2.4: Squeezing from an optical parametric oscillator as a function of pump power normalized to the threshold power when Ω=0. The plots show the predicted amplitude (phase) quadrature variance of the output field for two values of the escape efficiency of OPO cavity. Pump depletion is neglected, and all the input fields are assumed to be in coherent or vacuum states. The calculation was performed with the experimental parameters derived in Chap. 3

In the deamplifcation regime the second harmonic pump field is π out of phase with the fundamental seed, so that the coherent amplitude of the pump field is real and nega-

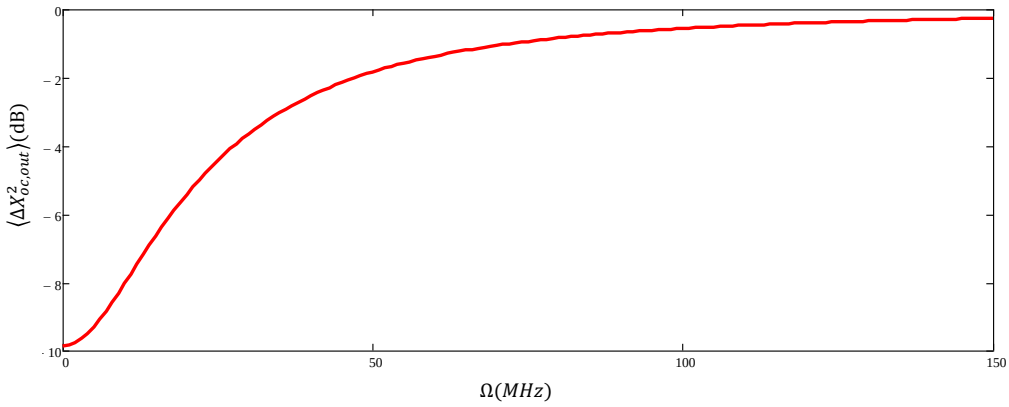

Figure 2.5: The predicted frequency spectra of the squeezing at half threshold for an OPO operating in the deamplification regime, with $\eta_{esc} = 0.914$.

tive. We see that in this regime the amplitude quadrature of the output field is squeezed for all non-zero pump powers and all sideband frequencies.

At Ω=0, and at threshold, the level of squeezing is ultimately limited by the escape efficiency $\rightarrow 1 - \eta_{esc}$ and the optimum squeezing is achieved. In the amplification regime (the coherent amplitude real and positive) the squeezing is observed on the phase quadrature of the output field, and the amplitude quadrature is anti-squeezed. Also in this case it is observed the squeezing improving at low frequencies and near threshold. Fig. 2.4 shows the predicted squeezed quadrature variance as a function of pump power for two different η_{esc} values: $\eta_{esc} = 0.815$ and $\eta_{esc} = 0.914$. These are the two cases realized in our laboratory as we will see in more detail in Chap. 3.

In practice, due to low frequency noise sources, we do not observe squeezing at ω=0, as we have already explain in Sec. 1.6. The predicted frequency spectra of the squeezing at half threshold is shown in Fig. 2.5 for an OPO operating in the deamplification regime, with $\eta_{esc} = 0.914$. As Ω increases the level of squeezing drops with $\langle \Delta X^2_{oc,out} \rangle \rightarrow 1$ as $\Omega \rightarrow \infty$. In our experiment $\Omega/2\pi$=3 MHz where we expect to observe a reasonable level of squeezing.

2.5 Classical properties of parametric amplification.

Let us now examine the classical property of parametric amplification by considering the Eq. 2.24a in the classical case, i.e. a e b are c-numbers [13]. The steady-state solution is obtained by setting the time derivative to zero

$$0 = -\gamma a - \tilde{\chi} a^* + \sqrt{2\gamma_{ic}} a_{ic,in} \tag{2.32}$$

where we have set only $a_{ic,in} \neq 0$ because in our experiment, we seeded our OPO through ic. Besides we consider $a_{ic,in} \in \Re$. The complex conjugate equation of Eq. 2.32 reads as

$$0 = -\gamma a^* - \tilde{\chi}^* a + \sqrt{2\gamma_{ic}} a_{ic,in} \tag{2.33}$$

where we have take into account of the pump field phase in $\tilde{\chi}$. By replacing the Eq. 2.33 in Eq. 2.32 we obtain

$$\left(1-\frac{|\widetilde{\chi}|^2}{\gamma^2}\right)a=\frac{\sqrt{2\gamma_{ic}}}{\gamma}\left(1-\frac{\widetilde{\chi}}{\gamma}\right)a_{ic,in} \tag{2.34}$$

Finally, by considering the boundary condition for the output mirror and by putting the input of this mirror equal to zero:

$$a_{oc,out}=\frac{\sqrt{4\gamma_{ic}\gamma_{oc}}}{\gamma}\frac{1}{\left(1\pm\frac{|\widetilde{\chi}|}{\gamma}\right)}a_{ic,in} \tag{2.35}$$

and the regenerative gain G=$\left|\frac{a_{oc,out}}{a_{ic,in}}\right|^2$ is

$$G_{\pm}=\frac{1}{(1\pm d)^2} \tag{2.36}$$

2.6 Losses effect on squeezing

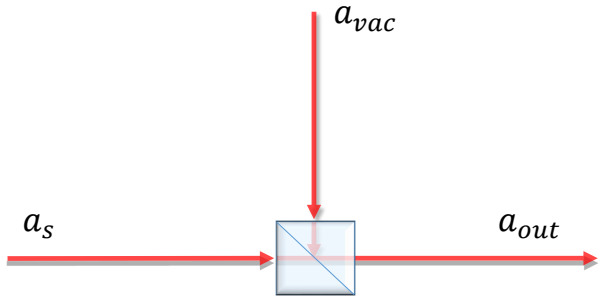

Figure 2.6: The beam splitter model of losses.

Squeezed states that are observed in practical experiments necessarily suffer from losses present in transmission channels and detectors which degrade the observed squeezing and anti-squeezing levels. In order to understand the effect of losses on a single-mode squeezed state, we can use the model in which a lossy optical element with a certain power reflectivity ε (i.e. with an efficiency $\eta=1-\varepsilon$) is replaced by a beam splitter . At the other input port of the beam splitter there is the vacuum state (see fig.2.6).

The interference of the signal mode a_s with the vacuum mode a_{vac} will produce a outgoing mode a_{out}

$$a_{out}=\sqrt{\eta}a_s+\imath\sqrt{1-\eta}a_{vac} \tag{2.37}$$

Accordingly, we have

$$\hat{X}_{out}(\theta)=\sqrt{\eta}\hat{X}_s(\theta)+\sqrt{1-\eta}\hat{X}_{vac}(\theta) \tag{2.38}$$

Because signal and vacuum states are uncorrelated to each other, it follows that:

$$\left\langle\Delta X_{out}^2\right\rangle=\eta\left\langle\Delta X_s^2\right\rangle+(1-\eta)\left\langle\Delta X_{vac}^2\right\rangle \tag{2.39}$$

Therefore, since the vacuum variance is one, we can rewrite the Eq. 2.31 as

$$\left\langle \Delta X_{1,2}^2 \right\rangle = 1 \mp \eta\, \eta_{esc} \frac{4d}{(\Omega/\gamma)^2 + (1 \pm d)^2} \tag{2.40}$$

CHAPTER 3

The experimental setup

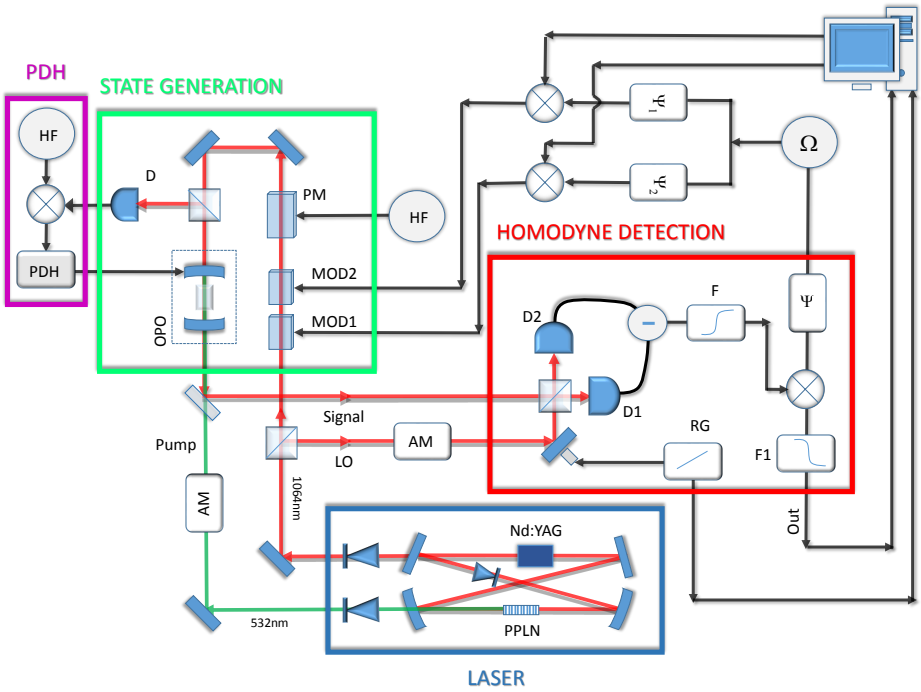

Figure 3.1: Experimental setup for generation and detection of squeezed state. It consists of four stages, laser, state generation, PDH and homodyne detection stages. The principal radiation source is provided by a homemade single-mode Nd:YAGlaser internally frequency doubled by a periodically poled MgO:$LiNbO_3$. The laser output at 532 nm is used as the pump for an optical parametric oscillator (OPO), whereas the other output at 1064 nm is sent to a polarising beam splitter (PBS) to generate the input for the state generation stage and the local oscillator (LO) for the homodyne detector. The sidebands used as OPO coherent seeds are generated by exploiting the combined effect of the two optical systems, MOD1 and MOD2. A phase modulator (PM) generates the sidebands used as active stabilization of the OPO cavity via the Pound-Drever-Hall (PDH) technique. The homodyne detector consists of a balanced beam splitter, two low noise detectors (D1 and D2), and a differential amplifier. The powers of the LO and of the pump are set by amplitude modulators (AM) that consist of an half-wave plate and a Brewster plate.

In this Chapter we discuss in detail the experimental system that enabled generation and detection of the states analysed throughout the work presented in this thesis. It has been implemented during my Ph.D in order to study several features of non-classical states of light. In particular, the published or submitted papers in which it has been exploited will be shown in the Part II of this thesis.

3.1 Introduction

The experimental setup used for the generation and detection of non-classical states in the continuous variables regime consists of four stages, as highlighted in Fig.3.1: laser, state generation, PDH and homodyne detection stages. A brief description of these stages is provided below. Then they will be analysed individually in the subsequent sections in more detail.

The principal radiation source is provided by a homemade Nd:YAG laser internally frequency doubled by a periodically poled MgO:$LiNbO_3$ (PPLN in Fig. 3.1). The laser output at 532 nm is used as the pump for an optical parametric oscillator (OPO), whereas the other output at 1064 nm is sent to a polarising beam splitter (PBS) to generate the input for the state generation stage and the local oscillator (LO) for the homodyne detector. The pump and LO powers are set by two amplitude modulators (AM) which consists in a half-wave plate and a Brewster plate. The core component of the state generation stage is the OPO, which consist in an linear cavity in which a MgO:$LiNbO_3$ crystal is placed. The OPO generates the squeezed light by means of the non linear effect, whose corresponding theories and experimental realizations have already been reported in Chap. 2. The sidebands (at frequency $\Omega/2\pi$ = 3 MHz) used as OPO coherent seeds are generated by exploiting the combined effect of the two optical systems, indicated in Fig. 3.1 as MOD1 and MOD2, whereas a phase modulator (PM) generates the sidebands used as active stabilization of the OPO cavity via the Pound-Drever-Hall (PDH) technique. The homodyne detector consists of a balanced beam splitter, two low noise detectors ($D1$ and $D2$), and a differential amplifier ($\ominus$). To remove the low frequency signal we use an high-pass filter @ 500kHz and then the signal is sent to the demodulation apparatus. To extract the information about the signal (that is at frequency $\Omega/2\pi$) we use a phase shifter (Ψ) a mixer ($\otimes$) and a low pass filter @ 300kHz.

3.2 The laser

The radiation source is a single-mode home-made Nd:YAG laser producing radiation at 1064 nm. It consists of a 4 mirrors ring cavity, as sketched in Fig. 3.2. The active medium is a cylindrical Nd:YAG crystal with a diameter of 2 mm and 60 mm length radially pumped by three arrays of laser diode at a wavelength of 808 nm, water cooled. The two curved mirrors (M3 and M2), with high reflectivity at 1064 nm, have radius of curvature r_{oc}=300 mm, the mirror M4 has maximum reflectivity at an angle of incidence of 10° and the output coupler for the wavelength at 1064 nm (M1) has 97.5 % reflectivity.

There are several methods of forcing a laser to oscillate in a single transverse and/or longitudinal mode. In our case in order to achieve the single transverse mode selection, the cavity is designed such that only TEM_{00} mode is selected whereas the other higher order modes are cute off by the active medium. Hence, the beam waist inside the Nd:YAG crystal is w_{AM}=0.52 mm÷0.55 mm (see Fig. 3.3). For laser bandwidths much larger than the Free Spectral Range (FSR) [1], the most efficient method of achieving single

[1] The resonance frequencies of a cavity satisfy the condition $\nu = n\frac{c}{2L}$ with n integer, c being the light speed

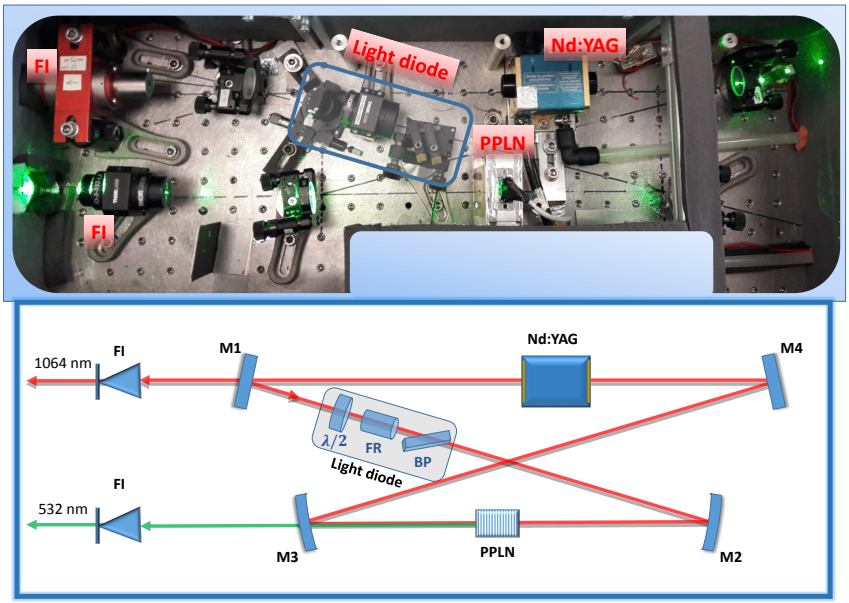

Figure 3.2: Schematic diagram of the laser compared with its photo. The active medium is a cylindrical Nd:YAG crystal and a periodically poled MgO:LiNbO3 (PPLN) is used for the second harmonic generation. The single mode operation is ensured by a light diode which consists of a half-wave plate ($\lambda/2$), a Faraday rotator (FR) and a Brewster plate (BP).

longitudinal mode selection is to force the oscillation to be unidirectional. In this case, in fact, the phenomenon of spatial hole burning [2] within the active medium does not occur and the laser tends to oscillate on a single mode [46]. To achieve unidirectional ring operation, an *optical diode* is inserted within the laser cavity. It is a device giving preferential transmission of one direction of beam propagation and consist of a half-wave plate ($\lambda/2$), a Faraday rotator (FR), and a Brewster plate (BP) which is a plate of an optical material with coplanar surfaces, inserted into the laser beam at Brewster's angle so that the reflection loss becomes minimal for *p*-polarized light. Our FR consists of a Terbium

and L the optical length of the cavity. The resonance frequencies are equally spaced and the difference between two adjacent resonance frequencies is called *free spectral range* (FSR) [13] [46]

$$FSR = \frac{c}{2L}$$

.

[2] Lasers with both homogeneously and inhomogeneously broadened gain media tend to oscillate in several longitudinal modes as result of *spatial* and *spectral hole burning*, respectively [46]. For homogeneous line, multimode oscillation is due to holes burned in the spatial distribution of inversion within the active medium. This phenomenon is known as *spatial hole burning*. More specifically, in standing-wave laser cavities, the coherent superposition of the optical fields travelling in opposite directions within the cavity results in a sinusoidal intensity distribution. At the maxima of the intensity distribution, there is strong gain saturation, and the population inversion is depleted. However, at nulls in the optical field, the oscillating mode is unable to deplete the inversion. As the result, the inversion density is no longer uniform, but has "holes" at the positions corresponding to the peaks in the optical intensity. The gain at the nulls in the optical field will continue to increase as the gain medium is pumped harder. Because other cavity modes have a different spatial profile than the first mode and can use the population inversion at these positions, this can lead to multimode operation.

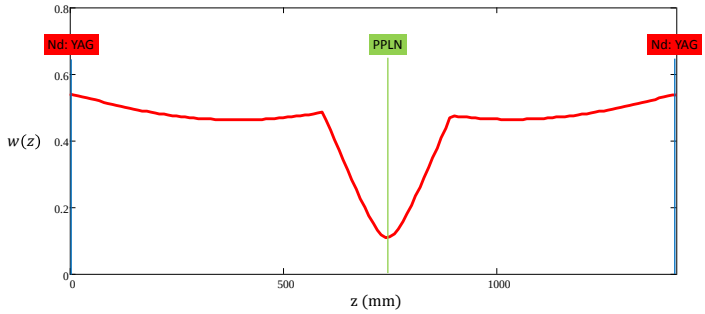

Figure 3.3: Profile of w(z) inside the laser cavity during a round trip starting from the Nd:YAG crystal. The crystal for the second-harmonic generation (PPLN) is in the center.

Gallium Garnet (TGG) crystal immersed in a longitudinal dc magnetic field, H. When a linearly polarized optical beam passes through the Faraday rotator, its polarization plane experiences a rotation about the beam axis:

$$\theta_{FR} = VdH \tag{3.1}$$

where d is the crystal length and V is the Verdet constant (V=40 rad/Tm @1064nm) [47]. The sense of rotation depends on the relative direction of the magnetic field and the beam propagation direction: counterclockwise for a left-to-right propagating beam and clockwise for a right-to-left propagating beam.

The p polarized wave travelling from left to right passes first through a $\lambda/2$ plate that rotates the polarization vector of θ=15°. Then it passes through the Faraday rotator, with its axis in the magnetic field direction. The output beam has the plane of polarization rotated about the beam axis of θ_{FR}=-15°. Therefore the two rotations exactly cancel, so no attenuation is suffered by the beam passing through the BP. For a beam travelling in the opposite direction, right to left, the two rotation add to each other (i.e. θ_{tot}= 30°). Correspondingly, the beam experiences losses larger than the laser gain.

The second-harmonic generation (SHG) occurs within the laser cavity by using a periodically poled MgO:LiNbO3 (PPLN) thermally stabilized around 70 °C. The intracavity frequency doubling prevents the mode hopping [48]. This is the phenomenon in which a laser exhibits sudden jumps between different modes: the laser may operate on a single resonator mode for some time, but then suddenly switches to another mode. This means that this other mode suddenly takes over or that there may be power in both modes. The intracavity SHG, introduces a loss that is less for the oscillating mode than for the neighboring modes. At first sight this seems counterintuitive, since it is the lasing mode that obviously has a significant loss, namely that resulting from the generation of its second harmonic, whereas adjacent, nonlasing modes would have negligible loss due to SHG. However, these modes are subject to loss from the generation of their sum frequency. The effect turns out to be twice the loss that the lasing mode experiences through SHG. Mode hopping is thereby suppressed, as the lasing mode dominates the neighboring modes. The cavity is designed so that the waist in SHG cristal is w_{SHG}=0.11÷0.12 mm (see Fig.3.3) in order to obtain a good conversion efficiency however remaining below the damage threshold (500kW/cm^2). The laser output powers for 1064 nm and 532 nm vs the pump current are shown in Fig. 3.4. By considering that the output coupler (M1)

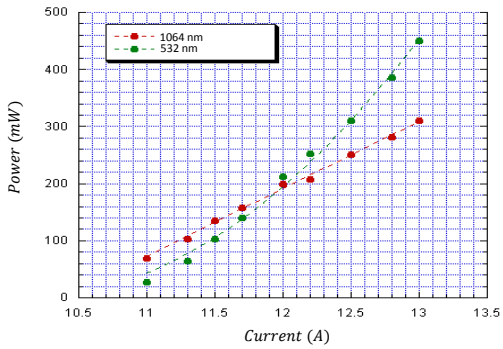

Figure 3.4: Laser output power vs pump current: @1064 nm (red) @532 nm (green).

reflectivity at 1064 nm and that the losses experienced by the output at 532 nm output (M3) are 35%, we have a conversion efficiency about 5.8 % at a current value of 13 A.

The FSR is 203 MHz and the relaxation oscillation frequency at the current at which we operate ($\sim$ 13 A) is about 90 kHz thus allowing a noise spectrum shifted towards the low frequencies.

3.3 States generation stage

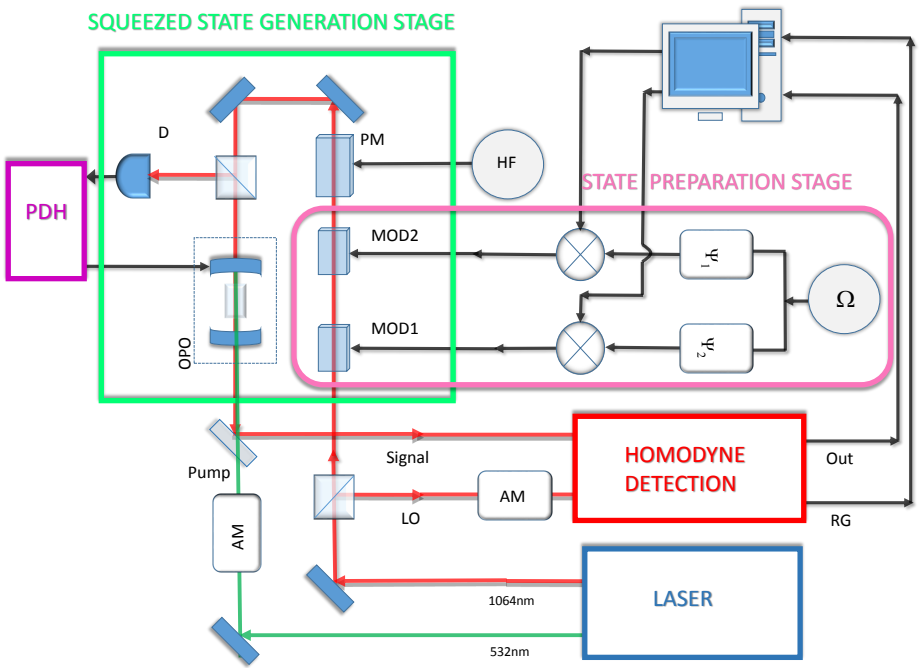

Figure 3.5: Zoom on states generation stage.

The non classical states generation process is performed in two steps, labelled as *state preparation stage* and *squeezed state generation stage* in Fig. 3.5, respectively. First, the sidebands used as OPO seeds are generated at frequency $\Omega/2\pi$= 3 MHz by exploiting the combined effect of the two optical systems, indicated in Fig. 3.5 as MOD1 and MOD2. Then, the resultant state is sent into the OPO cavity, in which it is squeezed as shown in Chap. 2.

3.3.1 State preparation stage

Our aim is to generate an arbitrary state, with amplitude and phase selectable on demand. In a first step, we have to generate an arbitrary coherent state (CS) which we can model as a cosine function:

$$CS = A\cos(\omega t + \varphi) \tag{3.2}$$

with adjustable values of the amplitude A and phase φ. The idea underlying our strategy is that this CS can be viewed as a linear combination of two coherent states with a phase shift of $\pi/2$ with respect to each other. The Eq. 3.2, indeed, can be written as

$$CS = A\cos\varphi\cos\omega t - A\sin\phi\sin\omega t \tag{3.3}$$

In our apparatus, the optical system MOD1 generates a CS with phase 0, while MOD2 generates a CS with phase $\pi/2$. Therefore by matching these CSs with properly chosen amplitudes (as expressed in eq. 3.3), it is possible to generate our arbitrary CS. In order to perform this operation we designed and realized two parts: an optical one and electronic one. A structured generation/acquisition PC-system allows us to control this process.

Optical layout

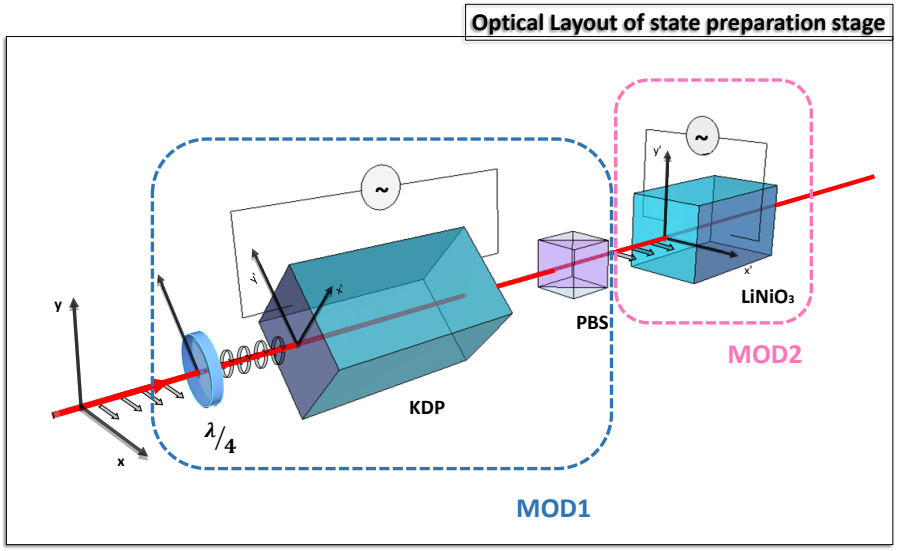

Figure 3.6: Optical layout of the state preparation stage.

MOD1 and MOD2 are two optical systems which are exploited to generate two CS as expressed by Eq. 3.3. For this purpose they are positioned to sequentially intercept the laser beam at 1064 nm as shown in Fig. 3.5. Their optical layout is sketched in more detail in Fig. 3.6. MOD1 consists of a $\lambda/4$ plate, a KDP crystal, and a PBS: the optical field is prepared with circular polarization by setting the fast axis of $\lambda/4$ at an angle of 45° with respect to the incident p polarization, and then it is passed through a KDP crystal whose axes are oriented at 45°. The horizontal component of the output beam selected by the PBS is sent in MOD2, which consists of a $LiNbO_3$ crystal whose extraordinary axis is horizontal. The physical phenomenon underlying this system is the electro-optic effect, which consists in the change of the index of refraction of certain anisotropic materials resulting from the application of an electric field. This effect can be exploit to design electro-optic modulators [13][41]. The basic idea behind these electro-optic devices is to alter the optical properties of a material by applying a voltage in a controlled way. Depending on the device configuration, it is possible to vary phase, polarization, amplitude , frequency , or direction of propagation of the light beam. In particular, the KDP crystal in MOD1 configuration is usually used as an amplitude modulator, while $LiNbO_3$ crystal in MOD2 configuration is used as a phase modulator as described in detail in Ref. [13]. In this context, these devices, instead, are used to generate two coherent states phase-shifted by $\pi/2$.

Electronic layout

In order to control this process via PC, we implemented two identical electronic circuits which drive MOD1 and MOD2. They consist of a phase shifter ($\Psi_{1,2}$ in fig 3.5) and a mixer ($\otimes$). A voltage signal, A(B)=cost, generated by PC, is sent to the mixer together with the sinusoidally varying signal at frequency $\Omega/2\pi = 3MHz$ (sidebands). The mixer combines them and its output, $A\cos(\Omega t + \Psi_1)$ ($B\cos(\Omega t + \Psi_1)$) is sent to MOD1 (MOD2). These two optical systems generate two CSs with a $\pi/2$ phase shift only if $\Psi_1 = \Psi_2$. Therefore the two phase shifters are used in order to set $\Psi_1 = \Psi_2$ so that the modulation signals are in phase when they reach MOD1 and MOD2.

Ramp generator (RG)

The generated states are acquired by means of the Homodyne detector (HD) whose features will be described in the remainder of this chapter. In HD, the LO phase θ is scanned from 0 to 2π thanks to a piezomounted mirror (PZT) which intercepts the LO optical path. In this way we can acquire the homodyne trace of our generated states as function of θ. The PZT is driven by a ramp generator (RG) custom built in order to ensure the synchronization between the generation and the acquisition processes. This is, as we shall see, a necessary feature when we want to generate and observe mixtures of CSs.

The core of this circuit is a function generator which generates a triangle-shaped waveform. This process is triggered by a rectangular function with the two pulse widths (positive and negative) different in time. When square waveforms are used as "clock" signals the time of the positive pulse width is known as the "Duty Cycle" of the period. For example, if we have a square waveform for which the positive or "ON" time is equal to the negative or "OFF" time, the duty cycle is 50% of its period. On the falling edge of the rectangular wave, the positive rise of the ramp which drives the LO PZT starts as shown in fig. 3.7. With our RG we can change the pulse width along with the duty cycle and therefore we can appropriately set the ramp time and the number of PZT oscillations in that time.

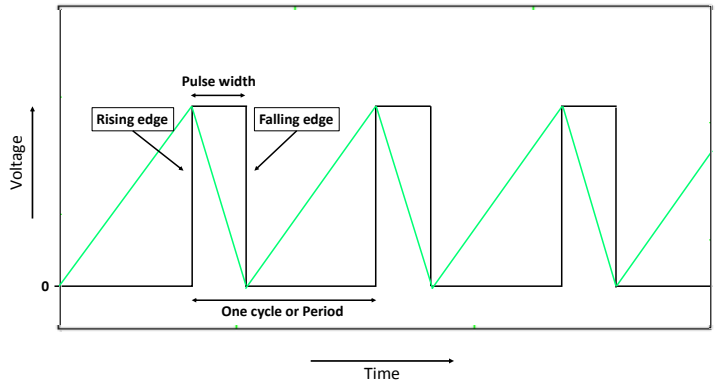

Figure 3.7: The ramp generator (RG) output which drives the LO PZT. generates a triangle-shaped waveform triggered by a rectangular function with the two pulse widths (positive and negative) different in time: on the falling edge of the rectangular wave, the positive rise of the ramp. Its pulse width along with the duty cycle can be changed.

The rectangular wave of RG is used as trigger for the generation and acquisition processes allowing their synchronization. Indeed the timing of the generation/acquisition task is tuned by imposing that the two processes start after the same time from the wave falling edge. In this way the start of the pulse train generation is synchronized with the start of the data acquisition. Besides, the two processes occur in the same time window at the same sampling rate. In order to monitor this, we developed the PC-control system explained below.

Engineering of generation process

In our apparatus we can control the generation process together with the one for the data acquisition via PC. We developed a control system based on LabVIEW programming environment, since it provides powerful programming tools for data acquisition and signal processing. It is structured in three separate parts whose main operations can be followed by the sort of ”flow charts” illustrated in fig 3.8.

Below we will focus on each of them individually, by following the specific sequence with which they run. Each part will be explained along with the help of graphical user interface screenshots.

- **The first step**

  The fist steps consist in acquiring the vacuum state (obtained putting the PC-generated voltage values equal to zero) and calculating its variance (see the screenshot in fig.3.9). In the work presented here, all the homodyne measurements are normalized so that the variance of the vacuum state is equal to 1. Therefore the variance value is saved in a file that will be read from the two following ”programs” which will process it to normalize all the acquired experimental data.

- **The second step**

  The second part generates a train of identical voltage values A which are sent to MOD1 through the electronic circuit described above. MOD1 generates a coherent state with a mean photon number, (n_{ph}), which depends on the response of the KDP crystal to the applied voltage.

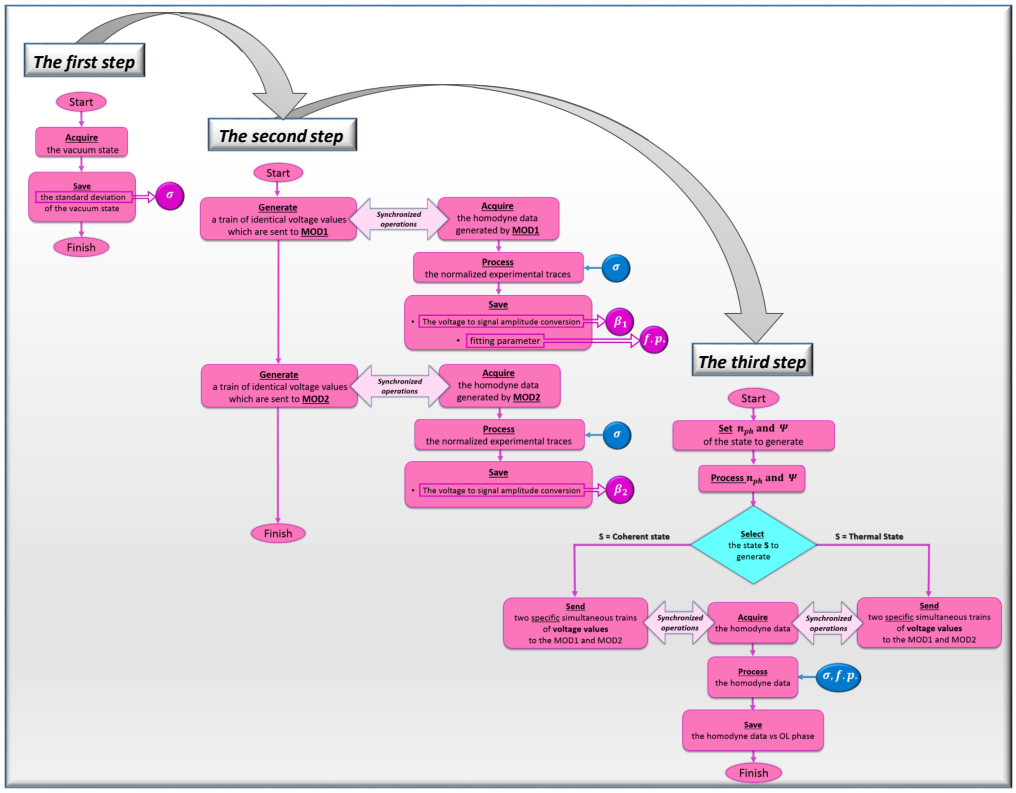

Figure 3.8: The "Flow charts" of the main operations developed in Labview program in order to control the generation and acquisition processes.

The generation and acquisition operations are synchronized with each other, meaning that each generated point is simultaneously recorded. As we already mentioned, the rectangular wave of RG is used as trigger for the two processes: they begin after the same selectable time from the wave falling edge. The operator can set the acquisition time window and the sampling rate. These two parameters determine the number of the generated/recorded data points. In the example shown in Fig. 3.10, we set a time window of 70 ms with a repetition rate of 100 kHz so that we collect 7000 data points.

In the homodyne detection it is necessary to associate the right phase value θ to a certain measured quadrature $X(\theta)$. However, the voltage-dependent displacement of LO PZT actuators doesn't vary linearly with the applied voltage. In order to overcome this trouble, once the data are recorded, they are processed as follows: the experimental data are fitted according to a fitting function of the form: $a + b\cos(cx + d + ex^2)$. The fitting parameters are used to linearise the phase variation. Besides from them it is possible to derive the voltage to signal amplitude conversion β_1 and therefore the voltage to n_{ph} conversion. At this point of our analysis, we know the KPD response to the applied voltage and therefore we can drive it in a controlled manner. The same operations are repeated on MOD2 in order to obtain the voltage to signal amplitude conversion β_2 corresponding to

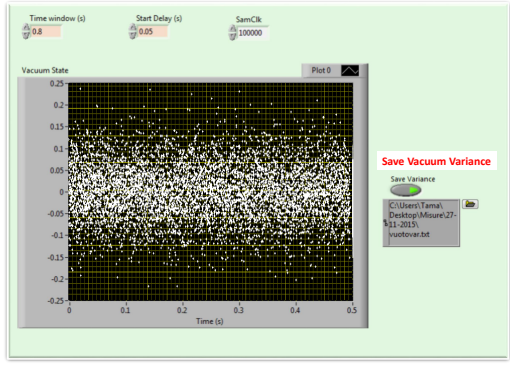

Figure 3.9: Screenshot of the first step of the generation/acquisition process. It is consist in acquiring the vacuum states and saving its variance.

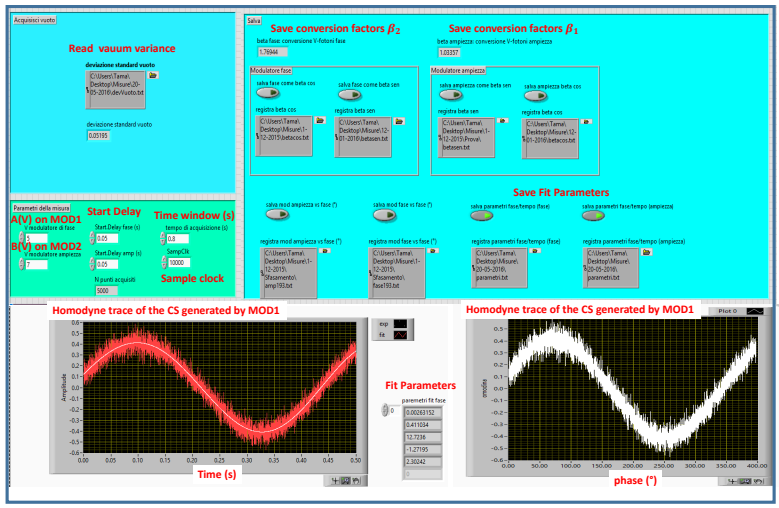

Figure 3.10: Screenshot of the second step of the generation/acquisition process.

$LiNbO_3$ crystal.

- **The third step**

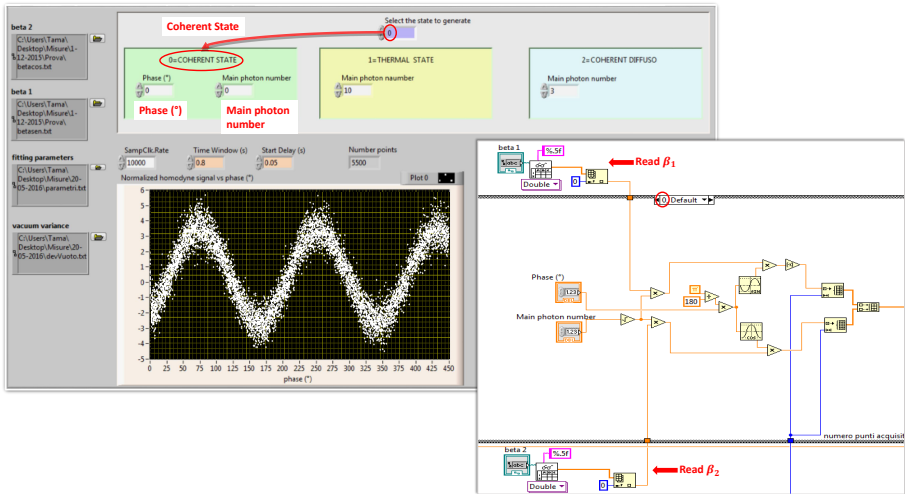

Figure 3.11: The screenshot of the front panel when we choose to generate a CS with selectable main photon number and phase. Once these parameters are set, the software reads β_1 and β_2 saved in the previous step and generates the right voltage value to be sent to MOD1 and MOD2, according to the sequence illustrated in the block diagram at the bottom right corner.

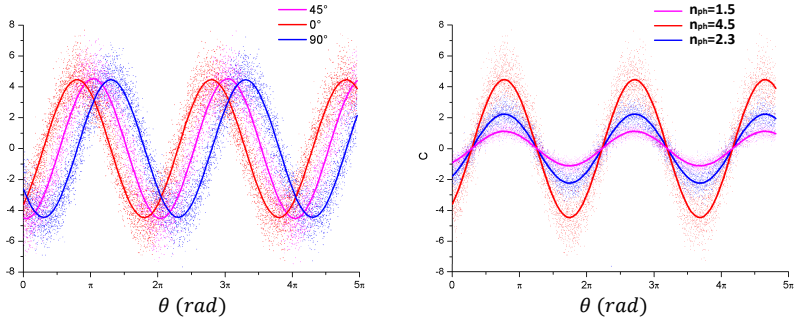

Figure 3.12: Coherent States generated by choosing the main photon number, n_{ph} and phase, φ on demand. On the right the homodyne traces corresponding to three coherent states generated by setting $\varphi = 0$ and $n_{ph} = 1.5$,$n_{ph} = 2.3$ and $n_{ph} = 4.5$ are shown, on the left three coherent states with the same main photon number, $n_{ph} = 4.5$ but with different phase values, $\varphi_1 = 0$,$\varphi_2 = \pi/4$ and $\varphi_3 = \pi/2$ are plotted. The fitted curves (continuous lines) parameters, amplitude and phase, are in agreement with the values which we have chosen to set.

The last step allows to set the amplitude A and the phase φ of the state which

we want to generate. Once these values are set, the "program" process them by reading the data files (β_1, β_2), saved in the previous step, and converting them into two specific and simultaneous trains of voltage values which are sent to the crystals. In the software configuration considered here, the user can choose to generate two kinds of states: coherent and thermal states.

1. *Coherent state*

   In Fig. 3.11 we can see the screenshot of the front panel which occur when we choose to generate a CS with selectable n_{ph} and φ. Once these parameters are set, the software reads β_1 and β_2 and generates the right voltage value to be sent to MOD1 and MOD2, according to the sequence illustrated in the block diagram at the bottom right corner of Fig. 3.11.

   This enables the CS generation under controlled conditions: Fig. 3.12 show the homodyne traces corresponding to three CSs generated by setting $\varphi = 0$ and different values for the main photon number, $n_{ph} = 1.5$, $n_{ph} = 2.3$ and $n_{ph} = 4.5$ on the right, and three CSs with the same main photon number, $n_{ph} = 4.5$ but with different phase values, $\varphi_1 = 0$, $\varphi_2 = \pi/4$ and $\varphi_3 = \pi/2$, on the left. The fitted curves (continuous lines in Fig. 3.12) parameters, amplitude and phase, are in agreement with the values which we have chosen to set.

2. *Thermal state*

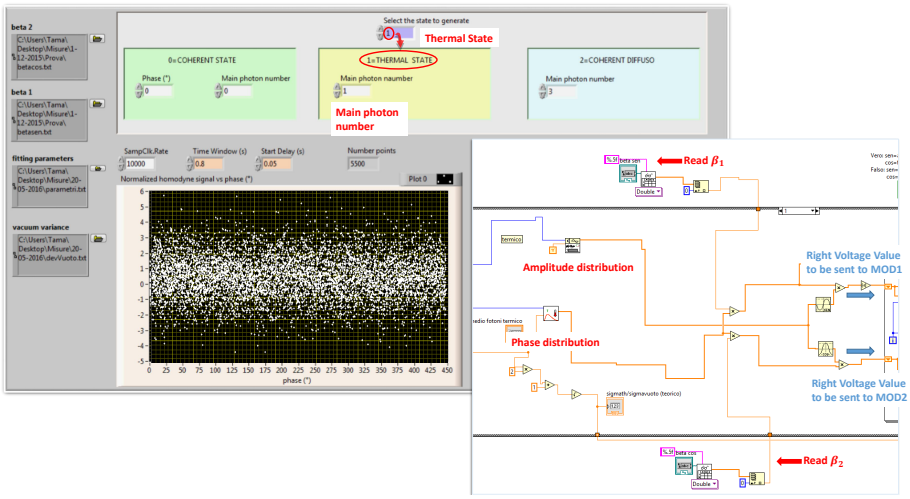

Figure 3.13: Screenshot of the third step of the generation/acquisition process when we want to generate a termal state by setting the main photon number on demand.

Our aim now is to generate a thermal state by setting n_{ph} at will. The density matrix of a thermal state (see Sec. 1.2.3) in the Glauber representation reads as follows

$$\hat{\rho}(\tilde{n}_{\rm th}) = \int_0^\infty d|\alpha| \frac{2|\alpha|}{\tilde{n}_{\rm th}} e^{-\frac{|\alpha|^2}{\tilde{n}_{\rm th}}} \int_0^{2\pi} \frac{d\phi}{2\pi} ||\alpha|e^{i\phi}\rangle\langle|\alpha|e^{i\phi}|\,, \tag{3.4}$$

i.e., it can be viewed as a mixture of coherent states with phase ϕ uniformly distributed over the range 0 to 2π, and a given amplitude $|\alpha|$ distribution. Therefore, we have to generate a rapid sequence of coherent states with $|\alpha|$

and ϕ randomly selected from these distributions. The pc generates random $|\alpha|$ and ϕ values according to their specified distributions and converts them in two simultaneous trains of voltage values which are sent to the crystals. The code of the block diagram which performs this task is shown at the bottom right-hand of Fig. 3.13. For each pair of generated voltage value, the "program" acquires a homodyne point in a synchronised way and this operation is repeated in the time window and with the repetition rate which we set. It is worth noting that the proper synchronization between the generated signal and the acquisition is the basic feature to the optimal working of the system. Finally the data are properly converted (by reading the vacuum state variance and fitting parameters which allow to linearise the LO phase variation) and displayed.

3.3.2 Squeezed state generation: OPO.

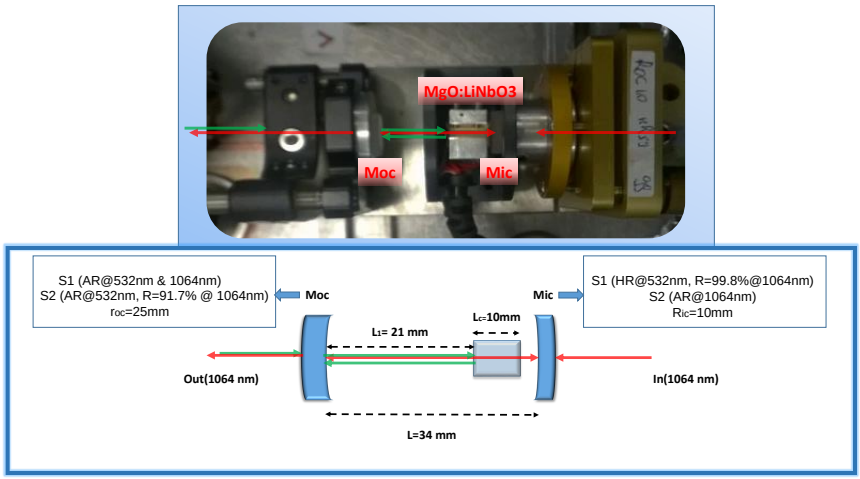

Figure 3.14: Schematic diagram of the optical parametric oscillator (OPO) with its photo. It is a linear optical resonator consisting of two concave mirrors with radii of curvature r_{ic}=10mm, r_{oc}=25mm and separation L, and a MgO:LiNbO3 crystal length L_c=10mm.

The optical layout of the OPO used to generate the squeezed field is depicted in Fig. 3.14 in which its size and the mirror features are indicated. It is a linear optical resonator consisting of two concave mirrors with radii of curvature r_{ic}=10mm, r_{oc}=25mm and separation L, and a MgO:LiNbO3 crystal length L_c=10mm. Such a crystal was chosen as the nonlinear medium for the optical parametric oscillation in virtue of its relatively high nonlinearity and its compatibility with the Nd:YAG laser wavelength. The Magnesium oxide doping (5%) was introduced into bulk Lithium Niobate for the prevention of photorefractive damage. The input coupler (M_{ic}) has the flat surface that is anti-reflection (AR) coated @1064 nm and the curved surface with a reflectivity of R_{ic}=99.8 % at 1064 nm and the coating for high reflection (HR) at 532 nm. The output coupler (M_{oc}) has the curved surface AR coated at 532 nm and a reflectivity of R_{oc}=91.7%

at 1064 nm whereas the other surface is AR coated at both wavelengths. The internal loss for single pass, due to the two faces of the crystal, is estimated as $\Delta = 2.42 \times 10^{-3}$.

An optical resonator confines and stores light at resonance frequencies determined by its configuration. It may be viewed as an optical transmission system that incorporates a feedback: the light circulates or is repeatedly reflected within it.[41] The condition for a stable resonator, that means a resonator which builds up a resonant wave, can be derived. It results in the stability criterion which for two mirror cavity can be written as [46]:

$$0 \leq g_{ic} g_{oc} \leq 1 \quad with \quad g_i = 1 - \frac{L_{eff}}{r_i},\ i = ic, oc; \tag{3.5}$$

where L_{eff} is the effective length of the resonator, which takes account of the presence of the non linear crystal inside the cavity, $L_{eff} = L_1 + (L - L_1) + L_c n_0(\lambda, T)$, being n_0 MgO:LiNbO3's ordinary refractive index depending on the wavelength λ and temperature T. Based on this criterion we find that for a given set of mirror curvatures, resonance only occurs for a restricted range of cavity lengths. We have to choose the length and the curvatures together. Our OPO cavity is designed in order to satisfy this stability condition and in such a way that it is not confocal. Therefore the changes in the resonance frequencies $\Delta\nu_{nm}$ for the modes TEM_{mn} away from the resonance of the fundamental mode are clearly visible [13]. The beam waist is minimum in the crystal center. This requirement ensures a high conversion efficiency and the non-criticality of the phase matching condition. The OPO cavity thus designed has a *finesse* [3] F = 67 and the free spectral range is FSR = 3300 MHz, which corresponds to a linewidth of about 55 MHz.

By considering these cavity parameters, the links between the transmitted power (P_{out}) with the input one (P_{in}) as functions of detuning $\delta\nu$ reads as [13]

$$\frac{P_{out}}{P_{in}} = \frac{(1 - R_{ic})(1 - R_{oc}) \left| \sqrt{R_{oc} R_{ic} (1 - \Delta)^2} e^{-\imath 2\pi \frac{\delta\nu}{FSR}} \right|}{\sqrt{R_{ic} R_{oc}} \left| 1 - \sqrt{R_{oc} R_{ic} (1 - \Delta)^2} e^{-\imath 2\pi \frac{\delta\nu}{FSR}} \right|^2} \tag{3.6}$$

and the power of the field inside the cavity can be written as:

$$\frac{P_{cav}}{P_{in}} = \frac{1 - R_{ic}}{\left| 1 - \sqrt{R_{oc} R_{ic} (1 - \Delta)^2} e^{-\imath 2\pi \frac{\delta\nu}{FSR}} \right|^2} \tag{3.7}$$

The response of cavity is shown in Fig. 3.15.

[3] The *finesse* of an optical resonator is defined as

$$F = \frac{FSR}{FWHM}$$

where FWHM is the Full Width at Half-Maximum bandwidth of cavity resonances. The finesse is generally used as a measure for the quality of cavity. It is easy to show that

$$F = \frac{\pi \left(R_{oc} R_{ic} (1 - \Delta)^2 \right)^{1/4}}{1 - \sqrt{R_{oc} R_{ic} (1 - \Delta)^2}}$$

in which one can explicitly see that it is fully determined by the resonator losses and it is independent of the resonator length.

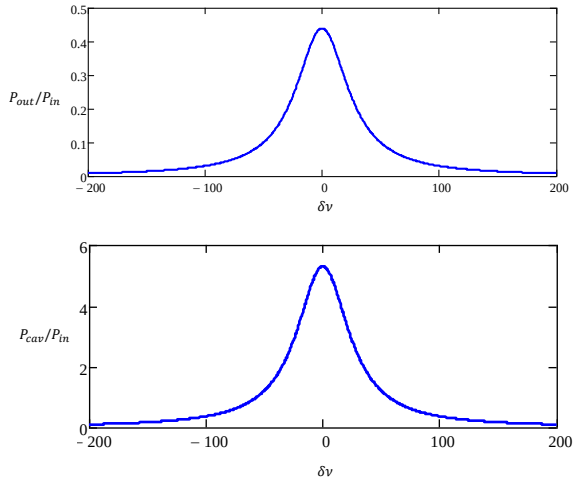

Figure 3.15: Cavity response. Upper panel: expected link between the transmitted (P_{out}) with the input power (P_{in}) as function of OPO detuning δv, by considering the parameters of our cavity. Lower panel: OPO internal field.

The ideal situation for transmitting the laser light through an external cavity would be to have the external cavity length fixed, with the frequency of the laser light resonant with the frequency of one of the modes of the cavity. Furthermore, the spatial profile of the incident laser beam would ideally be matched to a transverse mode of the passive optical cavity: since the laser light propagates in a TEM_{00} mode (by which we mean the fundamental transverse mode of the laser resonator), we would ideally want to match it with the fundamental transverse mode (TEM_{00}) of the external cavity. Such mode matching does not occur automatically, since the fundamental external cavity mode will have its beam width and radius of curvature, entirely independent of the parameters of the laser resonator. Therefore the experimental situation is more complex than the ideal case and aligning an optical resonator to a laser beam is non-trivial. If the laser beam is not perfectly aligned and mode-matched to the external cavity, the input beam will partially couple to many different transverse modes of the optical cavity and the light exiting the cavity will feature all the excited modes rather than maintaining the spatial profile of the input beam.

To mode-match the laser TEM_{00} mode to that of the external cavity mode, lenses having a specific focal length and placed at a specific location between the laser and the resonator must be used to shape the incoming beam. One of mathematical tools for studying the cavities is the ABCD matrix formalism. It is a ray optics formalism whereby we can monitor the evolution of an optical beam as is propagates through optical elements. An excellent overview can be found in Ref. [46]. By using it, we studied how the radius of curvature of the wavefront R(z) and the size w(z) of the beam propagate in the cavity in order to obtain the best possible mode matching. (Recall here that the ABCD formalism is based on the paraxial approximation: the optical rays remain confined around the optical axis z). From the behaviour of w(z) and R(z) inside our cavity, shown in Fig. 3.16, we have to propagate the beam through the mirror M_{ic}, in order to find the beam size outside the cavity. By studying the free-space propagation from the

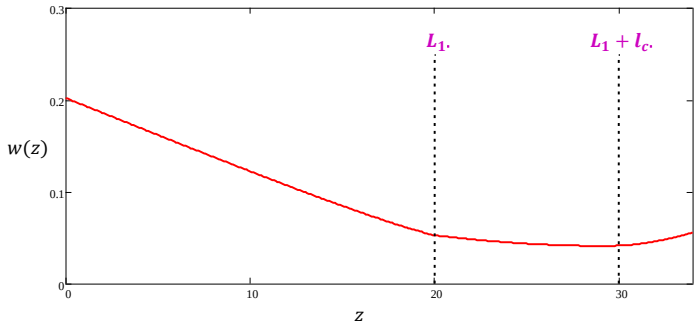

Figure 3.16: Propagation of the mode waist w(z) inside the cavity

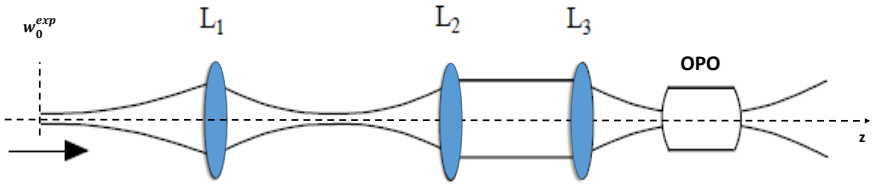

Figure 3.17: Precise mode matching of a Gaussian beam via telescopic lens arrangement. With the combination of L_1 and L_2 combination we collimate the beam. L_3 is used to achieve the desired beam waist in the crystal center.

flat face of mirror M_{ic}, we can retrieve the focal length f3 of the lens L_3 in Fig. 3.17. By measuring w_0 e R_0 at the laser output, we can deduce the possible lenses to be used for the telescopic system L_1+L_2.

The mode matching of the laser beam to the OPO is an iterative process and aligning the overall system is non trivial.

The alignment procedure reads as follow:

1. The two mirrors M1 and M2 shown in Fig. 3.18 are used as alignment tool for directing the beam so that it is parallel to the table at a convenient height above it. This is an iterative process performed with aid of mounted iris or other height marker.

2. We place the lens L_3 on the optical beam path in the right location, so that the beam hits the iris centres. After inserting the lens, we can observe the beam spot with a CCD camera in order to take a further benchmark.

3. We insert the non linear crystal. We make sure that the beam crosses the centre of the crystal and hits the centres of the markers previously taken.

4. Now we can align the two mirrors of the optical cavity.

    - First of all, we set up the M_{oc} at the correct distance from the crystal so that the beam hits the mirror near its center. We direct the mirror so that the back-reflected beam overlap the forward propagating beam.

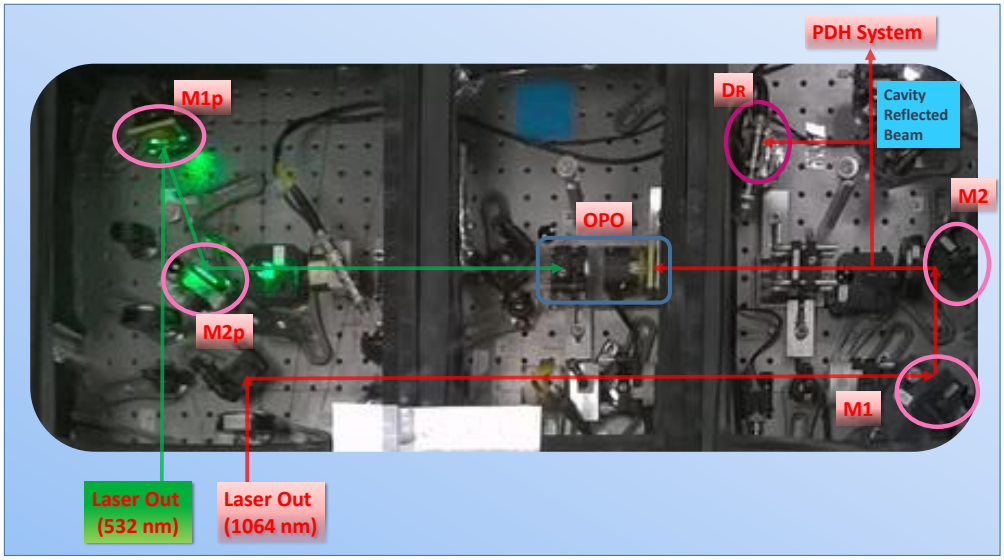

Figure 3.18: Photo of the OPO in which the optical elements used to achieve the mode-matching are highlighted.

- We put the detector labelled as D_R in Fig. 3.18 on the cavity reflected beam (channelled through a beam splitter (BS_1)) in order to monitor its power.
- We install the second mirror M_{ic} so that its surface is facing M_{oc} and the beam hits its center. We adjust M_{ic} by maximising the reflected beam intensity.
- We should now have a cavity that is close to being aligned. If the alignment is very close, we may see flickering of light on observation screen for the transmitted light. If the alignment is only somewhat close, we may be able to see a couple of dim intensity spots, and not much flickering. We use the adjustments on the two cavity mirrors to overlap these spots.

5. When the cavity is aligned to the incident beam, we should be able to see the time dependent coupling of the laser light to the modes of the cavity when the resonator mirror M_{ic} is scanned back and forth using a piezo element so that the length of the resonator changes in a periodic manner. Different transverse modes will in general have different resonant frequencies and the laser light can couple to different transverse modes of the cavity. A perfectly mode matched cavity will only transmit the incident laser mode (TEM_{00}): the transmitted TEM_{00} mode should be very bright when resonant, while the other modes greatly suppressed. We maximize the transmitted intensity by adjusting the cavity alignment and the position of the incident beam waist with L_3 which can be useful for the fine tuning of the mode matching.

MgO:LiNbO3's refractive index is strongly depend on temperature, and temperature tuning was used to achieve noncritical phase matching. The phase matching condition of this system, can be obtained from temperature-dependent Sellmeier equations[49]:

$$n_0^2(\lambda,T) = 4.913 + \frac{1.173\cdot 10^5 + 1.65\cdot 10^{-2}T^2}{(\lambda\cdot 10^3)^2 - (2.12\cdot 10^2 + 2.7\cdot 10^{-5}T^2)^2} - 2.78\cdot 10^{-8}\left(\lambda\cdot 10^3\right)^2 \qquad (3.8)$$

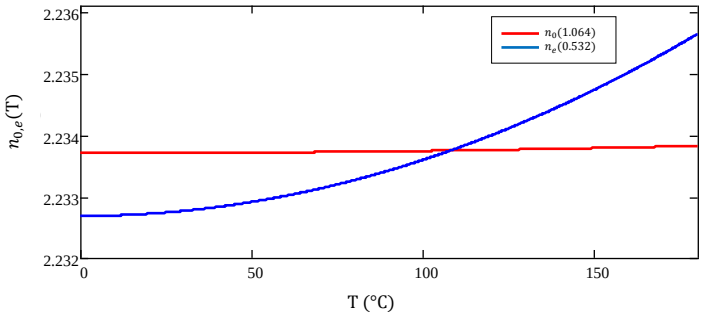

Figure 3.19: The ordinary refractive index, n_0, and extraordinary refractive index, n_e of $MgO:LiNbO_3$ as functions of the temperature.

$$n_e^2(\lambda,T) = 4.5567 + \frac{0.97\cdot 10^5 + 2.7\cdot 10^{-2}T^2}{(\lambda\cdot 10^3)^2 - (2.01\cdot 10^2 + 5.4\cdot 10^{-5}T^2)^2} - 2.24\cdot 10^{-8}(\lambda\cdot 10^3)^2 + 2.605\cdot 10^{-7}T^2 - 2.1432\cdot 10^{-4}T_{NCPM} + 4.96\cdot 10^{-6}T_{NCPM}^2 \quad (3.9)$$

which express the ordinary refractive index, n_0, and the extraordinary refractive index, n_e as functions of the temperature and the wavelength λ. Here we have omitted the dimensions for simplicity and T_{NCPM}=108 ° C is the temperature of noncritical phase matching for 1.064 μm $\Rightarrow$ 0.532 μm SHG interaction. Fig. 3.19 shows $n_0(\lambda_1,T)$ and $n_0(\lambda_2,T)$, with λ_1=1.064 μm and λ_2=0.532 μm, as functions of T. The phase mismatch is then

$$\Delta k(\lambda,T) = \frac{2\pi}{\lambda}n_e(\lambda,T) - \frac{2\pi}{\lambda}n_0(2\lambda,T) \quad (3.10)$$

The effect of phase mismatch on the non-linear interaction strength is given by [42]

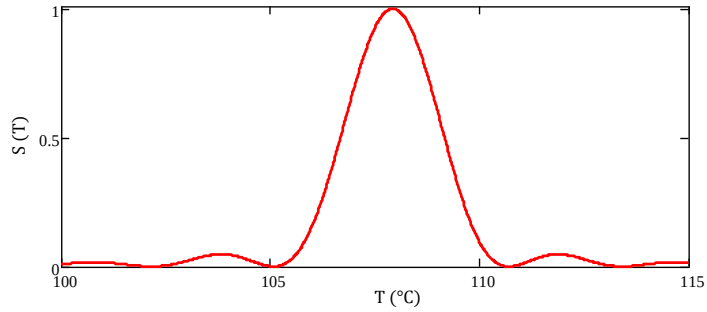

Figure 3.20: The effect of phase mismatch on the non-linear interaction strength using $MgO:LiNbO_3$

$$S(\lambda,T,z) = sinc\left(\frac{\Delta k(\lambda,T)z}{2}\right)e^{i\Delta k(\lambda,T)\frac{z}{2}} \quad (3.11)$$

where z is the interaction length within the nonlinear medium. Fig. 3.20 plots S(λ, T, z) as a function of temperature and for the interaction length z=L_c=10 mm. We see that the

optimum nonlinearity occurs at 108°C whereas the experimental temperature is about 108.6°C.

3.3.3 Pump optical layout

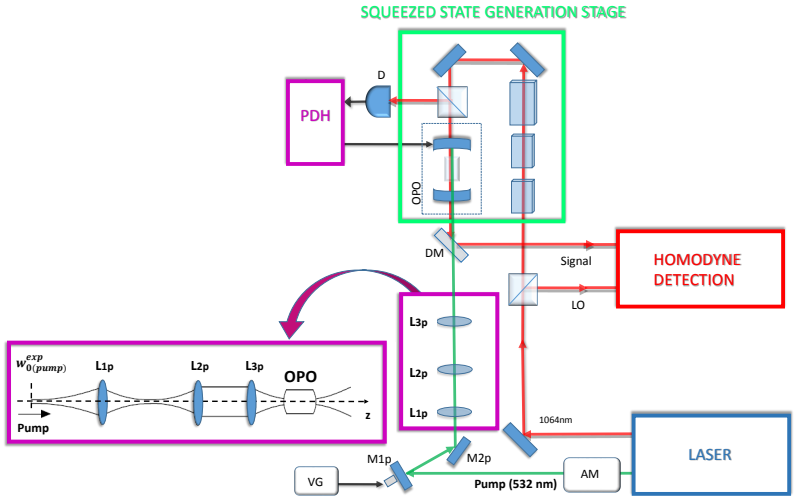

Figure 3.21: Pump optical layout.

The second harmonic field generated inside the laser cavity is used to pump the OPO which is seeded with the field at the fundamental frequency. When a nonlinear medium inside an optical cavity is irradiated with a pump beam, the signal generated on the first pass trough the medium by OPG can act as an input on consecutive passes, if it is coupled into the cavity. The signal builds up within the cavity if it fulfils the resonance condition of the cavity. In our case the OPO cavity is resonant with the field at the fundamental frequency. Thus, the pump field (532 nm) enters and leaves the OPO cavity through the out-coupling mirror immediately after crossing the crystal forward and backward, whereas the fundamental seed field (1064 nm) enters the OPO through the input coupler and could resonate within the cavity.

In order to optimise the non linear process efficiency we have to shape the pump beam. The optimum beam waist for the pump in the non linear crystal is given by [50]:

$$\frac{w_{532}}{w_{1064}} = \frac{1}{\sqrt{2}}\sqrt{\frac{n_0\,(1064)}{n_e\,(532)}} \tag{3.12}$$

Therefore we have to design a lenses system in such a way that w_{532}=33μm inside the crystal, since w_{1064}=46μm. By following a procedure similar to that specified for the seed, we can study the behaviour of w_{532} and R_{532} inside the cavity (see Fig.) and outside the OPO output coupler. Fig. 3.22 show the behaviour of w(z) of the seed (red), already shown in Fig. 3.16, compared to the behaviour w(z) of the pump (green) inside the cavity. We can retrieve the focal length $f3_p$ of the lens L_{3p} in Fig. 3.21 and then $f1_p$ and $f2_p$ of the telescopic system L_{1p}+L_{2p}. By channelling the pump beam by means the

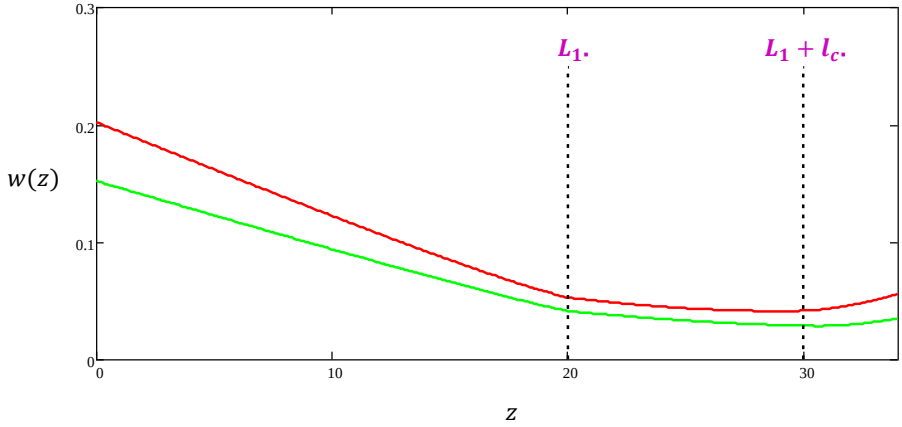

Figure 3.22: Propagation of the mode waist w(z) of the seed field (red) and of the pump beam (green) inside the cavity.

two mirror labelled $M1_p$ and $M2_p$ in Fig. 3.21, we can align it inside the OPO cavity. Fig. 3.18, instead, shows a photo of the pump optical layout where we can see the real placement of $M1_p$ and $M2_p$. By finely adjusting the separation between L_{1p} and L_{2p} we optimize w_{532} inside the OPO. The tool used to check the mode matching and the alignment between the seed and the pump inside the crystal is the regenerative gain G of the OPO's amplification, defined as the ratio of the output power with and without the second harmonic pump field. We have seen in Sec. 2.5. Such a gain can be written as a function of pump field power, P, and the OPO threshold, P_{th}, as:

$$G_{\pm} = \frac{1}{\left(1 \pm \sqrt{\frac{P}{P_{th}}}\right)^2} \tag{3.13}$$

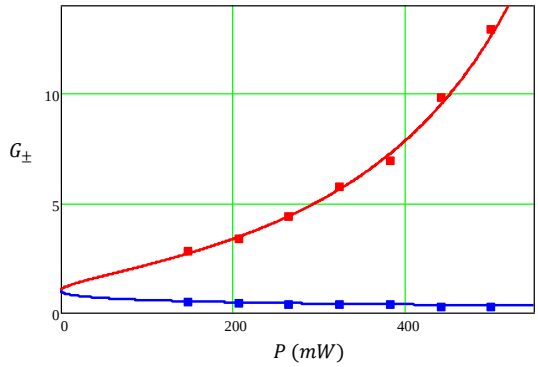

Figure 3.23: Measurements of the gain of the parametric amplification as functions of pump power P. By fitting the experimental data with expression in 3.13 we retrieve that the OPO threshold is P_{th}=970 mW.

The pump phase is changed by means a piezo-mounted mirror. By driving it with

a triangular waveform (VG in Fig. 3.21) we can measure the gain $G_{\pm}$ as function of P which is set with the amplitude modulator, AM in Fig. 3.21.

By measuring the gain of the parametric amplification as a function of pump power P and by fitting the experimental data with expression in 3.13 we can retrieve the OPO threshold, P_{th}. In our case we find P_{th}=970 mW (see Fig. 3.23)

3.4 PDH

In this Section we will describe how an error signal can be derived to hold the OPO resonant with the frequency of the laser mode. In our apparatus we use an active stabilization based on the Pound-Drever-Hall (PDH) technique [51] [52] whereby the length of the resonator can be controlled. The idea behind this method is that the information about whether the cavity is above or below the resonance, is encoded in the phase of the total reflected electric field of the cavity.

As we defined the response of the OPO cavity for the transmitted light, we define the one for the reflected light. The reflection coefficient F(ω) is the ratio between the electric fields of the reflected beam, E_{ref} and the incident beam E_{in}

$$F(\omega) = \frac{E_{ref}}{E_{in}} = \frac{g(\omega) - R_{in}}{1 - g(\omega)} \sqrt{R_{in}} \tag{3.14}$$

where we have put

$$g(\omega) = \sqrt{R_{oc} R_{ic} (1 - \Delta^2)} e^{-\imath 2\pi \frac{\delta\nu}{FSR}} \tag{3.15}$$

Fig. 3.24 shows the intensity of the reflected beam, $|F(\omega)|^2$ and the phase response. We see that the phase is a function which changes sign at the cavity line center. Therefore

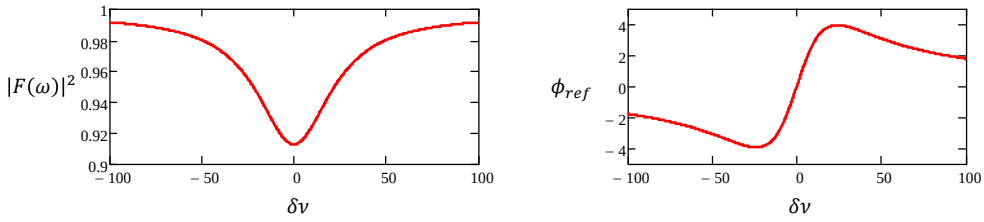

Figure 3.24: Magnitude and phase of the reflection coefficient for the OPO cavity.

it enables a distinction between different cavity positions in frequency. Since direct phase measurements are not possible, one needs to probe quantities which are in some way coupled to it. It's worth noting that this is just the key point in the PDH technique: the generation of an error signal which samples the phase of the reflected electric field from the cavity. In order to extract information about the phase, a phase modulator is placed between the laser and the cavity and the light reflected from the cavity is detected. In this way the incident beam on the cavity is phase-modulated with a certain frequency and its electric field becomes:

$$\begin{aligned} E_{in} &= E_0 e^{\imath(\omega t + \beta \sin \Omega t)} \\ &\approx E_0 \left[J_0(\beta) e^{\imath\omega t} + J_1(\beta) e^{\imath(\omega+\Omega)t} - J_1(\beta) e^{\imath(\omega-\Omega)t} \right] \end{aligned} \tag{3.16}$$

where we have used the expansion in terms of Bessel functions [51] [52].

To calculate the reflected beam's field when there are several incident beams, we can treat each beam independently and multiply each one by the reflection coefficient at the appropriate frequency. In the Pound–Drever–Hall setup, where we have a carrier and two sidebands, the total reflected beam is

$$E_{ref} = E_0 \left[F(\omega) J_0(\beta) e^{\imath\omega t} + F(\omega+\Omega) J_1(\beta) e^{\imath(\omega+\Omega)t} - F(\omega-\Omega) J_1(\beta) e^{\imath(\omega-\Omega)t} \right] \tag{3.17}$$

The reflected beam is detected by a photodiode, which measures its power $P_{ref} = \left|E_{ref}\right|^2$. By defining

$$P_c = |E_{in}(r)|^2 J_0^2(\beta) P_{s,n} = |E_{in}(r)|^2 J_n^2(\beta) \tag{3.18}$$

as the optical power in the carrier and the n-th order sidebands, respectively, the reflected power can be written as

$$\begin{aligned} P_{ref} = {} & P_c |F(\omega)|^2 + P_{s,1} \left[|F(\omega+\Omega)|^2 + |F(\omega-\Omega)|^2 \right] \\ & + 2\sqrt{P_c P_{s,1}} \left[\Re\{F(\omega) F^*(\omega+\Omega) - F^*(\omega) F(\omega-\Omega)\} \cos\Omega t \right] \\ & + 2\sqrt{P_c P_{s,1}} \left[\Im\{F(\omega) F^*(\omega+\Omega) - F^*(\omega) F(\omega-\Omega)\} \sin\Omega t \right] + (2\Omega \; terms) \end{aligned} \tag{3.19}$$

which is a signal consisting of stationary terms, terms oscillating at frequency Ω , resulting from interference between the carrier and the sidebands, and higher frequency contributions arising from the sidebands interfering with each other. If the carrier is near the cavity resonance and the modulation frequency is sufficiently high, the sidebands will be totally reflected. In this regime, the expression

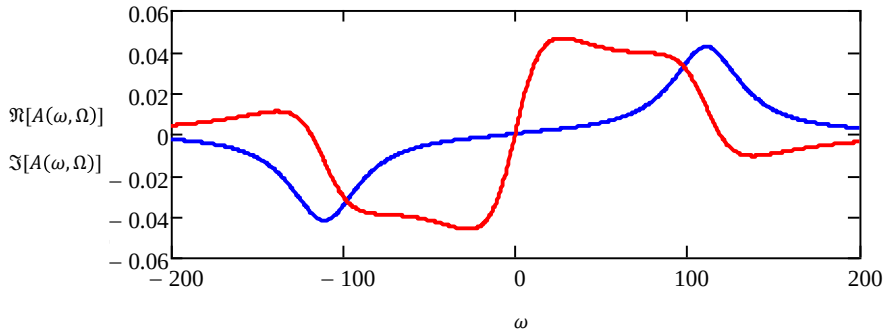

Figure 3.25: Real and imaginary part of the cavity reflection coefficient $A(\omega,\Omega)$ at Ω=111 MHz. $\Im A(\omega,\Omega)$ is a smooth function with odd symmetry around the cavity resonance and therefore represents a suitable candidate for the generation of an error signal.

$$A(\omega,\Omega) = F(\omega) F^*(\omega+\Omega) - F^*(\omega) F(\omega-\Omega) \approx -\imath 2\Im\{F(\omega)\} \tag{3.20}$$

This expression is plotted in Fig. 3.25.

Therefore, the aim is to isolate this component by mixing it with the modulation signal (demodulation). Parts of the terms oscillating at Ω are shifted to DC, whereas all remaining contributions will appear at multiples of the modulation frequency. By ignoring them, the resulting DC component, i.e. the PDH error signal, takes the following form

$$P_{PDH} = -\sqrt{P_c P_{s,1}} \Im\{F(\omega) F^*(\omega+\Omega) - F^*(\omega) F(\omega-\Omega)\} \cos\phi \tag{3.21}$$

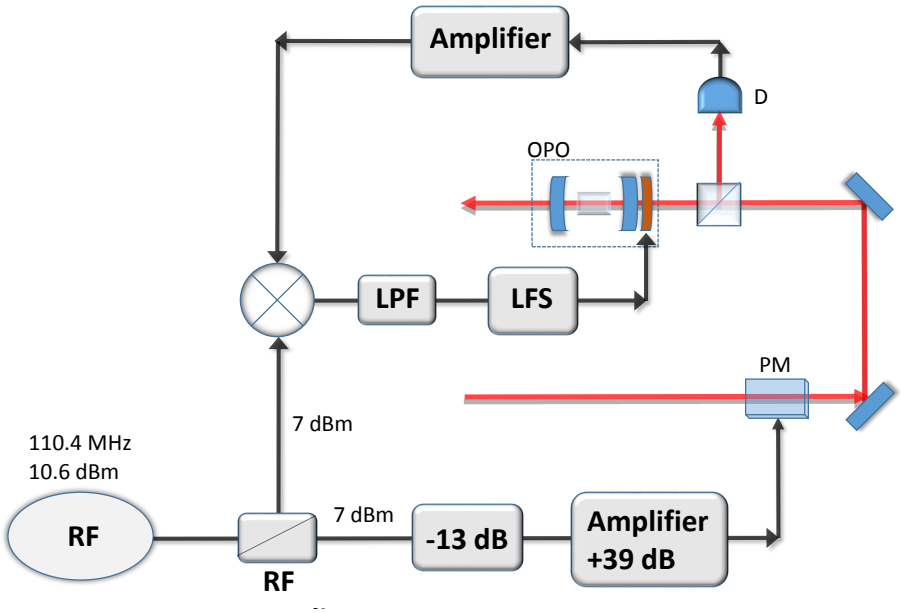

Figure 3.26: Scheme of the system for generating the PDH signal and keeping the cavity length constant.

where ϕ is the phase difference between the mixed signals.

A custom lock system has been realized for generating the PDH signal and keeping the cavity length constant. Fig. 3.26 shows the setup which consist of a high-frequency part and a low-frequency part (LFS). An RF source drives the PM and thereby modulates the input seed of the OPO. The modulation frequency is 110.4 MHz, well above the OPO linewidth. Half of this RF power is picked up by an RF power-splitter and mixed with the signal from the photodiode (D) by means a mixer ($\otimes$). The photodiode signal is amplified before this mixing process to keep a good signal-to-noise ratio. The output of the mixer is a composite signal that contains the frequency components of the source signals, as well as their sums and differences. Therefore, the signal leaving the mixer consists of the PDH error signal at DC, and higher frequency contributions, appearing at multiples of the modulation frequency. These higher frequency contributions are filtered away by means of a low-pass filter (LPF). Lastly, there is the LFS. This last one is used to drive the PZT connected to the rear mirror of the OPO cavity in order to actively control its length. LFS consists of the following parts. First we have an electronic circuit for controlling the offset whereby an external offset signal is added to the PDH input. By adjusting this offset signal, one can cancel a possible offset of the PDH error signal, which would break its symmetry around zero and thereby deteriorate the lock. Then there is a reference electronic circuit through which we can manually set the voltage applied to the PZT until we find the OPO resonance. Now we are ready to turn on the integrator. Lastly, there is a summing circuit which combines signals emerging from the integrator, amplifier and reference circuits.

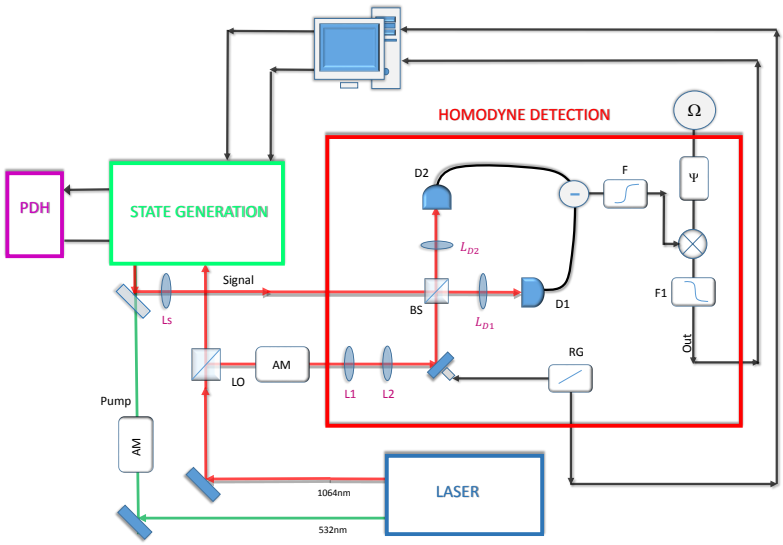

Figure 3.27: Zoom on Homodyne Detection scheme

3.5 Homodyne detection

In order to perform the measurements of the quantum states we implement the Homodyne Detection (HD) scheme whose operating principle has been already explained in Sec. 1.6. It consists (see Fig. 3.27) of a beam splitter, two low noise detector (D1 and D2) and a differential amplifier based on a LMH6624 operational amplifier ($\ominus$). The electronic noise is 17 dB below the vacuum noise at 3 MHz for 10 mW of the LO power. To remove the low frequency signal we use an high-pass filter @500kHz (F) and then the signal is sent to the demodulation apparatus which extracts the information about the signal that is at frequency $\Omega/2\pi$=3 MHz. This apparatus consists of a phase shifter (Ψ) a mixer ($\otimes$) and a low pass filter @300kHz (F1). The output is sent to PC and the acquisition process takes place according to the procedures shown in Sec. 3.3. Unlike ideal situation described above, in the experimental scenario we have to consider the losses resulting from the photodetection process, the non-perfect balancing between the two arms of the HD and the non-optimum spatial mode-matching between the signal and the LO. The inefficiencies linked to each of these factors are addressed separately below.

Inefficiencies in the photodetection process

As previously mentioned, in a realistic scenario we have to take account of the photodiode quantum efficiencies η_D. It is the probability of the incoming light being converted to measurable signal, that is the ratio of the number of photoelectrons released in a photoelectric process to the number of radiation quanta absorbed. If the photodetection is 100 % efficient, each photon in the optical beam should generate one electron in the photodetector current but in real photodectors $\eta_D < 1$ depending on the material and the geometry of the detector, and the wavelength of the light. In order to understand the effect of η_D on a single-mode squeezed vacuum state, we can use the model introduced in Sec. 2.6 and we can model a real photodetector as a beam splitter with transmissivity η_D followed by an ideal photodetector with $\eta = 1$, as shown in Fig. 3.28.

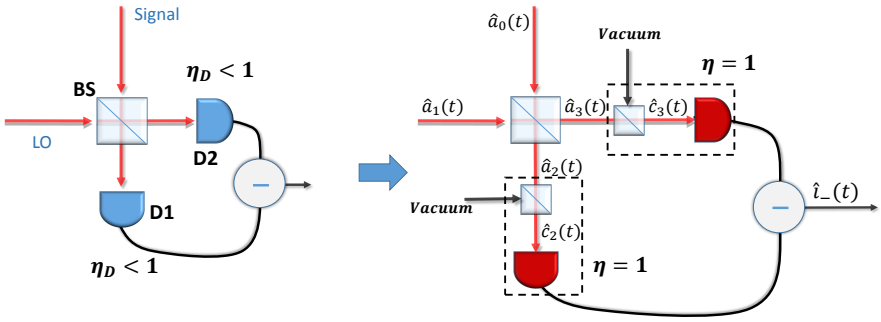

Figure 3.28: Sketch of the homodyne detector showing in which way the quantum efficiencies η_D of the photodiodes is modeled.

Recalling the BS action, the interference of the mode a_i with the vacuum mode b_i, with i=2,3, will produce a mode c_i

$$c_i = \sqrt{\eta}a_i + \imath\sqrt{1-\eta}b_i = \sqrt{\eta}\left\{\frac{1}{\sqrt{2}}(a_0 + \imath a_1)\right\} + \imath\sqrt{1-\eta}b_i \tag{3.22}$$

where, in the last expression, we have considered a 50:50 BS for the homodyne system. Therefore the output photocurrent i_- is

$$\begin{aligned} i_-(t) &\approx \imath\eta_D\left(a_0^\dagger a_1 - a_0 a_1^\dagger\right) + \sqrt{\frac{\eta_D(1-\eta_D)}{2}}\left(b_2^\dagger a_1 - b_2 a_1^\dagger\right) + \sqrt{\frac{\eta_D(1-\eta_D)}{2}}\imath\left(b_2^\dagger a_1 - b_2 a_1^\dagger\right) \\ &= 2\eta_D|\alpha|X_1(t,\theta) + 2\sqrt{\frac{\eta_D(1-\eta_D)}{2}}|\alpha|X_2(t,\theta+\pi/2) + 2\sqrt{\frac{\eta_D(1-\eta_D)}{2}}|\alpha|X_3(t,\theta+\pi) \end{aligned} \tag{3.23}$$

where $|\alpha|$ is the amplitude of the LO a_1 and X_1 and X_2 are uncorrelated. It is thus desirable that photodetectors have high quantum efficiency so that they accurately monitor the optical field. Our detectors have $\eta_D = 0.97$ that is the quantum efficiency of photodiodes corresponding to the manufacturer specifications.

Inefficiencies in the homodyne detection balancing

The degree of balancing, or the signal ratio between the two arms of the homodyne detector is crucial for its performance. From 1.58 we can write

$$\begin{aligned} i_- = &\underbrace{2(gT-R)\sqrt{P_{LO}}X_{LO}}_{(i)} + \underbrace{2(1+g)\sqrt{RT}\left[\sqrt{P_{LO}}X_s(\theta) + \sqrt{P_s}X_{LO}(\theta')\right]}_{(ii)} \\ &+ \underbrace{2(T-gR)\sqrt{P_s}X_s}_{(iii)} \end{aligned} \tag{3.24}$$

where P_i and X_i, with i=s,LO, are the LO and signal powers and field, respectively. $g = g_t/g_r$, where g_i, with i=t,r, is the amplifier gain of the detectors D_i. The three terms in this equation represent the coupling of the LO field into measurement (i), the coupling

of the signal field into the measurement (iii), the LO amplification of the signal field and signal amplification of the LO field (ii). Ideally, the splitting between the arms should be equal, resulting in the terms (i) and (iii) being zero, but in a real situation we have to measure the arms unbalance in order to evaluate its effect on measurements and, in particular, on squeezing. If $P_{LO} \gg P_s$, the signal amplification effect on LO can be neglected. All the measurements presented in this thesis are performed with P_{LO}=10 mW and P_s=1$\div$ 5 μ W. Besides it is easy to show that the efficiency which depends on the not-ideal 50:50 splitting ratio of BS is $\eta_{BS} = 4RT$ and in our apparatus it is negligible being η_{BS}=0.999.

Inefficiencies in optical mode-matching at BS

When the two input optical fields to the BS of the homodyne system are not perfectly mode matched, inefficiency in the homodyne measurement results. The mode mismatch of the fields can have several causes like non identical polarization, difference in spatial modes, lack of optical coherence and all have the same harmful effect to the homodyning. This effect can be viewed as the introduction of higher-order modes into the system, which are occupied by the unsqueezed vacuum state[53]. The schematic model of mode mismatch is shown in Fig. 3.29. Let us imagine that the LO is the overlap between two orthogonal spatial mode, whereas the signal resides only in one spatial mode and, therefore, in the other one (orthogonal) there is the vacuum. In this case the LO will amplify both the signal and vacuum.

In general, the modes at the beam splitter will overlap, and therefore interfere, with some efficiency. Considering only the coherent amplitudes, the fields input at the beam splitter can be written as:

$$\left(a_1(t), a_{1,\perp}(t,)\right) = \left(a_1(t), 0\right)$$

$$\left(a_2(t), a_{2,\perp}(t,)\right) = \left(\sqrt{\eta}a_2(t)\,\sqrt{1-\eta}a_2(t)\right)$$

and the coherent amplitude of the output state is

$$\left(a_r(t), a_{r,\perp}(t)\right) = \frac{1}{\sqrt{2}}\left(a_1(t) + e^{i\theta}\sqrt{\eta}a_2(t), e^{i\theta}\sqrt{1-\eta}a_2(t)\right)$$

Calculating the intensity of the reference and orthogonal modes we obtain:

$$a_r^*(t)\,a_r(t) = \frac{1}{2}\left(a_1^2(t) + \eta a_2^2(t) + 2\sqrt{\eta}\cos\theta a_1(t)\,a_2(t)\right) \tag{3.25a}$$

$$a_{r,\perp}^*(t)\,a_{r,\perp}(t) = \frac{1}{2}\left((1-\eta)\,a_2^2(t)\right) \tag{3.25b}$$

The photocurrent i_r obtained when this total field impinges on a photodetector is given by

$$i_r \propto a_1^2(t) + a_2^2(t) + 2\sqrt{\eta}\cos\theta a_1(t)\,a_2(t) \tag{3.26}$$

Notice that as the relative phase between the input modes changes we observe an interference fringe. The visibility V of this fringe is defined as

$$V = \frac{max_\theta\{i_r\} - min_\theta\{i_r\}}{max_\theta\{i_r\} + min_\theta\{i_r\}} = \frac{2\sqrt{\eta}a_1(t)\,a_2(t)}{a_1^2(t) + a_2^2(t)} \tag{3.27}$$

.

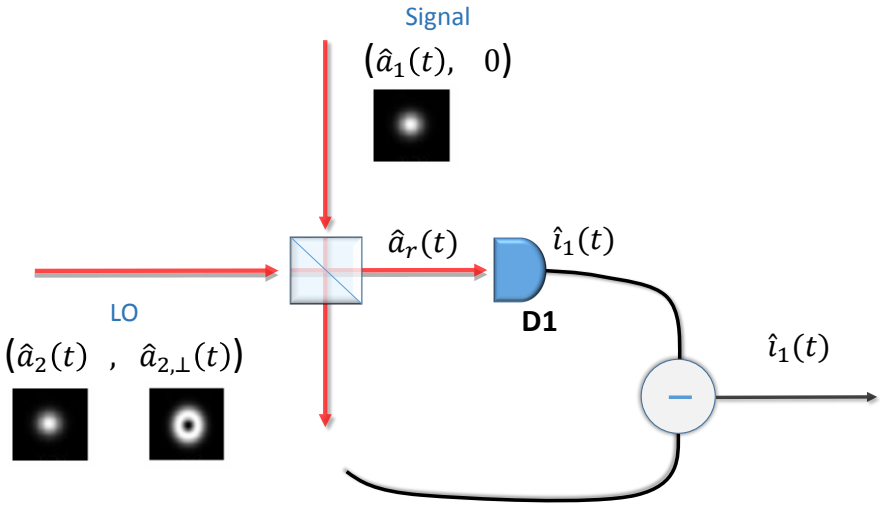

Figure 3.29: Schematic models of mode mismatch at BS in Homodyne Detector

If the power in each of the input modes is arranged to be equal we obtain a simple relationship between the visibility and mode-matching efficiency of the interference

$$\eta_{vis} = V^2 \tag{3.28}$$

By using an amplitude modulator (AM in Fig. 3.27) that consists of an HWP and a BP, it is possible to arrange the power of the two BS input beams to be equal. Therefore, once the powers are balanced, we can measure V to determine the mode-matching efficiency by means the Eq. 3.28.

Through careful design of the experimental optical path lengths and lens arrangements, we can shape the signal and LO beams, to make sure that they are characterized by the same beam waists and wavefront curvatures when they interfere at BS. The OPO outcoming signal is collimated with the lens Ls (fs=100). Any residual divergence can be fine adjusted by changing the position of the Ls along the beam direction. The telescopic lens arrangements used for the LO beam is chosen in order to collimate it with the same waist radius of the signal beam at BS. It consist of the lenses L1 (f1=-100) and L2 (f2=200) that are placed in order to permit an adequate shape of the LO beam. Their overlapping at the BS is achieved by using two beam steering mirrors (M1 and M2 in Fig. 3.30) which drive the LO optical path. Through such technical tricks and using polarising optics, we could typically achieve visibilities in the range from 0.96 to 0.98.

The relative phase difference between the signal and the LO is controlled by varying the path length of one arm by small amounts using a piezo-electric-crystal (PZT) that lengthens and shrinks in response to an applied voltage. By attaching a mirror to this PZT we may actively control the length of the optical beam path of the LO. The maximum expansion achievable by a typical PZT is around $10\mu m$, which is several optical wavelengths and it is therefore sufficient for our purposes.

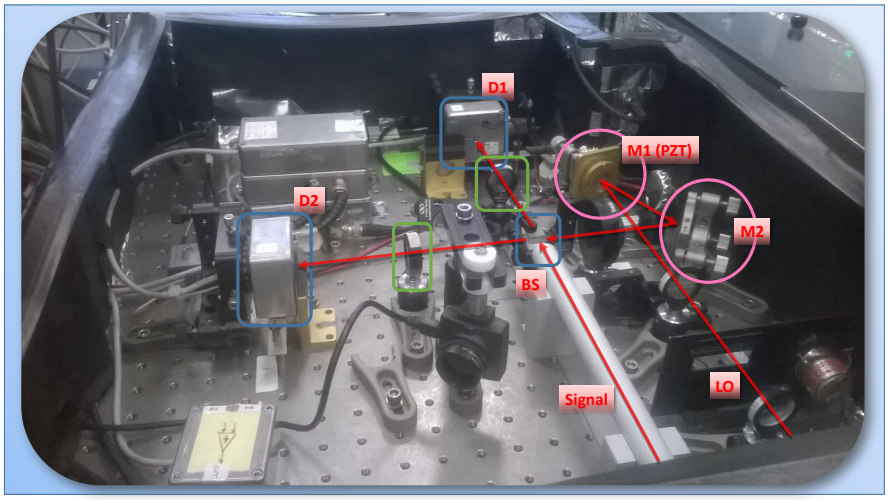

Figure 3.30: Photo of our homodyne detector in which the main elements are highlighted.

3.6 Propagation of squeezing

We have seen that the amount of observable squeezing is limited by the escape efficiency η_{esc} of the OPO cavity. It is defined as

$$\eta_{esc} = \gamma_{oc}/\gamma \tag{3.29}$$

where

$$\gamma = \gamma_{oc} + \gamma_{ic} + \gamma_i \Longrightarrow \textit{OPO total loss} \tag{3.30a}$$

$$\gamma_{oc} = \frac{1-R_{oc}}{2t_{rt}} \Longrightarrow \textit{OPO output coupler loss} \tag{3.30b}$$

$$\gamma_{ic} = \frac{1-R_{ic}}{2t_{rt}} \Longrightarrow \textit{OPO input coupler loss} \tag{3.30c}$$

$$\gamma_i = \frac{\Delta}{t_{rt}} \Longrightarrow \textit{OPO internal loss} \tag{3.30d}$$

where t_{rt} is the round trip time of the cavity and we have schematized the internal loss as a BS with reflectivity Δ, as we already seen in Sec. 2.3.1.

During my Ph.D work we have implemented two OPO cavities. In the first we have used an input coupler with R_{ic}=0.986 and thereby we have obtained $\eta_{esc} = 0.815$. The second OPO configuration is that already introduced and characterized by $\eta_{esc} = 0.924$.

In a complex experimental setup such as that described above the observed squeezing and anti-squeezing levels are further degraded by losses present in the transmission channels and detectors as shown in Sec 2.6. Therefore we have to include all the efficiencies of our apparatus and Eq. 2.40 becomes

$$\langle \Delta X_{\pm}^2 \rangle = 1 \pm \eta_{\text{tot}} \frac{4\sqrt{P/P_{\text{th}}}}{\left(1 \mp \sqrt{P/P_{\text{th}}}\right)^2 + 4\left(\frac{\Omega}{\gamma}\right)^2} \tag{3.31}$$

where we have explicitly written the dependence on pump power P, and, for sake of simplicity, we have put $\langle \Delta X_1^2 \rangle = \langle \Delta X_-^2 \rangle$ and $\langle \Delta X_2^2 \rangle = \langle \Delta X_+^2 \rangle$. $\Omega/\gamma = 0.13$ and η_{tot} is the total system efficiency which can be estimated by quantifying the individual contributions as follows:

$$\eta_{\rm tot} = \eta_{\rm DM}\,\eta_{\rm esc}\,\eta_{\rm HD}\,\eta_{\rm D}\,\eta_{\rm el}\,, \tag{3.32}$$

where $\eta_{\rm DM} = 0.96$ is the propagation efficiency of the optical path in the space between the OPO output coupler and the BS, the main amount of which comes from the measured dichroic mirror reflectivity (DM in Fig. 3.1), $\eta_{\rm D} = 0.97$ is the quantum efficiency of photodiodes corresponding to the manufacturer specifications and $\eta_{\rm el} = 0.98$ is the photodetectors' electronic noise. Finally, $\eta_{\rm HD}$ is the homodyne detection efficiency given by

$$\eta_{\rm HD} = \eta_{\rm Vis}\eta_{\rm BS} \tag{3.33}$$

where, as we have seen above, $\eta_{\rm Vis} \equiv \mathscr{V}^2$, takes into account of the degree of mode matching between OPO output mode and LO in BS. The best estimated visibility $\mathscr{V}$ is 0.98. Furthermore, we have $\eta_{\rm BS} = 0.999$, which depends on the not-ideal 50:50 splitting ratio of BS. The resulting quantum noise suppression below shot noise value is limited not only by losses but also by phase fluctuations between the OPO and the LO, which are caused by the imperfection of phase locking and mechanical vibrations [54]. In order to

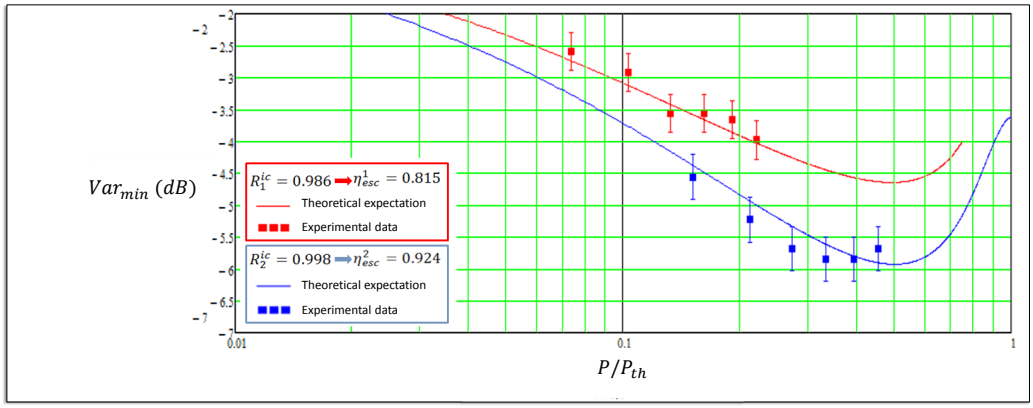

Figure 3.31: Comparison between the experimental data and the theoretical expectation in the two OPO configurations implemented in our laboratory: one with $\eta_{esc} = 0.815$ the other with $\eta_{esc} = 0.924$.

include this effect, we write the variance as

$$\langle \Delta X'^2 \rangle(\theta) = \langle \Delta X_-^2 \rangle \cos^2\theta + \langle \Delta X_+^2 \rangle \sin^2\theta \tag{3.34}$$

and assume that the phase fluctuations follow a Gaussian distribution $D(\phi,\sigma)$ where the standard deviation σ is estimated as 2.5 rad. The noise spectrum given by Eq. 3.31 is modified as

$$\langle \Delta X^2 \rangle(\theta) = \int D(\phi,\sigma)\langle \Delta X'^2 \rangle(\theta+\phi)\,d\phi \tag{3.35}$$

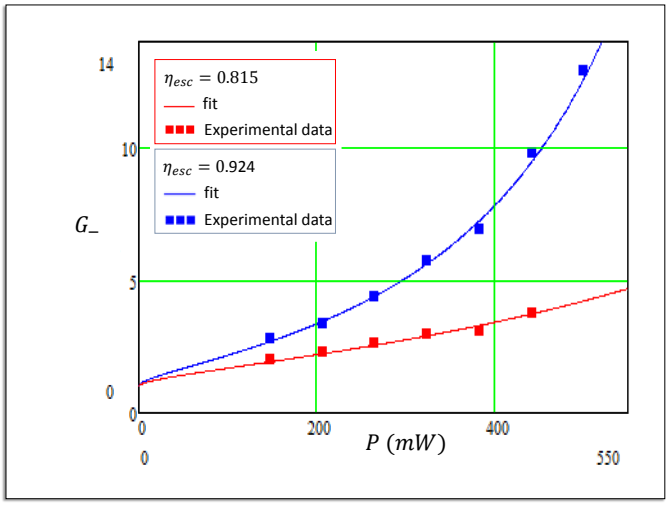

Figure 3.32: Measurements of the OPO regenerative gain G as functions of pump power P. By fitting the experimental data we obtain P_{th1}=1900 mW for the OPO configuration with $\eta_{esc} = 0.815$ and P_{th2}=970 mW for the OPO configuration with $\eta_{esc} = 0.924$

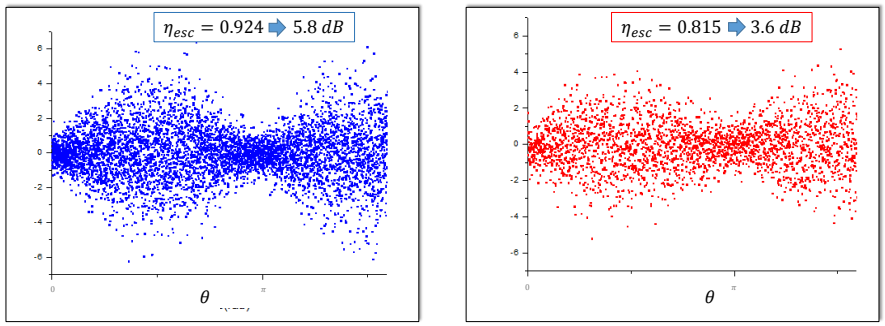

Figure 3.33: Homodyne traces of the vacuum squeezed state with OL power ∼10 mW and pump power ∼ 300 mW. On the left the acquisition performed with the OPO configuration characterized by η_{esc} = 0.924 is shown, on the right one with η_{esc} = 0.815. The measured squeezing levels are -5.8 dB and 3.6 dB, respectively, and are in agreement with the theoretical values.

in which $\langle \Delta X^2 \rangle (0)$ and $\langle \Delta X^2 \rangle \left(\frac{\pi}{2}\right)$ correspond to squeezing and anti-squeezing levels, respectively. Fig. 3.31 shows the comparison between the experimental data and the theoretical expectation in the two OPO configurations implemented in our laboratory: one with $\eta_{esc} = 0.815$ and the other with $\eta_{esc} = 0.924$, in which the OPO P_{th} are retrieved by fitting the measurements of the OPO regenerative gain G as a function of pump power P (see Fig. 3.32). We obtain P_{th1}=1900 mW for the OPO configuration with $\eta_{esc} = 0.815$ and P_{th2}=970 mW for the OPO configuration with $\eta_{esc} = 0.924$.

In Fig. 3.33 we show two examples of homodyne traces of the vacuum squeezed state: on the left we find an acquisition performed with the OPO configuration characterized

by η_{esc}=0.924, on the right one with η_{esc}=0.815.

3.7 The glass-integrated homodyne detector

Our apparatus is implemented with another homodyne acquisition scheme which exploits an integrated-optics device entirely fabricated by femtosecond laser micromachining. The device incorporates in the same chip both a balanced waveguide beam splitter and a thermo-optic phase shifter and we will refer to this device as *integrated homodyne analyzer* (IHA). In the last chapter we will investigate the output of the IHA in the presence of coherent and squeezed states and compare the results with those obtained via a standard homodyne detection (SHD) measurement based on a balanced cube beam splitter and a mechanical piezo movement (PZT) described above. Here we will focus on the feature of experimental setup sketched in 3.34.

3.7.1 The integrated homodyne analyzer (IHA)

In this section we describe the fabrication process and the main features of the IHA. It consists in a directional coupler, where two optical waveguides are brought close at few microns distance, so that they can exchange power by evanescent-field interaction, and a thermo-optic phase shifter. Waveguides are directly inscribed in EAGLE XG (Corning) glass substrate by femtosecond laser writing technology [11, 55]. To fabricate the waveguides, ultrashort pulses of about 300 fs duration, 240 nJ energy and 1 MHz repetition rate, from a Yb:KYW cavity-dumped femtosecond laser oscillator, are focused 30 μm beneath the surface of the substrate through a 0.6 NA microscope objective. Non-linear absorption processes of the ultrashort laser pulses generate a permanent refractive index increase, localized in the focal region. The translation of the sample under the laser beam at the constant speed of 20 mm/s allows to directly inscribe the waveguide along the desired path. The high precision translation is achieved by computer controlled air-bearing stages (Aerotech FiberGLIDE 3D). The waveguides support a single mode at 1064 nm wavelength (mode diameter $1/e^2$ is about 7 μm). The directional coupler is composed of two waveguides, starting at the relative distance of 125 μm, and brought close at the distance of 11 μm for a length of 300 μm. In such a region, the waveguides exchange power by evanescent field, and the interaction length is chosen to achieve a balanced splitting ratio. The bent segments have a curvature radius of 90 mm, which produces negligible additional bending losses. To fabricate the dynamic phase shifter, a 55 nm gold layer is sputtered on the top of the chip and a resistor is patterned, by femtosecond laser pulses, above one of the input waveguides of the directional coupler. This technique is described in more detail in Ref. [10]. The resistor is 100 μm wide and 5 mm long, for a value of resistance of about 100 Ω. Thermal dissipation on the resistor, when driven with a suitable current, creates temperature gradients in the glass, and thus thermo-optic modifications of the refractive indices in the waveguides. Therefore, a differential phase, directly proportional to the dissipated electrical power, can be imposed between the two input waveguides. In the homodyne measurements, the resistor is driven by a ramp generator (RG) to scan the LO phase.

3.7.2 Optical layout

In our experiments we aim at assessing the performance of the IHA, also in comparison with the SHD. To this purpose, we employed the apparatus sketched in Fig. 3.34, where the two homodyne detection configurations involving the SHD and the IHA can

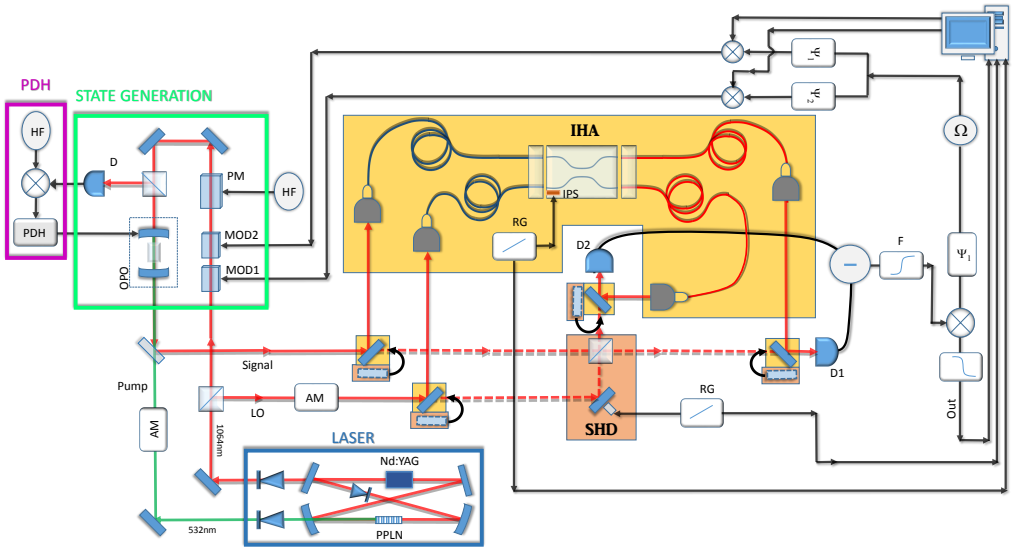

Figure 3.34: Once the state is generated, the OPO output beam can be directed onto either SHD or IHA by means of mirrors with high reflectivity at 1064 nm mounted on flippers. The homodyne detection system, indeed, is designed in such a way that we are able to pass from the configuration based on SHD to the configuration exploiting the IHA in a quickly and simply way. Therefore, an immediate comparison can be made between the measurements realized with both layouts. When the mirrors are flipped up, the signal is coupled to the IHA. In order to efficiently coupling the out coming signal from the OPO and the LO into and out of the waveguides, a pair of fiber arrays is used for the entry and exit interfaces of the IHA to inject and eject signal and LO beams efficiently. The LO phase is changed thanks to a thermal phase shifter (IPS). See the text for more details.

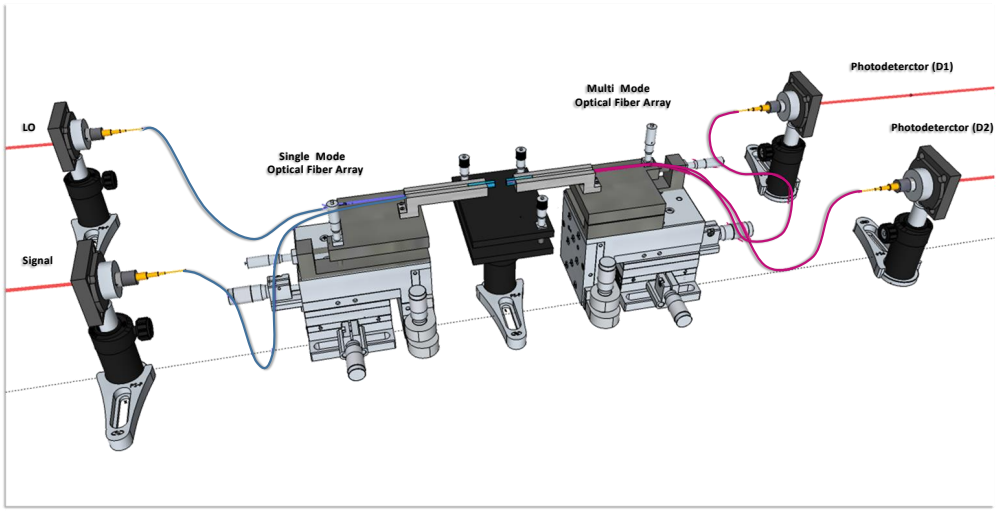

Figure 3.35: Pictorial zoom on the coupling system fibers-IHA. The fiber arrays-to-waveguide coupling efficiency is improved by aligning their position and orientation with a high degree of accuracy. For this purpose the two fiber arrays are separately mounted on two six-axis positioning stages with micron resolution. The alignment is a long and delicate iterative procedure but once the relative orientations between the components have been optimised, we have observed that the overall system remains stable.

be easily and quickly switched by means of flip mirrors. When the mirrors are flipped up, the set-up is switched to the IHA configuration. In order to efficiently couple the signal from the OPO and the LO to the inputs of the IHA we use a fiber arrays; a similar fiber arrays is used to couple the outputs of the IHA to the photodiodes, as pictorially shown in Fig. 3.34. Each fiber array contains two fibers, fastened with high precision at a distance of 125 μm by means of quartz V-groove blocks. The input fibers, which yield single-mode (SM) and polarization-maintaining operation, are Ferrule Connector/Physical Contact (FC/PC) connectorized. The signal and LO beams are coupled into them by means of adjustable FiberPort micropositioners. To improve the coupling efficiency, the built-in lenses of the latter components are chosen to ensure the optimal match between the incident modes and the fiber modes. The IHA is placed on an aluminium holder, to enhance heat dissipation, and the two fiber arrays can be aligned accurately to the waveguide inputs and outputs by means of two six-axis positioning stages with micrometric resolution as shown in Fig. 3.35. Index-matching gel is used to eliminate reflection losses at the fiber-waveguide interfaces. The fibers in the output fiber array are instead multimode (MM), with a core diameter of 50 μm and a cladding diameter of 125 μm, connectorized at the other ends with ferrule connector/angled physical contact (FC/APC) terminals, to reduce back reflections.

It is worth noting that a critical issue in this configuration is the minimization of the back reflections across the entire system. In fact, light back-propagating in the optical paths may distort the error signal of the PDH system, destroying the locking of the resonant frequency of the OPO cavity. To avoid this situation and ensure the efficient functioning of the active stabilization of the OPO, the use of such FC/APC fibers connectors was found to be crucial.

Light from the two FC/APC connectors is finally collected by lenses and focused on the low-noise photodetectors (D1, D2), which are shared between the two configurations.

In Chap. 6 we will show the measurements performed with this homodyne configuration. In particular we will demonstrate that our integrated device is able to detect the nonclassical features of the input signals.

Part II

Nonclassical states measurements

CHAPTER 4

Full quantum state reconstruction of symmetric two-mode squeezed thermal states via spectral homodyne detection and a state-balancing detector

In this Chapter we discuss the first implementation and characterization of the experimental system used throughout the work presented in this thesis. The results presented here has been published in the journal article. In particular, we suggest and demonstrate a scheme to reconstruct the symmetric two-mode squeezed thermal states of spectral sideband modes from an OPO.

4.1 Introduction

We have seen in previous sections that the interaction inside the OPO is bilinear and involves the sideband modes $a_{\pm\Omega}$. It is described by the effective Hamiltonian $H_\Omega \propto a^\dagger_{+\Omega}a^\dagger_{-\Omega} + \text{h.c.}$, that is a two-mode squeezing interaction (see Sec. 1.5.2). Due to the linearity of H_Ω, if the initial state is a coherent state or the vacuum, the generated two-mode state ρ_Ω is a Gaussian state and, thus, fully characterized by its covariance matrix (CM) $\boldsymbol{\sigma}_\Omega$ and first moment vector $\mathbf{R}$ as we have shown in Sec 1.5. It is worth noting that due to the symmetry of H_Ω, the two-sideband state is symmetric [56] and can be written as $\rho_\Omega = D_2(\alpha)S_2(\xi)\nu_{+\Omega}(N)\otimes\nu_{-\Omega}(N)S_2^\dagger(\xi)D_2^\dagger(\alpha)$, where $D_2(\alpha) = \exp\{[\alpha(a^\dagger_{+\Omega}+a^\dagger_{-\Omega}) - \text{h.c.}]/\sqrt{2}\}$ is the symmetric displacement operator and $S_2(\alpha) = \exp(\xi a^\dagger_{+\Omega}a^\dagger_{-\Omega} - \text{h.c.})$ the two mode squeezing operator and $\nu_{\pm\Omega}(N)$ is the thermal state of mode $a_{\pm\Omega}$ with N average photons, [14]. The state ρ_Ω belongs to the so-called class of the two-mode squeezed thermal states, generated by the application of $S_2^\dagger(\xi)D_2^\dagger(\alpha)$ to two thermal states with (in general) different energies. Here we suggest and demonstrate a measurement scheme for the quantum state reconstruction of these symmetric spectral modes based on a single homodyne detector and the PDH error signal used to stabilise the OPO which we have shown in Chap. 3. The experimental apparatus used in this project can be for the most part superposed on that already described. In this configuration however the seed to be injected into OPO cavity is generated by a phase modulator labelled PMb in Fig 4.1 and the OPO cavity has an escape efficiency η_{esc}=0.815. Therefore the squeezing level which we can observe is about 3 dB. In order to test our experimental setup, we acted on the OPO pump and on the phase modulation to generate and characterize three classes of states: the coherent ($\alpha \neq 0$ and $N, \xi = 0$), the squeezed ($\xi, N \neq 0$ and $\alpha = 0$) and the squeezed-coherent ($\alpha, \xi, N \neq 0$) two-mode sideband state. We have already talked about Homodyne detection. In short, the signal under investigation interferes at a balanced beam splitter with a local oscillator (LO) with frequency ω_0. The two outputs undergo a photodetection process and their photocurrents are are combined together thus leading to a photocurrent

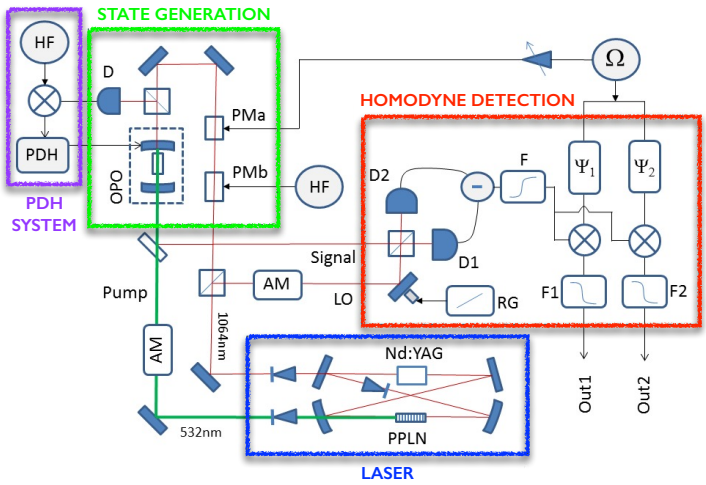

Figure 4.1: Schematic diagram of the experimental setup.

continuously varying in time. We recall here that, if $\tilde{a}_0(\omega_0)$ is the photon annihilation operator of the signal mode at the input of the HD, the detected photocurrent can be written as (note that the "fast term" ω_0 is canceled by the presence of the LO at the same frequency) $I(t) \propto \tilde{a}_0(t)\,\mathrm{e}^{-i\theta} + \tilde{a}_0^\dagger(t)\,\mathrm{e}^{i\theta}$, where θ is the phase difference between signal and LO and we introduced the time-dependent field operator $\tilde{a}_0(t)$, that is slowly varying with respect to the carrier at ω_0, such that $\tilde{a}_0(t) = \mathrm{e}^{-i\omega_0 t}\int d\omega\, F(\omega)\,\tilde{a}_0(\omega_0+\omega)\,\mathrm{e}^{-i\omega t} \equiv \mathrm{e}^{-i\omega_0 t} a_0(t)$, $F(\omega)$ being the apparatus spectral response function. To retrieve the information about the sidebands at frequencies $\omega_0 \pm \Omega$, described by the time-dependent field operators $a_{\pm\Omega}(t)$, we use an electronic setup consisting of a phase shifter (Ψ_1/Ψ_2) and a mixer ($\otimes$). After the mixer we have $I_\Omega(t,\Psi) = I(t)\cos(\Omega t + \Psi)$. Neglecting the terms proportional to $\exp(\pm 2i\Omega t)$ (low-pass filter F1/F2 @300 kHz) we find the following expression for the operator describing the (spectral) photocurrent $I_\Omega(t,\Psi) \propto X_\theta(t,\Psi|\Omega)$, where $X_\theta(t,\Psi|\Omega) = b(t,\Psi|\Omega)\,\mathrm{e}^{-i\theta} + b^\dagger(t,\Psi|\Omega)\,\mathrm{e}^{i\theta}$ is the quadrature operator associated with the field operator (note the dependence on the two sidebands):

$$b(t,\Psi|\Omega) = \frac{a_{+\Omega}(t)\,\mathrm{e}^{i\Psi} + a_{-\Omega}(t)\,\mathrm{e}^{-i\Psi}}{\sqrt{2}}. \tag{4.1}$$

Note that $\left[b(t,\Psi|\Omega), b^\dagger(t',\Psi|\Omega)\right] = \int d\omega\,|F(\omega)|^2\,\mathrm{e}^{-i\omega(t-t')}$.

We see that by changing the phase Ψ we can select different balanced combinations of the upper and lower sideband modes. In particular Ψ can be adjusted to select their symmetric $\mathscr{S}$ or antisymmetric $\mathscr{A}$ balanced combinations. For the sake of simplicity we implemented here a double electronic setup to observe the two outputs at the same time (Out1 and Out2 by setting Ψ_1 and Ψ_2 in fig. 4.1). The mode operators which correspond to the $\mathscr{S}$ and $\mathscr{A}$ combinations are:

$$b(t,0|\Omega) \equiv a_\mathrm{s}, \quad \text{and} \quad b(t,\pi/2|\Omega) \equiv a_\mathrm{a}, \tag{4.2}$$

respectively. We consider the corresponding quadrature operators $q_k = X_0(t,\Psi_k|\Omega)$, $p_k = X_{\pi/2}(t,\Psi_k|\Omega)$, and $z_k^\pm = X_{\pm\pi/4}(t,\Psi_k|\Omega)$, $k = \mathrm{a},\mathrm{s}$, with $\Psi_\mathrm{s} = 0$ and $\Psi_\mathrm{a} = \pi/2$. In the $\mathscr{S}/\mathscr{A}$ modal basis, the first moment vector of ρ_Ω reads $\boldsymbol{R}' = (\langle q_\mathrm{s}\rangle, \langle p_\mathrm{s}\rangle, \langle q_\mathrm{a}\rangle, \langle p_\mathrm{a}\rangle)^T$ and its 4×4

CM can be written in the following block-matrix form:

$$\boldsymbol{\sigma}' = \begin{pmatrix} \boldsymbol{\sigma}_{\rm s} & \boldsymbol{\sigma}_{\delta} \\ \boldsymbol{\sigma}_{\delta}^{T} & \boldsymbol{\sigma}_{\rm a} \end{pmatrix}, \quad \boldsymbol{\sigma}_{\delta} = \begin{pmatrix} \varepsilon_q & \delta_{qp} \\ \delta_{pq} & \varepsilon_p \end{pmatrix}, \tag{4.3}$$

where [57]:

$$\boldsymbol{\sigma}_k = \begin{pmatrix} \langle q_k^2\rangle - \langle q_k\rangle^2 & \frac{1}{2}\langle (z_k^+)^2 - (z_k^-)^2\rangle \\ \frac{1}{2}\langle (z_k^+)^2 - (z_k^-)^2\rangle & \langle p_k^2\rangle - \langle p_k\rangle^2 \end{pmatrix} \tag{4.4}$$

is the CM of the mode $k = {\rm a,s}$, $\varepsilon_l = \langle l_{\rm s} l_{\rm a}\rangle - \langle l_{\rm s}\rangle\langle l_{\rm a}\rangle$, $\delta_{l\bar{l}} = \langle l_{\rm s}\bar{l}_{\rm a}\rangle - \langle l_{\rm s}\rangle\langle \bar{l}_{\rm a}\rangle$ with $l, \bar{l} = q, p$ and $l \neq \bar{l}$. The matrix elements of $\boldsymbol{\sigma}_k$ can be directly measured from the homodyne traces of corresponding mode a_k. We now explicitly show how we can calculate them. From eq. 4.1

$$b(t, 0|\Omega) = \frac{\hat{a}_{+\Omega}(t) + \hat{a}_{-\Omega}(t)}{\sqrt{2}} \equiv a_{\rm s}, \tag{4.5a}$$

$$b(t, \pi/2|\Omega) = i\,\frac{\hat{a}_{+\Omega}(t) - \hat{a}_{-\Omega}(t)}{\sqrt{2}} \equiv a_{\rm a}, \tag{4.5b}$$

therefore the quadrature operator $X_\theta(t, \Psi|\Omega) = b(t, \Psi|\Omega)\,{\rm e}^{-i\theta} + b^\dagger(t, \Psi|\Omega)\,{\rm e}^{i\theta}$ can be written as:

$$X_\theta(t, \Psi|\Omega) = \cos\Psi\,[q_s\cos\theta + p_s\sin\theta] + \sin\Psi\,[q_a\cos\theta + p_a\sin\theta]\,. \tag{4.6}$$

If we set $\Psi = 0$, we have:

$$X_0(t, 0|\Omega) \equiv q_{\rm s} = a_{\rm s} + a_{\rm s}^\dagger = \frac{q_{+\Omega} + q_{-\Omega}}{\sqrt{2}} \Rightarrow \langle q_{\rm s}^2\rangle - \langle q_{\rm s}\rangle^2, \tag{4.7a}$$

$$X_{\pi/2}(t, 0|\Omega) \equiv p_{\rm s} = i(a_{\rm s}^\dagger - a_{\rm s}) = \frac{p_{+\Omega} + p_{-\Omega}}{\sqrt{2}} \Rightarrow \langle p_{\rm s}^2\rangle - \langle p_{\rm s}\rangle^2, \tag{4.7b}$$

$$X_{\pm\pi/4}(t, 0|\Omega) \equiv \frac{q_{\rm s} \pm p_{\rm s}}{\sqrt{2}} \Rightarrow \frac{1}{2}\langle q_{\rm s}p_{\rm s} + p_{\rm s}q_{\rm s}\rangle - \langle q_{\rm s}\rangle\langle p_{\rm s}\rangle, \tag{4.7c}$$

for $\Psi = \pi/2$ we obtain:

$$X_0(t, \pi/2|\Omega) \equiv q_{\rm a} = a_{\rm a} + a_{\rm a}^\dagger = \frac{p_{-\Omega} - p_{+\Omega}}{\sqrt{2}} \Rightarrow \langle q_{\rm a}^2\rangle - \langle q_{\rm a}\rangle^2, \tag{4.8a}$$

$$X_{\pi/2}(t, \pi/2|\Omega) \equiv p_{\rm a} = i(a_{\rm a}^\dagger - a_{\rm a}) = \frac{q_{+\Omega} - q_{-\Omega}}{\sqrt{2}} \Rightarrow \langle p_{\rm a}^2\rangle - \langle p_{\rm a}\rangle^2, \tag{4.8b}$$

$$X_{\pm\pi/4}(t, \pi/2|\Omega) \equiv \frac{q_{\rm a} \pm p_{\rm a}}{\sqrt{2}} \Rightarrow \frac{1}{2}\langle q_{\rm a}p_{\rm a} + p_{\rm a}q_{\rm a}\rangle - \langle q_{\rm a}\rangle\langle p_{\rm a}\rangle, \tag{4.8c}$$

Let us now consider the entries of $\boldsymbol{\sigma}_\delta$. The information about ε_l can be retrieved by changing the value of the mixer phase to $\Psi = \pm\pi/4$. In fact, it easy to show that [57, 58, 59] $\varepsilon_l = \frac{1}{2}\left(\langle l_+^2\rangle - \langle l_-^2\rangle\right) - \langle l_{\rm s}\rangle\langle l_{\rm a}\rangle$, $l = q, p$, where $q_\pm = X_0(t, \pm\pi/4|\Omega)$ and $p_\pm = X_{\pi/2}(t, \pm\pi/4|\Omega)$. Namely, if we set $\Psi = \pm\pi/4$ we find:

$$X_0(t, \pm\pi/4|\Omega) = \frac{q_{\rm a} \pm q_{\rm s}}{\sqrt{2}},$$

$$X_{\pi/2}(t, \pm\pi/4|\Omega) = \frac{p_{\rm s} \pm p_{\rm a}}{\sqrt{2}},$$

ad we have the following identities:

$$\langle X_0^2(t,\pi/4|\Omega) - X_0^2(t,-\pi/4|\Omega)\rangle = 2\langle q_a q_s\rangle \equiv \varepsilon_q, \tag{4.9}$$

$$\langle X_{\pi/2}^2(t,\pi/4|\Omega) - X_{\pi/2}^2(t,-\pi/4|\Omega)\rangle = 2\langle p_a p_s\rangle \equiv \varepsilon_p. \tag{4.10}$$

Let us now focus on $\delta_{l\bar{l}}$. It is not possible to calculate the elements δ_{qp} and δ_{pq} directly from the spectral homodyne traces [56]. To overcome this issue, a resonator detection method has been proposed and demonstrated in Refs. [56, 60]. Given the state ρ_Ω, but with different thermal contributions, these elements are equal to the energy unbalance between the sidebands (without the contribution due to the displacement that does not affect the CM), namely, $\delta_{qp} = -\delta_{pq} = \Delta N_\Omega = (N_{+\Omega} - N_{-\Omega})$, as shown in [61]. In our case we can exploit the error signal from the PDH stabilisation to check the symmetry of the sideband states and also to measure the presence of some energy unbalance of the two sidebands, leading to non-vanishing $\delta_{l\bar{l}}$. In our setup, indeed, the presence of the energy unbalance between the sidebands is due to the possible difference between the cavity transmission coefficients of the involved modes. Therefore, to determine the energy unbalance, we measure the normalized OPO cavity transmission coefficient when resonant with the pump, its bandwidth $\Delta\omega$ and get the corresponding analytical fit $T_0(\omega)$.

Then, we consider the error signal $E_{\rm PDH}(\delta x)$ of the PDH, where $\delta x = L - L_0$, L and L_0 being the actual cavity length and its length at resonance with the pump, respectively, see Fig. 4.2 (a). The detuning is thus given by $\delta\omega = -\omega_0\,\delta x/L_0$. If $|\delta\omega| \ll \Delta\omega$, that is our working regime, we can expand the error signal as $E_{\rm PDH}(\delta x) \approx \kappa\,\delta x$, where we used $E_{\rm PDH}(0) = 0$ and $\kappa = \partial_{\delta x} E_{\rm PDH}(0)$ is directly measured from the experimental PDH signal. At resonance, the cavity has a maximum of the (normalized) transmissivity at $\omega = 0$ (or $L = L_0$) and the corresponding PDH error signal vanishes, namely $E_{\rm PDH}(0) = 0$. This scenario is sketched in Fig. 4.2 (b), where we show a pictorial view of $T_0(\omega)$ when $E_{\rm PDH} = 0$: we have that $T_0 = 1$ and, thus, due to the symmetry of $T_0(\omega)$, we find $T_0(+\Omega) = T_0(-\Omega)$. In the presence of a detuning $|\delta\omega| \ll \Delta\omega$, we measure a PDH error signal $E_{\rm PDH}^{(\rm exp)} = E_{\rm PDH}(\delta x) \neq 0$, see Fig. 4.2 (c) (note that now the maximum of the transmissivity is reached at $\omega = \delta\omega$). Therefore, we can retrieve the actual value of detuning as $\delta\omega = -\omega_0 E_{\rm PDH}^{(\rm exp)}/(\kappa L_0)$ and use it to obtain the information about the (normalized) sideband transmission coefficients $T_{\delta\omega}(+\Omega)$ and $T_{\delta\omega}(-\Omega)$ starting from $T_{\delta\omega}(\omega) = T_0(\omega - \delta\omega)$. Eventually, we can assess the relative cavity transmission coefficients:

$$\tau_{\pm\Omega} = \frac{T_{\delta\omega}(\pm\Omega)}{T_{\delta\omega}(+\Omega) + T_{\delta\omega}(-\Omega)}, \tag{4.11}$$

associated with the two sideband modes, and the energy difference can be obtained as:

$$N_{+\Omega} - N_{-\Omega} = \frac{T_{\delta\omega}(+\Omega) - T_{\delta\omega}(-\Omega)}{T_{\delta\omega}(+\Omega) + T_{\delta\omega}(-\Omega)}\,(N_{+\Omega} + N_{-\Omega}). \tag{4.12}$$

In general, given the covariance matrix $\boldsymbol{\sigma}$ of a Gaussian state, the total energy can be obtained from the sum of its diagonal elements $[\boldsymbol{\sigma}]_{kk}$ as (without loss of generality we are still assuming the absence of the displacement):

$$N_{\rm tot} = \frac{1}{4}\sum_{k=1}^{4}[\boldsymbol{\sigma}]_{kk} - 1. \tag{4.13}$$

Experimentally, we can find the total energy $N_{+\Omega} + N_{-\Omega}$ from the first and second moments of the operators in Eqs. (4.7) and in Eqs. (4.8), which are measured from the homodyne detection.

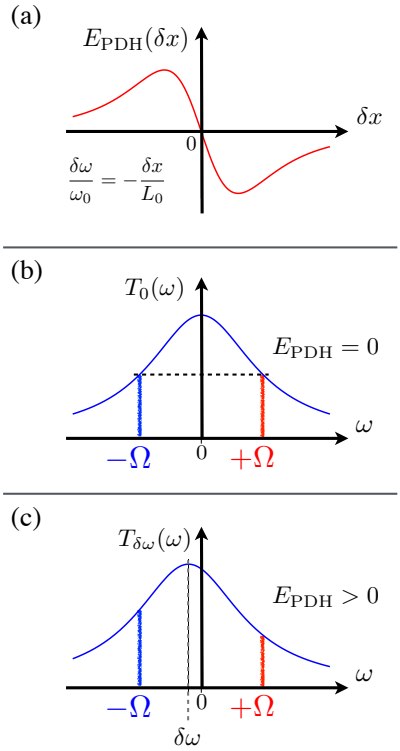

Figure 4.2: (a) PDH error signal as a function of the cavity displacement $\delta x = L - L_0$, where L is the cavity length and L_0 refers to the resonant condition with the pump at ω_0: the value of E_{PDH} allows to retrieve the information about the detuning $\delta\omega$. (b) Cavity transmission coefficient as a function of ω when $E_{\mathrm{PDH}} = 0$: one has the maximum $T_0(0) = 1$ and $T_0(+\Omega) = T_0(-\Omega)$. (b) Cavity transmission coefficient as a function of ω in the presence $E_{\mathrm{PDH}} \neq 0$ (in the plot we consider $E_{\mathrm{PDH}} > 0$): now one finds the transmissivity maximum at $\delta\omega$, namely, $T_{\delta\omega}(\delta\omega) = 1$. Note that $T_{\delta\omega}(\omega) = T_0(\omega - \delta\omega)$ and it is clear that $T_{\delta\omega}(+\Omega) \neq T_{\delta\omega}(-\Omega)$. Starting from the measured $E_{\mathrm{PDH}}(\delta x)$, one can retrieve the value $\delta\omega$ and, thereafter, the sideband transmission coefficients $T_{\delta\omega}(+\Omega)$ and $T_{\delta\omega}(-\Omega)$. For the sake of clarity we did not report the real experimental signals, but their pictorial view to better explain our analysis. See the text for details.

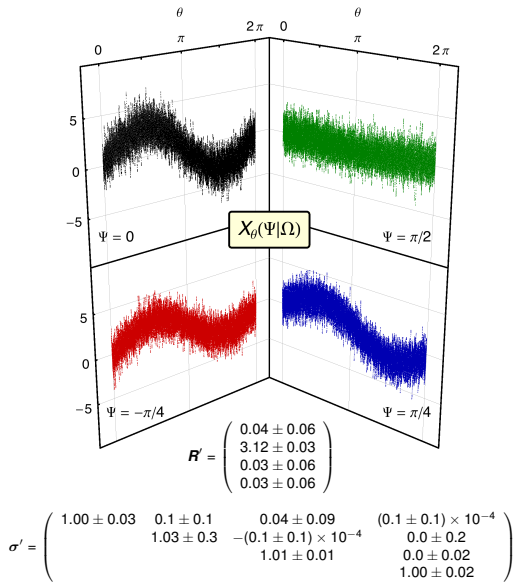

Figure 4.3: Homodyne traces referring to the coherent two-mode sideband state and the reconstructed $\boldsymbol{R}'$ and $\boldsymbol{\sigma}'$. The purities of the modes $\mathscr{S}$ and $\mathscr{A}$ are $\mu_s = 0.99^{+0.01}_{-0.02}$ and $\mu_a = 0.99^{+0.01}_{-0.01}$, respectively. Only the relevant elements are shown.

4.2 Experimental results

Once the mode has been selected by choosing the suitable mixer phase Ψ as shown above, the LO phase θ was scanned from 0 to 2π to acquire the corresponding homodyne trace. For the measurements shown in this paper we used a 2 GHz oscilloscope and collected about 100 000 points in the acquisition time of 20 ms. Figures 4.3, 4.4 and 4.5 show the experimental spectral homodyne traces corresponding to the coherent, squeezed and squeezed-coherent two-mode sideband states, respectively. The coherent state is generated by removing the OPO pump and sending to the PMa (see Fig. 4.1) a sinusoidal signal at 3 MHz with the proper voltage amplitude in order to generate the desired number of photons on the sidebands. In the case of the squeezed states, the OPO pump is set at ∼300 mW (well below the OPO threshold, which is about 4 times greater) whereas the input of the PMa seed generator is left in the vacuum (squeezed state) or modulated as in the case of the coherent state generation (squeezed-coherent state). As one can see, in the presence of squeezing (Figs. 4.4 and 4.5) all the four traces exhibit a phase-dependent quadrature variance; the dependence disappears when the coherent two-mode sideband state is considered (Fig. 4.3). In this last case we can also see that for $\Psi = \pi/2$ the homodyne trace is that of the vacuum state, as one may expect.

The statistical analysis of each trace allows to reconstruct the expectation value of the moments of the quadrature required to reconstruct the CM $\boldsymbol{\sigma}'$ and the first moments vector $\mathbf{R}'$, which are reported in the same figures. All the reconstructed $\boldsymbol{\sigma}'$ satisfy the physical condition $\boldsymbol{\sigma}' + i\boldsymbol{\Omega} \geq 0$ where $\boldsymbol{\Omega} = i\boldsymbol{\sigma}_y \oplus \boldsymbol{\sigma}_y$, $\boldsymbol{\sigma}_y$ being the Pauli matrix [14]. This implies that the modes $\mathscr{S}$ and $\mathscr{A}$ represent the same local quantum state, namely, $\boldsymbol{\sigma}_s = \boldsymbol{\sigma}_a$: this is in agreement with our measurement within statistical errors, as one can check

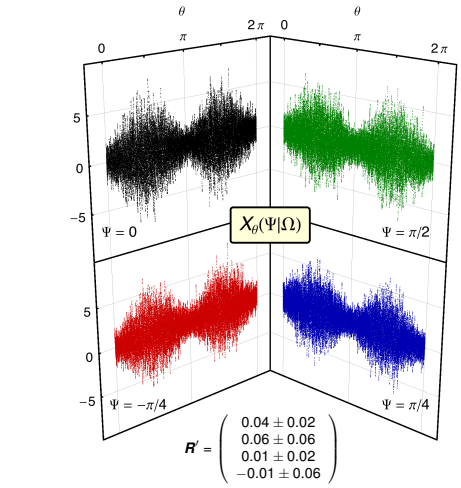

Figure 4.4: Homodyne traces referring to the squeezed two-mode sideband state and the reconstructed $\boldsymbol{R}'$ and $\boldsymbol{\sigma}'$. The noise reduction is 3.1 ± 0.3 dB for both the modes $\mathscr{S}$ and $\mathscr{A}$, wheres their purities are $\mu_{\mathrm{s}} = 0.68 \pm 0.07$ and $\mu_{\mathrm{a}} = 0.67 \pm 0.02$, respectively. Only the relevant elements are shown.

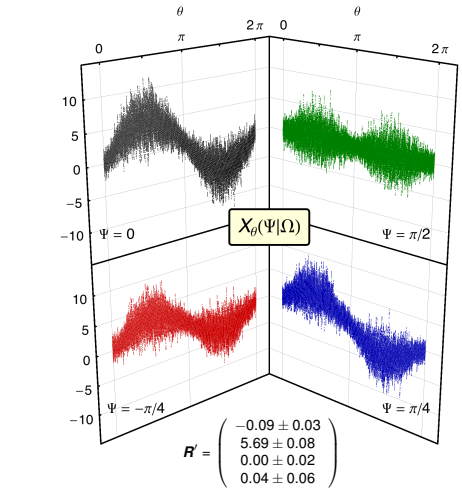

Figure 4.5: Homodyne traces referring to the squeezed-coherent two-mode sideband state and the reconstructed $\boldsymbol{R}'$ and $\boldsymbol{\sigma}'$. The noise reduction is 2.7 ± 0.3 dB for the $\mathscr{A}$ mode and 2.4 ± 0.2 dB for the $\mathscr{S}$ mode, whereas the purities are $\mu_{\mathrm{s}} = 0.68 \pm 0.07$ and $\mu_{\mathrm{a}} = 0.64 \pm 0.02$, respectively. Only the relevant elements are shown.

• *Two-mode coherent state:*

$$R = (0.05 \pm 0.06,\ 2.18 \pm 0.05,\ 0.01 \pm 0.06,\ 2.23 \pm 0.05)^{\mathrm{T}}$$

$$\sigma_\Omega = \begin{pmatrix} 1.00 \pm 0.02 & 0.0 \pm 0.1 & 0.00 \pm 0.02 & 0.1 \pm 0.1 \\ 0.0 \pm 0.1 & 1.02 \pm 0.02 & 0.0 \pm 0.1 & 0.01 \pm 0.02 \\ 0.00 \pm 0.02 & 0.0 \pm 0.1 & 1.00 \pm 0.02 & 0.0 \pm 0.1 \\ 0.1 \pm 0.1 & 0.01 \pm 0.02 & 0.0 \pm 0.1 & 1.02 \pm 0.02 \end{pmatrix}$$

• *Two-mode squeezed state:*

$$R = (0.02 \pm 0.04,\ 0.03 \pm 0.04,\ 0.03 \pm 0.04,\ 0.05 \pm 0.04)^{\mathrm{T}}$$

$$\sigma_\Omega = \begin{pmatrix} 2.3 \pm 0.1 & 0.00 \pm 0.06 & -1.8 \pm 0.1 & 0.05 \pm 0.06 \\ 0.00 \pm 0.06 & 2.3 \pm 0.1 & 0.01 \pm 0.06 & 1.8 \pm 0.1 \\ -1.8 \pm 0.1 & 0.01 \pm 0.06 & 2.3 \pm 0.1 & 0.00 \pm 0.06 \\ 0.05 \pm 0.06 & 1.8 \pm 0.1 & 0.00 \pm 0.06 & 2.3 \pm 0.1 \end{pmatrix}$$

• *Two-mode squeezed-coherent state:*

$$R = (-0.09 \pm 0.05,\ 4.02 \pm 0.06,\ -0.03 \pm 0.05,\ 4.02 \pm 0.06)^{\mathrm{T}}$$

$$\sigma_\Omega = \begin{pmatrix} 2.4 \pm 0.1 & 0.1 \pm 0.2 & -1.8 \pm 0.1 & 0.0 \pm 0.2 \\ 0.1 \pm 0.2 & 2.3 \pm 0.1 & -0.2 \pm 0.2 & 1.8 \pm 0.1 \\ -1.8 \pm 0.1 & -0.2 \pm 0.2 & 2.4 \pm 0.1 & -0.1 \pm 0.2 \\ 0.0 \pm 0.2 & 1.8 \pm 0.1 & -0.1 \pm 0.2 & 2.3 \pm 0.1 \end{pmatrix}$$

Table 4.1: Reconstructed first moment vectors $\boldsymbol{R}$ and CMs $\boldsymbol{\sigma}_\Omega$ of the two-mode sideband states ρ_Ω corresponding to the states of Figs. 4.3, 4.4 and 4.5, respectively.

from Figs. 4.3, 4.4 and 4.5. Furthermore, the diagonal elements of the off-diagonal blocks are zero within their statistical errors, in agreement with the expectation for a factorized state of the two modes.

We should now calculate the corresponding CMs in the modal basis $\hat{a}_{+\Omega}$ and $\hat{a}_{-\Omega}$ of the upper and lower sideband, respectively. Because of Eqs. (4.2) we can write $\boldsymbol{\sigma}_\Omega = \boldsymbol{S}^T \boldsymbol{\sigma}' \boldsymbol{S}$ and $\boldsymbol{R} = \boldsymbol{S}^T \boldsymbol{R}'$, where

$$\boldsymbol{S} = \frac{1}{\sqrt{2}} \begin{pmatrix} \mathbb{I} & \mathbb{I} \\ -i\boldsymbol{\sigma}_y & i\boldsymbol{\sigma}_y \end{pmatrix} \tag{4.14}$$

is the symplectic transformation associated with the mode transformations of Eqs. (4.2). The results are summarized in Table 4.1. Whereas the reconstructed two-mode sideband coherent state is indeed a product of two coherent states, the other two reconstructed states exhibit non-classical features. In particular, the minimum symplectic eigenvalues of the corresponding partially transposed CMs [62, 63] read $\tilde{\lambda} = 0.50 \pm 0.02$ and $\tilde{\lambda} = 0.55 \pm 0.03$ for the two-mode squeezed and squeezed-coherent state, respectively: since in both the cases $\tilde{\lambda} < 1$, we conclude that the sideband modes are entangled [1]

4.3 Concluding remarks

In conclusion, we have presented a measurement scheme to fully reconstruct the class of symmetric two-mode squeezed thermal states of spectral sideband modes from an optical parametric oscillator. This class of states, with Gaussian Wigner functions, is widely

[1] In the references cited the criterion is defined as $\tilde{\lambda} < 1/2$. Here, all the traces are normalized to the shot noise level of a pure vacuum field which is then set at one. Therefore such criterion read as $\tilde{\lambda} < 1$.

exploited in continuous-variable quantum technology. The scheme is based on homodyne detection and active stabilization, which guarantees phase coherence in every step of the experiment, and on a suitable analysis of the detected photocurrents. We have shown that by properly choosing the electronic mixer phase it is possible to select four different combinations of the upper and lower sideband which, together with the information from the PDH error signal, allows to reconstruct the elements of the covariance matrix of the state under consideration. The scheme has been successfully demonstrated to reconstruct both factorized and entangled sideband states.

In our implementation we have used two electronic mixers and retrieved information about two modes at a time. It is also possible to use four mixers and extract information about the four modes at the same time. The method is based on a single homodyne detector, the error signal from the active stabilization of the OPO and does not involve elements outside the main detection tools of continuous variable optical systems. As such, our procedure is indeed a versatile diagnostic tool, suitable to be embedded in quantum information experiments with continuous-variable systems in the spectral domain, where, in particular, a state from an OPO is used as a signal or a quantum probe and, therefore, should be fully characterized.

CHAPTER 5

Quantum-to-classical transition for squeezed thermal states (STS) of a single-mode optical system

In this chapter we show how the generation/acquisition states system implemented during my Ph.D studies has been used to observe and analyse quantum to classical transitions for squeezed thermal states (STS) of a single-mode optical system.

5.1 Introduction

The engineering of the nonclassical states generation and detection processes which we have developed during my Ph.D. has found its first concrete application in the study of the quantum-to-classical transition for squeezed thermal states (STS) of a single-mode optical system. Our findings have been exploited for analysing in details the significance of fidelity as a figure of merit in quantum state reconstruction of continuous-variable (CV) quantum optical systems. The result achieved has been published in the paper:

- A. Mandarino, M. Bina, C. Porto, S. Cialdi, S. Olivares, and M. G. A. Paris. *Assessing the significance of fidelity as a figure of merit in quantum state reconstruction of discrete and continuous-variable systems.* Physical Review A **93**, 062118 (2016)

In this Chapter we want to stress the experimental aspects of this work, whereas we refer you to the paper [64] for the theoretical analysis of the fidelity. Here we limit ourself to merely stating the conclusions of the theoretical developments. For the sake of completeness, anyway, the fidelity concept should be introduced. In quantum technology, it is commonly used to summarize the results of a reconstruction technique, either full quantum tomography [65, 66, 67, 68, 69, 70, 71] or some partial reconstruction scheme [72, 73, 74, 75, 76, 77]. The fidelity between two quantum states described by density matrices $\hat{\rho}_1$ and $\hat{\rho}_2$ is defined as [78]

$$F(\hat{\rho}_1,\hat{\rho}_2) = \mathrm{Tr}\left[\sqrt{\sqrt{\hat{\rho}_1}\hat{\rho}_2\sqrt{\hat{\rho}_1}}\right]^2 . \tag{5.1}$$

Fidelity is not a proper distance in the Hilbert space. However, it can be easily linked to a distance, and in turn to a metric over the manifold of density matrices. In fact, the Bures distance [79] between two states is defined as

$$D_B(\hat{\rho}_1,\hat{\rho}_2) = \sqrt{2[1-\sqrt{F(\hat{\rho}_1,\hat{\rho}_2)}]}\,.$$

Fidelity also provides an upper and a lower bound to the trace distance, namely [80]:

$$1-\sqrt{F(\hat{\rho}_1,\hat{\rho}_2)} \leq \frac{1}{2}||\hat{\rho}_1-\hat{\rho}_2||_1 \leq \sqrt{1-F(\hat{\rho}_1,\hat{\rho}_2)}\,.$$

These relationships ensure that higher values of fidelity correspond to the geometrical proximity of the two states in the Hilbert space. However, they do not seem straightforwardly related to the physical properties of the two states. In turn, it has been pointed out [81, 82, 83, 84] that a pair of states that appear very close to each other in terms of fidelity, may be very far in terms of physical resources. Relevant examples may be found with bipartite systems of either qubits or CV Gaussian states, where pairs of states composed by one entangled and one separable states may have (very) high value of fidelity one to each other. Besides, for single-mode CV states, high values of fidelity may be achieved by pairs including one state with a classical analogue and a genuinely quantum state of the field. In order to experimentally study this second case, we need to find a method to switch from a classical to a quantum framework in a controlled way. On the other hand, the OPO seeding is a crucial step to observe the quantum-to-classical transition with STS. As a matter of fact, without seeding the OPO, the output signal is a squeezed vacuum state, which is then degraded to a STS with a nonzero thermal component by propagation in a lossy channel as we have already seen. However, STS obtained in this way are always nonclassical for any value of the loss and the squeezing parameters [14, 85, 86]. For this reason, the STS generation technique shown in Sec. 3.3 has been developed.

5.2 Single-mode Gaussian states

Our goal is to study a single-mode STS and therefore we have to generate a thermal seed to be injected into the OPO. We have seen the experimental strategy exploited for generating and detecting this kind of states (see Sec. 3.3. We recall here that the density matrix of a thermal state in the Glauber representation reads as follows

$$\hat{\nu}_{\mathrm{OPO}}(\tilde{n}_{\mathrm{th}}) = \int_0^\infty d|\alpha| \frac{2|\alpha|}{\tilde{n}_{\mathrm{th}}} e^{-\frac{|\alpha|^2}{\tilde{n}_{\mathrm{th}}}} \int_0^{2\pi} \frac{d\phi}{2\pi} ||\alpha| e^{i\phi}\rangle\langle |\alpha| e^{i\phi}| \,, \tag{5.2}$$

i.e., it can be viewed as a mixture of coherent states with phase ϕ uniformly distributed over the range 0 to 2π, and a given amplitude $|\alpha|$ distribution. Therefore, we have to generate a rapid sequence of coherent states with $|\alpha|$ and ϕ randomly selected from these distributions.

The STS of a single-mode radiation field are states of the form

$$\hat{\rho} = \hat{S}(r)\hat{\nu}(n_{\mathrm{th}})\hat{S}^\dagger(r) \,, \tag{5.3}$$

where $\hat{S}(r) = \exp\left\{\frac{1}{2} r\left[(\hat{a}^\dagger)^2 - \hat{a}^2\right]\right\}$ is the squeezing operator, with $r \in \mathbb{R}$, $\hat{\nu}(n_{\mathrm{th}}) = n_{\mathrm{th}}^{\hat{a}^\dagger \hat{a}}/(1+n_{\mathrm{th}})^{\hat{a}^\dagger \hat{a}+1}$ is a thermal state with n_{th} average number of photons and $[\hat{a}, \hat{a}^\dagger] = 1$, $\hat{a}$ and $\hat{a}^\dagger$ being field operators. Upon defining the quadrature operators

$$\hat{x}_\theta \equiv \hat{a}\, \mathrm{e}^{-i\theta} + \hat{a}^\dagger \mathrm{e}^{i\theta} \,, \tag{5.4}$$

with $\theta \in [0, \pi]$, the STS are fully characterized by their first and second moments

$$\langle \hat{x}_\theta \rangle = 0 \qquad \forall \theta \tag{5.5a}$$

$$\langle \Delta \hat{x}_\theta^2 \rangle = (1 + 2n_{\mathrm{th}})(\mathrm{e}^{2r} \cos^2\theta + \mathrm{e}^{-2r} \sin^2\theta) \,, \tag{5.5b}$$

where $\langle \cdots \rangle \equiv \mathrm{Tr}[\hat{\rho} \cdots]$. In terms of the canonical operators $\hat{x} \equiv \hat{x}_0$ and $\hat{p} \equiv \hat{x}_{\pi/2}$, the covariance matrix (CM) of a STS reads

$$\sigma = \begin{pmatrix} \langle \Delta \hat{x}^2 \rangle & 0 \\ 0 & \langle \Delta \hat{p}^2 \rangle \end{pmatrix} = \begin{pmatrix} s/\mu & 0 \\ 0 & 1/\mu s \end{pmatrix}, \tag{5.6}$$

where $\mu = \mathrm{Tr}[\hat{\rho}^2] = (2n_{\mathrm{th}}+1)^{-1}$ is the purity of the state $\hat{\rho}$ and $s \equiv \mathrm{e}^{2r}$ is the squeezing factor. A STS is nonclassical, i.e. it corresponds to a singular Glauber P-function, whenever the conditions $s < \mu$ or $s > \mu^{-1}$ are satisfied. The total energy of a STS is given by

$$N_{\mathrm{tot}} = \langle \hat{a}^\dagger \hat{a} \rangle = n_{\mathrm{th}} + n_{\mathrm{s}} + 2n_{\mathrm{th}} n_{\mathrm{s}} \quad , \tag{5.7}$$

where $n_s = \sinh^2 r$ is the number of squeezing photons and n_{th} is the thermal contribution to energy. It is worth noting that the number of thermal photons n_{th} does not coincide with the parameter $\tilde{n}_{\mathrm{th}}$ in Eq. 5.2, as the former accounts for both the seeding and any losses from the OPO to the detector, whereas the latter is related to the thermal seeding of the OPO.

According to Eq. (5.7), it is possible to find a suitable parametrization of the single-mode STS CM (5.6) in terms of the different energy contributions

$$\langle \Delta\hat{x}^2 \rangle = \left(1 + 2\frac{N_{\mathrm{tot}} - n_{\mathrm{s}}}{2n_{\mathrm{s}}+1}\right)(1 + 2n_s - 2\sqrt{n_{\mathrm{s}} + n_{\mathrm{s}}^2}) \tag{5.8a}$$

$$\langle \Delta\hat{p}^2 \rangle = \left(1 + 2\frac{N_{\mathrm{tot}} - n_{\mathrm{s}}}{2n_{\mathrm{s}}+1}\right)\frac{1}{(1 + 2n_{\mathrm{s}} - 2\sqrt{n_{\mathrm{s}} + n_{\mathrm{s}}^2})}, \tag{5.8b}$$

from which the linear behavior of the variances as a function of the total energy N_{tot} is evident.

The fidelity between two STS is given by [87]

$$F(\sigma_1, \sigma_2) = \frac{1}{\sqrt{\Delta + \delta} - \sqrt{\delta}}, \tag{5.9}$$

where $\Delta = \frac{1}{4}\det[\sigma_1 + \sigma_2]$ and $\delta = \frac{1}{4}\prod_{i=1,2}(\det\sigma_i - 1)$.

5.3 Homodyne tomography

We perform state reconstruction of these single-mode CV systems by quantum homodyne tomography, i.e. by collecting homodyne data at different LO phases θ_k. Generation and acquisition operations are synchronized in the same time window of 70 ms at the same sampling rate of 100 kHz. Therefore we collect 7000 homodyne data points $\{(\theta_k, x_k)\}$, by scanning the LO with $\theta_k \in [0, 2\pi]$. We address the quantum-to-classical transition by generating $m = 14$ STS with increasing thermal component, as the squeezing is fixed by the geometry of the experimental setup.

These measurements are analysed by applying the pattern functions method whereby we reconstruct the first-moment vector and the CM, as well as the total energy $\hat{a}^\dagger\hat{a}$ of the state using the estimators in Eq.1.74. We characterized these states in terms of the position $\langle \Delta\hat{x}^2 \rangle$ and momentum $\langle \Delta\hat{p}^2 \rangle$ variances and the total energy $N_{\mathrm{tot}} \equiv \langle \hat{a}^\dagger\hat{a} \rangle$. From the measured quadrature variances, the experimental squeezing factor $s_{\mathrm{exp}} = [\langle \Delta\hat{x}^2 \rangle / \langle \Delta\hat{p}^2 \rangle]^{1/2}$ and purity $\mu_{\mathrm{exp}} = [\langle \Delta\hat{x}^2 \rangle \langle \Delta\hat{p}^2 \rangle]^{-1/2}$ are obtained. These results are reported in Table 5.1.

Moreover for all the detected states, we tested the compatibility with the typical form of the STS, i. e. null first-moment vector (5.5a) and diagonal CM (5.6). The shot-noise threshold is set at $\langle \Delta\hat{x}^2 \rangle = \langle \Delta\hat{p}^2 \rangle = 1$, under which the state of the detected single-mode radiation displays genuine quantum squeezing. The generated STS display squeezing in position quadrature and anti-squeezing in momentum quadrature (i.e. we have real and negative squeezing parameter $r < 0$). In Fig. 5.1 we show the position and momentum variances as a function of the total energy for the $m = 14$ experimentally generated STS. A

Table 5.1: Characterization, via homodyne tomography, of the $m = 14$ experimental STS in terms of the position and momentum variances, total energy, squeezing factor and purity. The STS display squeezing in position and anti-squeezing in momentum coordinates ($r < 0$) .

state #	$\langle \Delta\hat{x}^2 \rangle$	$\langle \Delta\hat{p}^2 \rangle$	$\langle \hat{a}^\dagger \hat{a} \rangle$	$s_{\rm exp}$	$\mu_{\rm exp}$
1	0.48 ± 0.03	3.15 ± 0.09	0.41 ± 0.02	0.39 ± 0.01	0.81 ± 0.03
2	0.67 ± 0.04	3.33 ± 0.09	0.50 ± 0.02	0.45 ± 0.01	0.67 ± 0.02
3	0.62 ± 0.04	3.77 ± 0.11	0.60 ± 0.02	0.40 ± 0.02	0.66 ± 0.02
4	0.69 ± 0.05	3.94 ± 0.11	0.66 ± 0.02	0.41 ± 0.02	0.61 ± 0.02
5	0.70 ± 0.05	4.51 ± 0.12	0.80 ± 0.03	0.39 ± 0.02	0.56 ± 0.02
6	0.77 ± 0.05	4.54 ± 0.13	0.83 ± 0.03	0.41 ± 0.02	0.54 ± 0.02
7	0.77 ± 0.05	4.60 ± 0.13	0.84 ± 0.03	0.41 ± 0.02	0.53 ± 0.02
8	0.93 ± 0.06	5.00 ± 0.14	0.98 ± 0.03	0.43 ± 0.02	0.46 ± 0.02
9	0.95 ± 0.06	5.36 ± 0.15	1.08 ± 0.03	0.42 ± 0.01	0.44 ± 0.02
10	0.93 ± 0.07	5.56 ± 0.15	1.12 ± 0.03	0.41 ± 0.02	0.44 ± 0.02
11	1.00 ± 0.07	5.80 ± 0.17	1.20 ± 0.03	0.42 ± 0.02	0.42 ± 0.02
12	1.13 ± 0.07	5.87 ± 0.16	1.25 ± 0.03	0.44 ± 0.02	0.39 ± 0.01
13	1.11 ± 0.08	6.33 ± 0.18	1.36 ± 0.04	0.42 ± 0.02	0.38 ± 0.01
14	1.30 ± 0.08	6.16 ± 0.18	1.36 ± 0.04	0.46 ± 0.02	0.35 ± 0.01

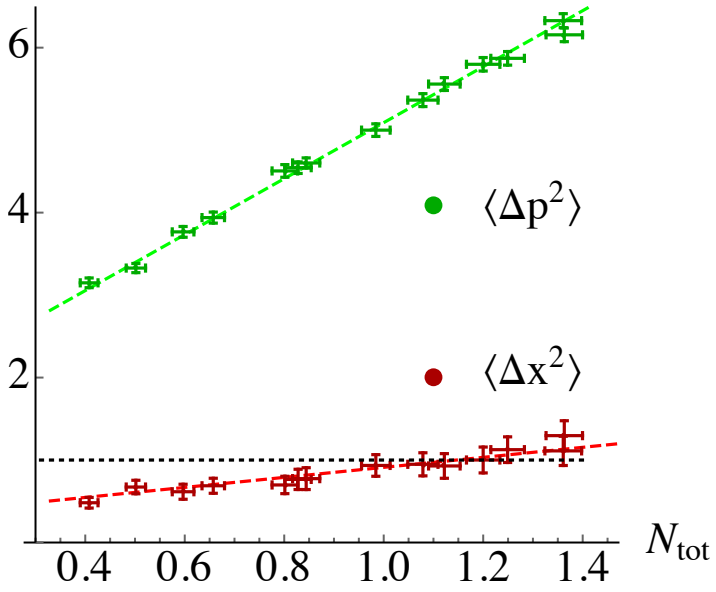

Figure 5.1: Tomographic reconstruction of the variances of the squeezed quadrature $\hat{x}$ (red lower dots) and of the anti-squeezed quadrature $\hat{p}$ (green upper dots) as a function of the total energy $N_{\rm tot}$, for $m = 14$ experimental STS. Dashed lines represent linear fits of the experimental data (see Eqs. (5.8)), from which we obtain the number of squeezed photons $n_{\rm s} \simeq 0.2$. The black dotted horizontal line is the shot-noise level at $\langle \Delta\hat{x}^2 \rangle = \langle \Delta\hat{p}^2 \rangle = 1$.

linear fitting, following Eq. (5.8), provides the value of the number of squeezed photons $n_s \simeq 0.2$, which corresponds to ~ 3.7 dB of squeezing. Fig. 5.1 makes apparent the capability of the experimental setup to generate STS-on-demand by seeding the OPO with a controlled number of thermal photons and in turn, to monitor the quantum-to-classical transition of a single-mode Gaussian state of light.

Once the information about the state of a system has been extracted from a set of experimental data, the fidelity between the reconstructed state and a given target state, is calculated [88, 89, 90, 91].

From an accurate theoretical development (details of which can be read in our paper [64]), we found that neighbouring states in terms of fidelity (i.e. states characterized by high values of fidelity) do not share the same quantum/classical properties.

5.4 Conclusions

In order to study the quantum-to-classical transition for STS of a single-mode optical system, it is necessary to seed the OPO in a controlled fashion. Our experimental setup allows this issue thanks to the system described in 3.3.1 whereby we can choose and set the STS photon number on demand. By generating STSs with the photon number increasing values, the quantum-to-classical transition has been observed.

This result has been exploit to study the significance of fidelity as a figure of merit in quantum state reconstruction.High values of fidelity such as 0.9 or 0.99 are considered as a piece of evidence in order to certify that the reconstructed and the target states i) are very close each other in the Hilbert space, ii) they share nearly identical physical properties. In our paper [64] we have experimentally confirmed the first statement and, at the same time, we have provided neat examples where the second one is clearly proved wrong. Overall, we have concluded that while fidelity is a good measure of geometrical proximity in the Hilbert space it should not be used as the sole benchmark to certify quantum properties [92, 93, 94, 95, 96], which should be rather estimated tomographycally in a direct way, or using a suitable witness operator [65, 68].

In this thesis framework, we want to highlight that the accurate control of the thermal and squeezing component of the apparatus, allows us to address the quantum-to-classical transition for STS states.

CHAPTER 6

Squeezing detection by using an glass-integrated homodyne analyzer

In this chapter we will show the measurements performed by exploiting the glass-integrated homodyne analyzer (IHA) which we have described in Sec. 3.7. We will analyse the homodyne traces of squeezed vacuum and coherent states. The comparison with those realized with the standard homodyne detector will show the IHA effect on squeezing.

6.1 Introduction

Experiments involving non-classical states of light need highly complex optical circuits through which optical beams propagate. This means the use of a lot of mirrors, beam splitters and lenses. This kind of experimental setup in bulk optics encounters severe limitations, in particular concerning the optical phase stability and control, which is a crucial requirement for the manipulation of squeezed states. This makes the adoption of a monolithic integrated platform highly beneficial. Actually, while integrated quantum photonics has recently boosted many experimental demonstrations based on discrete-variable systems [97, 98, 99, 100], few on-chip experiments have been reported to date with continuous variable systems. Masada et al. demonstrated fundamental operations for the manipulation of squeezed light states within a reconfigurable silica-on-silicon chip [101]; however, an external piezo-electric controller was used in that case to vary the local-oscillator phase in the homodyne measurement. Very recently, the integration on the same chip of a beam splitter and balanced detectors of the homodyne apparatus was reported, to perform quantum random number generation [102], but no active modulation was operated on the phase of the local oscillator in the experiment. A few waveguide-based sources of squeezed light states have been also demonstrated [103, 104] and first steps are moving towards a fully guided-wave based architecture exploiting squeezed light [105].

In line with these, here we report on homodyne measurements performed via our integrated homodyne analyser (IHA) which we have introduced in Sec. 3.7. More in detail, we investigate the output of the IHA in the presence of coherent and squeezed states and compare the results with those obtained via the standard homodyne detection measurement (SHD).

6.2 Squeezed vacuum states

As a first experiment, we characterize a squeezed vacuum state, generated by the OPO. Figure 6.1 shows the experimental spectral homodyne traces achieved by collecting M=7000 data points in a time window of 800 ms with a repetition rate of 10 kHz, $\{(x_k, \theta_k)\}$, x_k

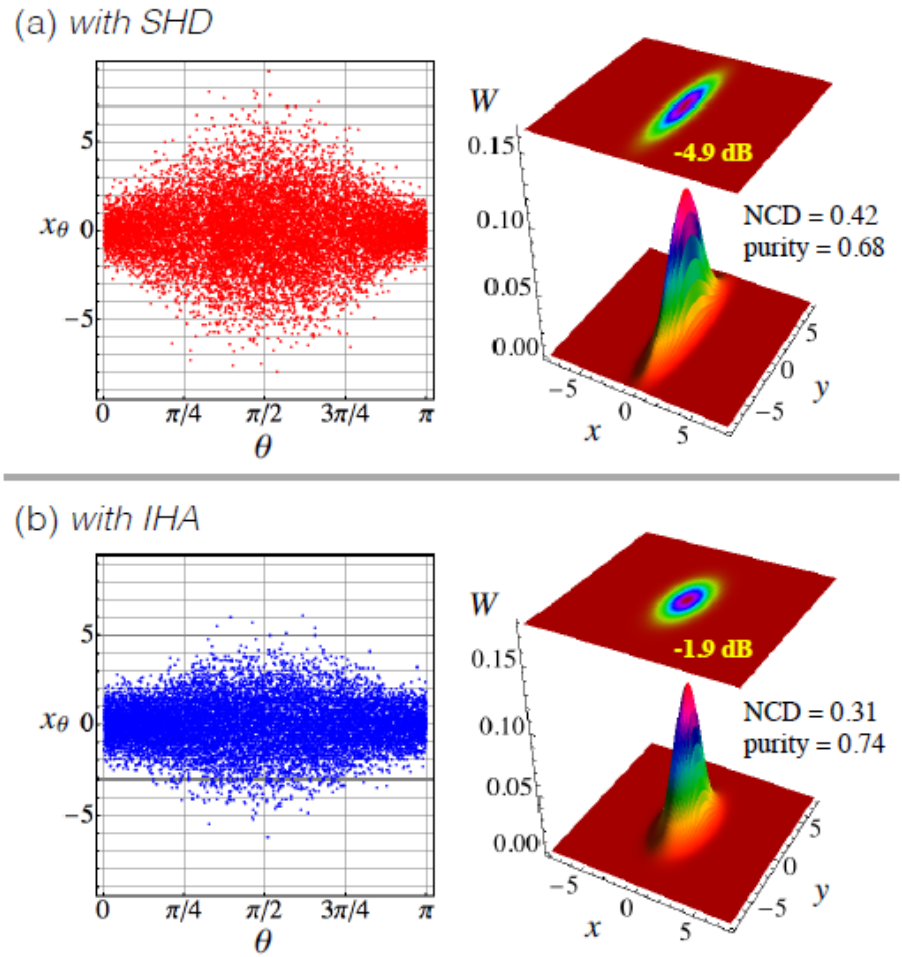

Figure 6.1: Homodyne traces referring to the vacuum squeezed states detected by using the SHD (top panel) and the IHA (bottom panel). We also report the corresponding reconstructed Wigner functions, the nonclassical depth (NCD) and the purity.

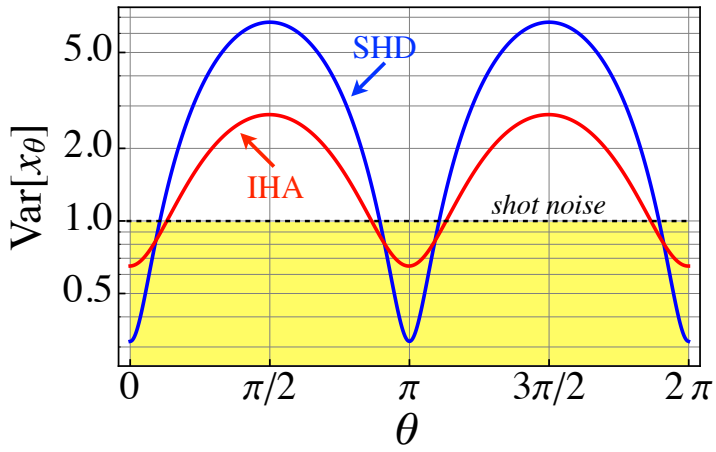

Figure 6.2: Measured quadrature variance as a function of θ for the SHD (blue) and the IHA (red). We also report the shot-noise level for comparison (black horizontal dashed line).

being the k-th outcome from the measurement of the quadrature at LO phase θ_k, with $k = 1, ..., M$. They correspond to the vacuum squeezed states detected by switching between presets as we have seen in Sec. 3.7. In the top panel of Fig. 6.1 we can see the homodyne trace acquired with the SHD, in which the LO phase is scanned from 0 to π. The bottom panel of Fig. 6.1, instead, shows the measurement performed employing the IHA. All traces are normalized to the shot noise level of a pure vacuum field which is therefore set at one. In both cases the pump beam power for the OPO is P = 300 mW and the LO power is set to 10 mW by using an amplitude modulator.

As one can see, the traces exhibit squeezing at $\theta = 0$ and anti-squeezing at $\theta = \pi/2$. By applying the pattern function method to $\{(x_k, \theta_k)\}$, we perform a tomographic state reconstruction of single-mode CV systems. The reconstructed Wigner functions which correspond to the two examined cases are displayed next to the respective homodyne traces in Fig. 6.1. The purity $\mu[\rho] = \mathrm{Tr}[\rho^2]$ and the non classical depth, NCD, [106] of the state ρ acquired with the SHD are μ = 0.68 and NCD = 0.42, respectively, whereas those acquired with the IHA are μ = 0.74 and NCD = 0.31, respectively. It is worth noting that the higher purity of the state acquired by the IHA is due to the presence of losses, which reduce the state energy and make it closer to the vacuum state (which is pure). This is also testified by the squeezing level which is -4.9 dB in the case of SHD and is reduced to -1.9 dB for the IHA.

By using the pattern function tomography, we can also evaluate the quadrature variance $\mathrm{Var}[x_\theta]$ as a function of θ in order to highlight the difference between the squeezing and anti-squeezing levels in the two measurement configurations. The results are shown in Fig. 6.2: the horizontal dashed line represents the vacuum noise level and the observed noise levels for squeezing are -4.9 ± 0.5 dB for the SHD (blue) and -1.9 ± 0.1 dB for the IHA (red). This difference arises from the different efficiencies of the two systems. Indeed, we have seen that the squeezed states that are observed in practical experiments necessarily suffer from losses present in transmission channels and detectors which degrade the observed squeezing and anti-squeezing levels.

In order to analyse in more detail the effect of losses on the single-mode squeezed state, we compare the performance of our apparatus with the theoretical model seen

in Chap 3. We have seen that the noise spectrum $\langle \Delta X_{\pm}^2 \rangle$ of the squeezed $(-)$ and antisqueezed $(+)$ quadrature variances for an OPO below threshold is expressed by Eq. 3.31. When the IHA is used, we also have to take account of the overall IHA efficiency $\eta_c^{\mathrm{IHA}} = \eta_{\mathrm{f}}\,\eta_{\mathrm{w}}$, where η_{f} and η_{w} are the fiber coupling and the the waveguide transmission efficiencies, respectively. The actual value η_{IHA} has been evaluated by measuring the input intensity into the fiber coupling lens and the output intensity at the multimode fiber exit. Since the measured fibers coupling efficiency is $\eta_f = 0.82$, we estimate $\eta_w = 0.51$.

It is worth noting that the chip does not alter the features of the generated states but it acts as a lossy channel. Thus, its effect is merely a degradation of the observed squeezing level. Overall, employing the IHA we have:

$$\eta_{\mathrm{HD}}^{(\mathrm{IHA})} = \eta_{\mathrm{Vis}}^{(\mathrm{IHA})}\,\eta_{\mathrm{BS}}^{(\mathrm{IHA})}\,\eta_c^{(\mathrm{IHA})}\,, \tag{6.1}$$

with now $\eta_{\mathrm{Vis}}^{(\mathrm{IHA})} = 0.96$ (the estimated visibility is $\mathscr{V} = 0.98$), and $\eta_{\mathrm{BS}}^{(\mathrm{IHA})} = 0.998$. For SHD we recall that

$$\eta_{\mathrm{HD}}^{\mathrm{SHD}} = \eta_{\mathrm{Vis}}^{\mathrm{SHD}}\eta_{\mathrm{BS}}^{\mathrm{SHD}} \tag{6.2}$$

In the measurements shown here, we have $\eta_{\mathrm{Vis}}^{(\mathrm{SHD})} \equiv \mathscr{V}^2 = 0.96^2$ whereas all other efficiency values are those indicated in Sec. 3.6. The squeezing levels computed with the theoretical formula Eq. 3.31 correspond to noise reductions of -4.9 dB in SHD and of -1.9 dB in IHA, in agreement with the experimental results.

6.3 Squeezed coherent states

In order to test the reliability of the IHA, here we focus on coherent and squeezed-coherent states. This will allow to demonstrate the performance of our integrated de-

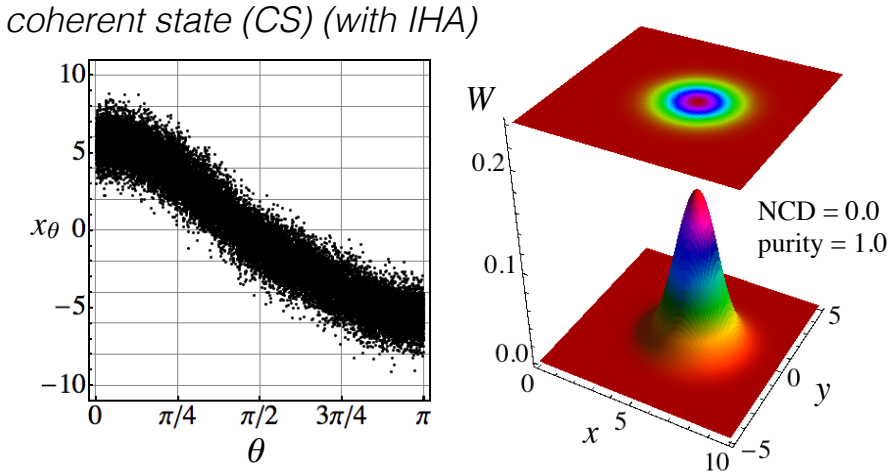

Figure 6.3: Homodyne trace referring to a coherent state (CS) by exploiting the IHA and the corresponding reconstructed Wigner function. The non classical depth (NCD) and the purity of the state are also reported.

vice in the presence of both a classical state, i.e., the coherent state, for which the losses

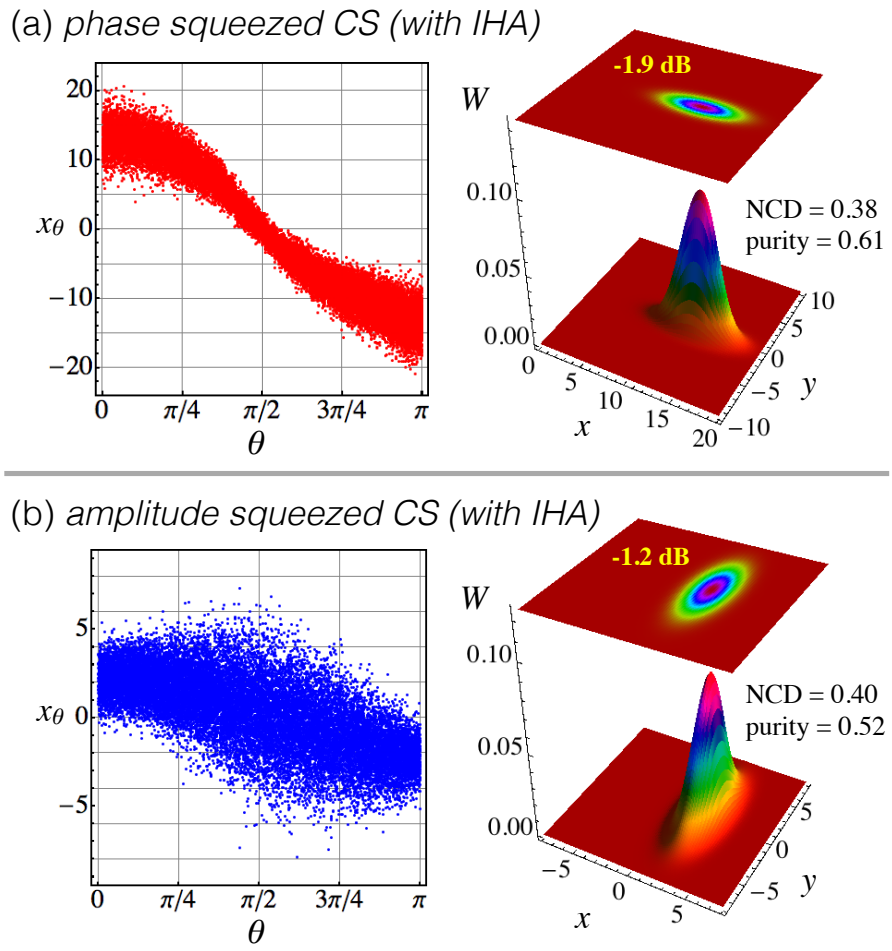

Figure 6.4: Homodyne traces and reconstructed Wigner functions of phase squeezed CS (top panel) and amplitude squeezed CS (bottom panel) by using the IHA. Their non classical depths (NCD) and purities are also reported.

only affect its amplitude but not the phase, and a quantum state. This latter case is the most interesting, since the intrinsic losses of the IHA can make difficult to detect the nonclassical features (squeezing) of the input signal.

In the presence of a coherent state (CS) we obtain the homodyne trace reported in Fig. 6.3. We can see that the IHA allows to record the signal at different phases scanned by the thermo-optic phase shifter. Moreover, the tomographically reconstructed Wigner function corresponds to a coherent state with purity 1 and vanishing non classical depth, as expected.

The phase and amplitude squeezed coherent states are generated by changing the relative phase between the seed and the pump waves, which is controlled by a mirror attached to a piezoelectric actuator intercepting the pump beam optical path. If the pump and seed fields are in phase, the OPO acts to amplify the seed (phase squeezing); if they are π out of phase, it acts to de-amplify the seed (amplitude squeezing). When

we operate in the amplification regime, we observe the phase squeezed CS shown in the top panel of Fig. 6.4: the observed level for squeezing at $\theta = \pi/2$ is -1.9 ± 0.2 dB. On the contrary, when the OPO is operating to de-amplify the seed we observe amplitude squeezing. The measured amplitude squeezed CS shown in the bottom panel of Fig. 6.4 features a noise reduction of -1.2 ± 0.3 dB at $\theta = 0$. It is worth nothing that the difference between the squeezing levels in these two cases is the same that we observe if we perform the measurements using the SHD. The reason for such a discrepancy between these two cases has to be attributed to the PDH system. One of the future improvements of our apparatus should deal with this issue. An upgrade concerning the noise sources suffered by the PDH system should resolve this discrepancy.

6.4 Conclusion

The IHA has been successfully embedded in our optics setup for the generation and characterization of continuous variable optical states, namely, coherent and squeezed coherent states. We have demonstrated that, despite the intrinsic losses which affect the IHA, due to the very nature of the fabrication process, our integrated device is able to detect the nonclassical features of the input signals. In particular, the reliability of the recorded homodyne traces have allowed for the tomographic reconstruction of the considered states by using the pattern function method, thus showing a high degree of reliability also with respect to the standard homodyne technique based on a cube BS and a piezo-mounted movement to scan the field quadratures.

As we pointed out, one of the main limitations of the IHA is the presence of losses. The main future perspective is to work on the waveguide writing process in order to reduce the device internal losses. Despite this limitation, we have shown that this device can already be used in all applications which do not necessarily require a high degree of squeezing. Our results open the way to applications of the IHA in more complex schemes involving, for example, more mixing processes by means of BSs. In this case, the main vantage is that, once aligned, the IHA shows a major stability with respect to that of the cube BS. On the other hand, the IHA makes these complex systems more compact and easier handling.

Conclusion and Perspectives

The research activity presented in this Thesis investigate quantum optical techniques to generate and detect nonclassical states in continuous variable (CV) regime. The work performed during my Ph.D. has been essentially devoted to the implementation of the experimental setup. Its core is represented by an Optical Parametric Oscillator (OPO) whereby squeezed states are generated. The acquisition system consists of an optical homodyne detector (HD). The overall system has a complex structure involving both optical and electronic components. Every step of the generation and acquisition processes have been carefully studied and designed in order to improve as much as possible the performance of the experimental apparatus. Moreover, we have addressed the problem of its alignment through an intense experimental work, in order to achieve the best possible measurement conditions. The excellent agreement between the experimental data and the theoretical predictions shows the level of control achieved in managing this setup.

On the other hand, during my Ph.D. we worked on the engineering of the state generation process. In this regard, a system which consists of optical and electronic components has been developed. By means of a software specifically implemented, it can be controlled in such a way that the states to be injected in the OPO can be generated with amplitude and/or phase distribution selectable on demand and properly acquired. Here we have limited ourselves to regard the squeezed vacuum, coherent and thermal states. In particular, it was just the study of these latter that has highlighted the real skill of our generation/acquisition apparatus, for the first time. The results have been reported in a paper [64] in which we have shown how the accurate control of the thermal and squeezing components of the setup, allows us to address the quantum-to-classical transition for squeezed thermal states. Anyway, this implemented system allows the generation of any sort of Gaussian states on demand and offers novel possibilities of exploiting the quantum features in various fields of applied physics such as measurement technology and information processing.

During my research activity, we also developed an upgrade of the HD system in order to miniaturise it by exploiting an integrated homodyne analyzer inscribed in a glass substrate by femtosecond laser writing technology which incorporates in the same chip both a balanced waveguide beam splitter and a thermo-optic phase shifter. This device has been embedded in our experimental setup and we have demonstrated that, despite the intrinsic losses which affect it due to the fabrication process, it is able to detect the nonclassical features of CV quantum states. Precisely, for the first time, we have demonstrated how this device can be used to measure vacuum and coherent squeezed states. This feasibility testing opens the way for exploring the potential offered by this

device in more complex experimental projects. For example, we have observed that this integrated device tenders a major stability with respect to that of the homodyne system realized with a macroscopic beam splitter (BS), once aligned. Therefore its use may be preferable when we want to realize experiments which involve more BS. Anyway, it can be already utilized whenever high degrees of squeezing is not required. Besides, the future work may be finalized to improve the fabrication processes in order to reduce its intrinsic losses.

In conclusion, our work contributed to understanding the control of nonclassical states generation and detection processes not only in the field of quantum optics but also for applications in the field of Quantum information. Some application has already been realized, but the power of our experimental setup is not yet expired. Furthermore, it is possible to improve our apparatus performance as regards the level of squeezing which we can observe. A future perspective may be a higher insulation of the system from external noises sources which degrade the observable squeezing level. For example, our source is a water cooled laser as we have seen. By replacing the current cooling system with another air-based one, the mechanical vibrations should be reduced. This implementation should result in a further increase of the observable degree of squeezing.

Bibliography

[1] L. A. Wu, H. J. Kimble, J. L. Hall, and H. Wu. In: *Phys. Rev. Lett.* **57**, 2520 (1986).

[2] In: ().

[3] In: ().

[4] H. Vahlbruch, M. Mehmet, K. Danzmann, and R. Schnabel. In: *Phys. Rev. Lett.* **117**, 110801 (2016).

[5] C. M. Caves. In: *Phys. Rev. D* **23**, 1693 (1981).

[6] J. Abadie, B. Abbott, R. Abbott, T. Abbott, M. Abernathy, C. Adams, R. Adhikari, C. Affeldt, B. Allen, and G. Allenet et al. In: *Nat. Phys.* **7**, 962 (2011).

[7] J. Aasi, J. Abadie, B. Abbott, R. Abbott, T. Abbott, M. Abernathy, C. Adams, T. Adams, P. Addesso, and R. Adhikari et al. In: *Nat. Phot.* **7**, 613 (2013).

[8] A. Furusawa, J. L. Sorensen, S. L. Braunstein, C. A. Fuchs, H. J. Kimble, and E. S. Polzik. In: *Science* **282**, 706 (1998).

[9] S. L. Braunstein and A. K. Pati. *Quantum Information with Continuous Variables*. Kluwer Academic Publishers, Dordrecht, 2003.

[10] F. Flamini, L. Magrini, A. S. Rab, N. Spagnolo, V. D'Ambrosio, P. Mataloni, F. Sciarrino, T. Zandrini, A. Crespi, R. Ramponi, and R. Osellame. In: *Light Sci. Appl.* **4**,e354 (2015).

[11] R. Osellame, G. Cerullo, and R. Ramponi. *Femtosecond Laser Micromachining: Photonic and Microfluidic Devices in Transparent Materials*. Topics in Applied Physics, Springer, Berlin., 2012.

[12] D. F. Walls and G. J. Milburn. *Quantum Optics*. 2nd Edition, Springer-Verlag Berlin Heidelberg, 2008.

[13] H. A. Bachor and T. C. Ralph. *A Guide to Experiments in Quantum Optics*. New York: Wiley, 2004.

[14] S. Olivares. In: *Eur. Phys. J. Special Topics* **203**, 3–24 (2012).

[15] H. P. Yuen and V. W. S. Chan. In: *Opt. Lett.* **8**, 177 (1983).

[16] G. L. Abbas, V. W. S. Chan, and T. K. Yee. In: *Opt. Lett.* **8**, 419 (1983).

[17] A. I. Lvovsky, H. Hansen, T. Aichele, O. Benson, J. Mlynek, and S. Schiller. In: *Phys. Rev. Lett.* **87**, 050402 (2001).

[18] A. Zavatta, M. Bellini, P. L. Ramazza, F. Marin, and F. T. Arecchi. In: *J. Opt. Soc. Am. B* **19**, 1189 (2002).

[19] A. I. Lvovsky and J. H. Shapiro. In: *Phys. Rev. A* **65**, 033830 (2002).

[20] S. A. Babichev, B. Brezger, and A. I. Lvovsky. In: *Phys. Rev. Lett.* **92**, 047903 (2004).

[21] A. Zavatta, S. Viciani, and M. Bellini. In: *Phys. Rev. A* **70**, 053821 (2004).

[22] A. Zavatta, S. Viciani, and M. Bellini. In: *Science* **306**, 660 (2004).

[23] V. Parigi, A. Zavatta, M. S. Kim, and M. Bellini. In: *Science* **317**, 1890 (2007).

[24] S. Grandi, A. Zavatta, M. Bellini, and M. G. A. Paris. *Preprint arXiv: 1505.03297*.

[25] E. Jakeman, C.J. Oliver, and E. R. Pike. In: *Adv. Phys.* **24**, 349 (1975).

[26] B. L. Schumaker. In: *Opt.Lett.* **9**, 189 (1984).

[27] B. Yurke. In: *Phys. Rev. A* **32**, 300 (1985).

[28] D. T. Smithey, M. Beck, M. G. Raymer, and A. Faridani. In: *Phys. Rev. Lett.* **70**, 1244 (1993).

[29] M. G. Raymer, M. Beck, and D. F. McAlister. In: *Phys. Rev. Lett.* **72**, 1137 (1994).

[30] D. T. Smithey, M. Beck, J. Cooper, and M. G. Raymer. In: *Phys. Rev. A.* **48**, 3159 (1993).

[31] G. M. D'Ariano, C. Macchiavello, and M. G. A. Paris. In: *Phys. Rev. A.* **50**, 4298 (1994).

[32] M. Munroe, D. Boggavarapu, M. E. Anderson, and M. G. Raymer. In: *Phys. Rev. A.* **52**, R924 (1995).

[33] G. Breitenbach, S. Schiller, and J. Mlynek. In: *Nature* **387**, 471 (1997).

[34] G. M. D'Ariano, M. G. A. Paris, and M. F. Sacchi. In: *NatureAdv. Imag. Electr. Phys.* **128**, 205-308 (2003).

[35] A. I. Lvovsky and M. G. Raymer. In: *Rev. Mod. Phys.* **81**, 299 (2009).

[36] M. Gu, H. M. Chrzanowski, S. M. Assad, K. Modi T. Symul, T. C. Ralph, V. Vedral, and P. K. Lam. In: *Nat. Phys.* **8**,671 (2012).

[37] L. S. Madsen, A. Berni, M. Lassen, and U. L. Andersen. In: *Phys. Rev. Lett.* **109**,030402 (2012).

[38] V. Chille, N. Quinn, C. Peuntinger, C. Croal, L. Mista, Jr. C. Marquardt, G. Leuchs, and N. Korolkova. In: *Phys. Rev. A* **91**,050301 (2015).

[39] G. M. D'Ariano, C. Macchiavello, and M. G. A. Paris. In: *Phys. Rev. A* **5**, 4298 (1994).

[40] G. M. D'Ariano, M. G. A. Paris, and M. F. Sacchi. In: *Adv. Imag. Electr. Phys.* **128**, 205 (2003).

[41] B. E. A. Saleh and M. C. Teich. *Fundamentals of Photonics*. 2nd Edition, New York: Wiley, 2007.

[42] R. W. Boyd. *Nonlinear optics*. Academic Press,London, 1992.

[43] W. Wasilewski, A. I. Lvovsky, K. Banaszek, and C. Radzewicz. In: *Phys. Rev. A* **73**, 063819 (2006).

[44] R. E. Slusher, P. Grangier, A. LaPorta, B. Yurke, and M. J. Potasek. In: *Phys. Rev. Lett.* **59**, 2566 (1987).

[45] C. Kim and P. Kumar. In: *Phys. Rev. Lett.* **73**, 1605 (1994).

[46] O. Svelto. *Principles of Lasers*. 5th edition, Springer Science Business Media, 2010.

[47] O. Slezák, R. Yasuhara, A. Lucianetti, and T. Mocek. In: *Opt. Mat. Express* **6**, 3683 (2016).

[48] K. I. Martin, W. A. Clarkson, and D. C. Hanna. In: *Opt.Lett.* **22**, 375 (1997).

[49] R. C. Eckhardt, C. D. Nabors, W. J. Kozlovsky, and R. L. Byer. In: *J. Opt. Soc. Am. B* **8**, 646 (1991).

[50] R. L. Sutherland and B. Thompson. *Handbook of nonlinear optics*. Boca Raton: CRC Press, 2003.

[51] K. Somiya. In: *Phys. Rev. D* **67**, 122001 (2013).

[52] E. D. Black. In: *Amer. J. of Phys.* **69**, 79 (2001).

[53] W. P. Bowen. *Experiments towards a Quantum Information Network with Squeezed Light and Entanglement*. PhD thesis, the Australian National University, 2003.

[54] Y. Takeno, M. Yukawa, H. Yonezawa, and A. Furusawa. In: *Opt. Express* **15**, 4321 (2007).

[55] S. M. Eaton, H. Zhang, M. L. Ng, J. Li, W. Chen, S. Ho, and P. R. Herman. In: *Opt. Express* **16**,9443 (2008).

[56] F. A. S. Barbosa, A. S. Coelho, K. N. Cassemiro, P. Nussenzveig, C. Fabre, A. S. Villar, and M. Martinelli. In: *Phys. Rev. A.* **88**,052113 (2013).

[57] V. D'Auria, A. Porzio, S. Solimeno, S. Olivares, and M. G. A. Paris. In: *J. Opt. B: Quantum and Semiclass. Opt.* **7**, S750 (2005).

[58] V. D'Auria, S. Fornaro, A. Porzio, S. Solimeno, S. Olivares, and M. G. A. Paris. In: *Phys. Rev. Lett.* **102**, 020502 (2009).

[59] D. Buono, G. Nocerino, V. D'Auria, A. Porzio, S. Olivaresand, and M. G. A. Paris. In: *J. Opt. Soc. Am. B* **27**, A110 (2010).

[60] F. A. S. Barbosa, A. S. Coelho, K. N. Cassemiro, P. Nussenzveig, C. Fabre, M. Martinelli, and A. S. Villar. In: *Phys. Rev. Lett.* **111**, 200402 (2013).

[61] S. Cialdi, C. Porto, D. Cipriani, S. Olivares, and M. G. A. Paris. In: *Phys. Rev. A* **93**, 043805 (2016).

[62] R. Simon. In: *Phys. Rev. Lett.* **84**, 2726 (2000).

[63] R. Simon, A. Serafini, F. Illuminati, and S. De Siena. In: *J. Phys. B: At. Mol. Opt. Phys.* **37**, L21 (2004).

[64] A. Mandarino, M. Bina, C. Porto, S. Cialdi, S. Olivares, and M. G. A. Paris. In: *Physical Review A* **93**, 062118 (2016).

[65] G. M. D'Ariano, M. G. A. Paris, and M. F. Sacchi. In: *Adv. Imag. Electr. Phys.* **128**, 205 (2003).

[66] M. G. A. Paris and J. Řeháček. *Quantum State Estimation*. In: *Lect. Notes Phys.* **649**, 2004.

[67] A. I. Lvovsky and M. G. Raymer. In: *Rev. Mod. Phys.* **81**, 299 (2009).

[68] C. Schwemmer, L. Knips, D. Richart, H. Weinfurter, T. Moroder, M. Kleinmann, and O. Gühne. In: *Phys. Rev. Lett.* **114**, 080403 (2015).

[69] M. Beck, D. T. Smithey, and M. G. Raymer. In: *Phys. Rev. A* **48**, R890 (1993).

[70] A. Ourjoumtsev, R. Tualle-Brouri, and P. Grangier. In: *Phys. Rev. Lett.* **96**, 213601 (2006).

[71] A. Ourjoumtsev, H. Jeong, R. Tualle-Brouri, and P. Grangier. In: *Nature* **448**, 784 (2007).

[72] E. T. Jaynes. In: *Phys. Rev.* **106**, 620 (1957).

[73] V. Bužek, R. Derka, G. Adam, and P.L. Knight. In: *Phys. Rev.* **266**, 454 (1998).

[74] S. Olivares and M. G. A. Paris. In: *Phys. Rev. A* **76**, 042120 (2007).

[75] G. Zambra, A. Andreoni, M. Bondani, M. Gramegna, M. Genovese, G. Brida, A. Rossi, and M. G. A. Paris. In: *Phys. Rev. Lett.* **95**, 063602 (2005).

[76] K. Banaszek and I. A. Walmsley. In: *Opt. Lett.* **28**, 52 (2003).

[77] J. Řeháček, Z. Hradil, O. Haderka, J. Peřina Jr, and M. Hamar et al. In: ().

[78] A. Uhlmann. In: *Rep. Math. Phys.* **9**, 273 (1976).

[79] I. Bengtsson and K. Zyczkowski. *Geometry of Quantum States*. Cambridge University Press, 2006.

[80] C. A. Fuchs and J. van de Graaf. In: *IEEE Trans. Inf. Theory* **45**, 1216 (1999).

[81] V. Dodonov. In: *J. Phys. A* **45**, 032002 (2012).

[82] M. Bina, A. Mandarino, S. Olivares, and M. G. A. Paris. In: *Phys. Rev. A* **89**, 012305 (2014).

[83] A. Mandarino, M. Bina, S. Olivares, and M. G. A. Paris. In: *Int. J. Q. Inf* **12**, 1461015 (2014).

[84] C. Benedetti, A. P. Shurupov, M. G. A. Paris, G. Brida, and M. Genovese. In: *Phys. Rev. A* **87**, 052136 (2013).

[85] A. R. Rossi, S. Olivares, and M. G. A. Paris. In: *J. Mod. Opt.* **51**, 1057 (2004).

[86] A. Ferraro, S. Olivares, and M. G. A. Paris. In: *Gaussian States in Quantum Information* Bibliopolis, Napoli, (2005).

[87] P. Marian and T. A. Marian. In: *Phys. Rev. A* **86**, 022340 (2012).

[88] C. F. Roos, G. P. T. Lancaster, M. Riebe, W. Hänsel H. Häffner, S. Gulde, C. Becher, J. Eschner, F. Schmidt-Kaler, and R. Blatt. In: *Phys. Rev. Lett.* **92**, 220402 (2004).

[89] J. Fulconis, O. Alibart, J. L. O'Brien, W. J. Wadsworth, and J. G. Rarity. In: *Phys. Rev. Lett.* **99**, 120501 (2007).

[90] D. Riste, M. Dukalski, C. A. Watson, G. de Lange, M. J. Tiggelman, Ya. M. Blanter, K. W. Lehnert, R. N. Schouten, and L. DiCarlo. In: *Nature* **502**, 350 (2013).

[91] L. Steffen, Y. Salathe, M. Oppliger, P. Kurpiers, M. Baur, C. Lang, C. Eichler, G. Puebla-Hellmann, A. Fedorov, and A. Wallraff. In: *Nature* **500**, 319 (2013).

[92] C. Kurz, M. Schug, P. Eich, J. Huwer, P. Müller, and J. Eschner. In: *Nat. Commun.* **5**, 5527 (2014).

[93] F. Dolde, V. Bergholm, I. Jakobi Y. Wang, B. Naydenov, S. Pezzagna, J. Meijer, F. Jelezko, P. Neumann, and T. Schulte-Herbrüggen et al. In: *Nat. Commun.* **5**, 3371 (2014).

[94] J. J. Pla, K. Y. Tan, J. P. Dehollain, W. H. Lim, J. J. L. Morton, F. A. Zwanenburg, D. N. Jamieson, A. S. Dzurak, and A. Morello. In: *Nature* **496**, 334 (2013).

[95] J. Goldwin, M. Trupke, J. Kenner, A. Ratnapala, and E. A. Hinds. In: *Nat. Commun.* **2**, 418 (2011).

[96] D. Leibfried, B. DeMarco, D. Lucas V. Meyer, M. Barrett, J. Britton, C. Langer T. Rosenband W. M. Itano B. Jelenković, and D. J. Wineland. In: *Nature* **422**,412 (2003).

[97] A. Politi, M. J. Cryan, S. Yu J. G. Rarity, and J. L. OŔrien. In: *Science* **320**,646 (2008).

[98] L. Sansoni, F. Sciarrino, P. Mataloni G. Vallone, A. Crespi, R. Ramponi, and R. Osellame. In: *Phys. Rev. Lett.* **105**,200503 (2010).

[99] T. Meany, M. Gräfe, R. Heilmann, A. Perez-Leija, S. Gross, M. J. Steel, M. J. Withford, and A. Szameit. In: *Laser Photon. Rev.* **9**, 363 (2015).

[100] J. M. Silverstone, D. Bonneau, J. L. O'Brien, and M. Thompson. In: *IEEE J. Sel. Top. Quantum Electron* **22**,390 (2016).

[101] G. Masada, K. Miyata, A. Politi, T. Hashimoto, J.L. O'Brien, and A. Furusawa. In: *Nat. Photon.* **9**, 316 (2015).

[102] F. Raffaelli, G. Ferranti, D. H. Mahler, P. Sibson, J. E. Kennard, A. Santamato, G. Sinclair, D. Bonneau, M. G. Thompson, and J. C. F. Matthews. In: *arXiv:1612.04676 [quant-ph]* ().

[103] A. Dutt, K. Luke, A. L. Gaeta S. Manipatruni, P. Nussenzveig, and M. Lipson. In: *Phys. Rev. Appl.* **3**, 044005 (2015).

[104] M. Stefszky, R. Ricken, C. Eigner, V. Quiring, H. Herrmann, and C. Silberhorn. In: *Phys. Rev. Lett.* **7**,044026 (2017).

[105] F. Kaiser, B. Fedrici, A. Zavatta, V. D'Auria, and S. Tanzilli. In: *Optica* **3**,362 (2016).

[106] C. T. Lee. In: *Phys. Rev. A* **44**,R2775 (1991).

List of Publications

Refereed publications

S. Cialdi, C. Porto, D. Cipriani, S. Olivares, and M. G. A. Paris. *Full quantum state reconstruction of symmetric two-mode squeezed thermal states via spectral homodyne detection and a state-balancing detector.* Physical Review A **93**, 043805 (2016)

A. Mandarino, M. Bina, C. Porto, S. Cialdi, S. Olivares, and M. G. A. Paris.*Assessing the significance of fidelity as a figure of merit in quantum state reconstruction of discrete and continuous-variable systems.* Physical Review A **93**, 062118 (2016)

Publications under review

C. Porto, D. Rusca, S. Cialdi, A. Crespi, R. Osellame, D. Tamascelli, S. Olivares, and M. G. A. Paris. *Detection of squeezing by on-chip glass-integrated homodyne analyzer* Preprint arXiv:1710.04665 [quant-ph] (2017)

Acknowledgments

This work was supported by UniMI through the UNIMI14 Grant No. 15-6-3008000-609 and the H2020 Transition Grant No. 15-6-3008000-625, and by EU through the H2020 Project QuProCS (Grant Agreement No. 641277), and QUCHIP (grant agreement 641039).

Desidero eprimere la mia gratitudine a tutti coloro che mi hanno accompagnata in questi tre anni di dottorato con insegnamenti, consigli e suggerimenti.

Innanzitutto vorrei ringraziare il mio supervisore, il Dott. Simone Cialdi, per avermi guidato, consigliato e supportato durante tutto il mio percorso. Lo ringrazio non solo per aver cercato in ogni momento di trasmettermi la sua grande conoscenza ed esperienza ma anche per la disponibilità e pazienza dimostratami e per avermi spronato a fare sempre meglio. Per me non è superfluo dire che senza di te questo lavoro non avrebbe preso vita e ti ringrazio sinceramente per tutti i momenti, lavorativi e non, vissuti in laboratorio!

Desidero poi ringraziare il Dott. Andrea Ciprani senza il quale non avrei potuto realizzare questo lavoro, per avermi consigliato e aiutato a superare tutti gli ostacoli, tecnici e non, incontrati in questi anni.

Ringraziamenti speciali vanno, inoltre, al Dott. Stefano Olivares, per tutto quello che mi ha insegnato, per le occasioni di confronto, non solo in ambito professionale, e per i bei momenti trascorsi insieme in laboratorio. La passione e l'entusiasmo che metti nel tuo lavoro sono stati per me d'esempio e ne farò tesoro qualsiasi cosa mi riservi il futuro (...non solo in ambito lavorativo).

Un ringraziamento altrettanto speciale va al Prof. Matteo G. A. Paris non solo per la sua guida e il suo sostegno, ma anche e soprattutto per tutte le esperienze che mi ha permesso di vivere in questi tre anni, che mi hanno fatto crescere sia da un punto di vista professionale che personale.

Infine, ma non per importanza, vorrei ringraziare tutto il gruppo di meccanica quantistica (Applied Quantum Mechanics group – Dipartimento di Fisica – Università degli Studi di Milano) con il quale ho condiviso queste esperienze, per avermi accolto con entusiasmo, per i momenti di confronto e per avermi accompagnato sempre con un sorriso in questo percorso.

Mi sembra doveroso riservare un ringraziamento anche ai referee di questa tesi, il Dott. Alberto Porzio e la Dott.ssa Alessia Allevi, che con le loro osservazioni e i loro suggerimenti hanno contribuito ad arricchicchire la stesura di questo lavoro.

Infine, vorrei dedicare questa tesi alla mia famiglia senza la quale non sarei qui, a questo punto della mia vita: a te, mamma, e a te, Naika... non vi sono parole che possano esprimere quanto vi sia grata... e a te Tommaso, che già da tempo fai parte della mia famiglia... e a voi, babbo e nonno che mi siete sempre a fianco... e a te nonna, che nella tua semplicità sei forse stata la persona che più mi ha sostenuto in questo percoso... tu sei sempre stata orgogliosa di me ma forse quello che non sai è che io sono sempre stata orgogliosa di essere tua nipote... infine a te, Alberto, mio amico e mio compagno, che hai vissuto con me, giorno per giorno, nel bene e nel male, questi tre anni..ti ringrazio per essere stato sempre presente!